Three-dimensional Seismic Analysis and Modelling of Marine Hydrate Systems Offshore of Mauritania

LI, ANG

Three-dimensional Seismic Analysis and Modelling of Marine Hydrate Systems Offshore of Mauritania

Ang Li

A thesis submitted for the degree of
Doctor of Philosophy (Ph.D.) at Durham University

Department of Earth Sciences
Durham University
April 2017

Contents

Abstracts

Marine hydrates, which lock-up vast quantities of methane, are considered to be a prospective alternative energy source, a slow tipping point in the global carbon cycle and a probable trigger for submarine failures. In this thesis marine hydrate systems offshore of Mauritania and associated structural and sedimentary features are investigated by utilising two surveys of high-quality three-dimensional (3-D) seismic data. Interpreting them provides new insights into marine hydrate systems and how they respond to changes in ambient conditions.

In one region of one of the 3-D seismic surveys, a shear zone covering 50 km^2 is identified immediately above the hydrate bottom simulating reflector (BSR). It is considered to be the initial stages of a failure that did not result in widescale downslope transport of the succession. Due to this failure not going to completion, some free gas remains trapped at the level of the BSR. At this level the presence of free gases is supported by the continuous high-amplitude reflections. It is proposed that buoyancy built up by the inter-connected gas accumulation increases the pore pressure of the overlying hydrate-bearing to the level such that its base was critically stressed. In this research there is no seismic evidence for failures triggered by hydrate dissociation but the role of free gas in priming submarine failures is examined.

Whether marine hydrates can release significant amounts of methane into the atmosphere is inconclusive. In this research a proposed model indicates that methane was re-captured in the hydrate stability zone after being liberated. Ocean warming since the last glacial maximum (LGM) gave rise to the shoaling of the base of the hydrate stability zone (HSZ). Gases released from hydrate accumulating at the base entered the HSZ, driven by buoyancy built up in the gas accumulation. The hydrate seal was breached and this is manifested by 15 gas chimneys in seismic data. Hydrates then re-formed at a specific level within the HSZ. This study implies that not all of methane would enter the ocean after released from hydrates and therefore the contribution of marine hydrates to the atmospheric methane budget may be not that much as it was predicted before.

Gas venting is an effective way to transport methane at depth vertically to the ocean and an example of it is found in the feather edge of marine hydrate. This venting was possible due to the presence of faults above a salt diapir and is manifested by a series of pockmarks and mounds at the seabed. The BSR at this site is convex upwards and hence formed a trapping geometry for underlying free gases. Numerical model shows that this up-convex geometry is caused by the salt diapir having a higher thermal conductivity. Permeable migration conduits along the faults and excess pore pressure at the top of the trap allow for the happening of the venting. Compared with the neighbouring area where the BSR can be well observed, the region affected by diapirism has a limited scale of the observable BSR. This absence is proposed to result from the formed trap intercepting methane-rich pore fluid that would migrate landwards along the level of the base of the HSZ.

List of Figures

List of Abbreviations

AWO	acoustic wipe-out	MHSC	methane hydrate stability curve
BHSZ	the base of the hydrate stability zone	PHAA	positive high amplitude anomaly
BSR	bottom simulating reflector	RC	reflection coefficient
BWT	bottom water temperature	RMS	root mean square
FGZ	free gas zone	RSL	relative sea level
HSZ	hydrate stability zone	SID	seabed intersection depth
LGM	last glacial maximum	TWTT	two way travel time
mbsf	metres below seafloor	WOD	World Ocean Database

Declaration

I declare that the work presented in this thesis, submitted for the degree of Doctor of Philosophy at Durham University, is entirely my own except where clearly stated. To the best of my knowledge, this thesis is distinct from any previously submitted or published at this or any other university.

Ang Li

Department of Earth Sciences

Durham University

January 2017

Acknowledgements

Writing this note of thanks is the finishing touch on my thesis and I am very happy to see this day coming. Doing the Ph.D. of geology means a lot to me. Here I would like to convey my heartfelt gratitude to the people who help so much in these four years, not only in the scientific field but also at a personal level.

First I would like to thank my supervisor Richard J Davies for your professional help. You always lead me to think critically when facing a scientific question and encourage me to try some new ideas. This is of great help for me to growing into an independent researcher. I also would like to thank you for tolerance with my 'Chin-English' writing at the beginning of the research. Your decency, passion and insistency on how to do science impress me and will not be forgotten in my future career.

I would like to thank my supervisors Richard Hobbs, Simon Mathias and Jonathan Imber for your wonderful cooperation in my thesis. Your knowledge takes me to different worlds of geology and extends my skills of solving geological problems. Your office doors are always open to me and this gives me more confidence to finish the Ph.D. degree.

My reviewers, Neil Goulty, Christine Peirce and Andrew Aplin, are appreciated for guiding me through the research. Your objective viewpoints and sharp observation push me to re-evaluate my work and find its uncertainties. Your thought-provoking questions in the annual reviews allow me to assess the progress of the research by myself and manage the time such that I can learn how far to go to finish my thesis. I also would like to thank Jon Gluyas and Ken McCaffrey for their lecturing during the CeREES fieldtrip. Looking at the outcrops allows me to learn what the true world of petroleum system is like.

I thank Durham University for providing the friendly working environment and my research funding. I also thank China Scholarship Council (CSC) for providing such an excellent platform of studying abroad and covering my living costs. David Stevenson and Gary Wilkinson are thanked for their help in maintaining the hardware and software related to this research. The computers are moody and not easy to take care of. Hatfield College is thanked for its financial help in this research.

I would like to thank my colleagues, Jinxiu Yang, Yang Li, Longxun Tang, Sal Goodarzi, Loraine Pastoriza, Jack Hardwick, Alex Lapadat, Nadia Narayan, Adam Sproson, Ben Maunder, Harisma Andikagumi, Lamees Abdulkareem, Oliva Sanford, Dimitris Micheliousdakis, Charlotte Withers, Francesca E. Watson, Xiang Ge, Zeyang Liu, Huifei Tao, Wei Zhou and Meiyan Fu. We support each other by deliberating over our problems and talked about things other than just our papers. I also would like to thank my housemates, Junjie Liu, Jing Zhang, Qi Wang, Rongjuan Wang and Yan Qu and my friends, Steve, Yuexian Huang, Xiaolin Mou, Dan Li, Mengwei Sun, Josh, Allan Roberts and Vishal Bandugula Janardhan. Chatting with you guys can let me put the work aside temporarily and enjoy the life.

Last but not least, I would like to thank parents for your sympathetic ear. You are always there for me. Hopefully my small achievement of getting the Ph.D. degree would make you proud. A big thank to my wife who always supports me and takes care of our new born daughter Xuan. You never know how much I miss you and this missing is my biggest motivation to finish my work.

Chapter 1 Introduction

1.1 Background

1.1.1 Gas hydrate

Marine hydrates are ice-like crystalline solids in which gas is physically trapped by water molecules in clathrates (Sloan and Koh, 2007). Gas hydrates have three crystal structures – cubic structure I (sI) (McMullan and Jeffrey, 1965), cubic structure II (sII) (Mak and McMullan, 1965) or hexagonal structure H (sH) (Ripmeester et al., 1987). Most of the gas hosted in marine hydrate is methane and this is a potent green-house gas (Houghton et al., 1992). Its proportion relative to other gases can be up to 99% and the remaining gas includes but is not limited to ethane, propane and carbon dioxide (Soloviev and Ginsburg, 1994). The chemical compound for methane hydrate is $CH_4 \bullet nH_2O$ and for structure I, n = 5.75 (Sloan and Koh, 2007).

The process of hydration is an exothermic reaction that takes place under low temperature and high pressure (Sloan and Koh, 2007). In a temperature-pressure (*P-T*) plot the concave-down curve representing the phase boundary between gas and hydrate is the hydrate stability curve (HSC) which has been measured in the laboratory (Moridis, 2002; Lu and Sultan, 2008). Given that the concentration of the dissolved methane exceeds its solubility, hydrate would be stable under some *P-T* conditions (Fig. 1.1) and these can be met in deep marine environments and the regions where permafrost forms (Kvenvolden, 1993). The zone where hydrate is stable is termed the hydrate stability zone (HSZ) and it can theoretically extend from above the seabed to hundreds of metres below it. Once hydrate has formed in the water column, its buoyancy will raise it to the level at where it is no longer stable, so marine hydrates are normally stable in the HSZ below the seabed (Sloan and Koh, 2007; Fig. 1b). The critical water depth at which methane hydrate is stable in high latitude zones of the Arctic and Antarctic is shallower than that near the equator (Archer et al., 2009). Apart from *P-T* conditions, other factors that control the stability of hydrate include salinity and gas composition (Sloan and Koh, 2007). A hypersaline environment is an inhibitor for hydrate formation (Liu and Flemings, 2006;

Sloan and Koh, 2007). Localised hypersaline environments may be a mechanism for gas passing through the hydrate stability zone (HSZ), which has been recorded by measuring levels of chloride offshore of Oregon (Liu and Flemings, 2006). Hydrates with a higher proportion of heavier hydrocarbon gases have a deeper position for the base of the hydrate stability zone (BHSZ) (Sloan and Koh, 2007). For instance, in the area of Storegga Slide the BHSZ formed by 92% methane and 8% ethane is 45 m lower than that of hydrate made up of 99% methane and 1% ethane at the water depth of 880 m (Posewang and Mienert, 1999). Complex gas composition is thought to give rise to multiple BSRs (Tréhu et al., 1999; Andreassen et al., 2000; Foucher et al., 2002; Golmshtok and Soloviev, 2006; Popescu et al., 2006), but this explanation is still questioned (Posewang and Mienert, 1999).

Continental slopes are common sites where marine hydrate accumulates (e.g. the Gulf of Mexico, Brooks et al., 1984; the Okhotsk Sea, Ginsburg et al., 1993; offshore Costa Rica, Ruppel and Kinoshita, 2000; the Blake Ridge, Hornbach et al., 2003; at the Storegga slide, Bünz and Mienert, 2004; offshore Oregon, Tréhu et al., 2004; Hornbach et al., 2008; offshore Alaska, Collett, 2008; eastern Nankai Trough, Saeki et al., 2008; offshore Svalbard, Bünz et al., 2012; offshore Angola, Serié et al. 2012). It often accumulates at the BHSZ when dissolved gas is transported upwards into the HSZ by migrating pore-water and sufficient to create hydrates (Fig. 1.2, Singh et al., 1993; Hornbach et al., 2003; Haacke et al., 2007). Free gas is often below the BSHZ. It is formed by the hydrate recycling mechanism in which water and gas are released from hydrate-containing sediments due to the upward shift of the BHSZ, driven by the ongoing sedimentation, tectonic uplift, sea-level fall or bottom water warming. The FGZ can also be formed by the solubility-curvature mechanism that states the concentration buffer of gas hydrate enables the competing effect of downward diffusion and upward advection to form a steady-state aqueous concentration curve. If this curve and that of the solubility is sufficiently flat, pore water becomes saturated and free gas can form (Haacke et al., 2007). When gas can coalesce to form a continuous buoyant volume (gas saturation could be ~10%, Schowalter, 1979), it is normally trapped below the BHSZ due to the clogging effect of hydrates in sediments (Nimblett

and Ruppel, 2003; Chabert et al., 2011). Gas hydrates can also be found to outcrop at or near the seabed. The outcropping hydrate-bearing sediments imaged by photos or seismic data have mound-like morphology, either near the intersection between the BHSZ and the seabed (Egorov et al., 1999) or kilometres away from this intersection in a seaward direction (Roberts, 2001; Serié et al. 2012). In addition, gas chimneys, which are interpreted as potential migration pathways for water and gas to reach the seabed (Cartwright and Santamarina, 2015), could be favourable places for hydrate accumulations (Fig.1.2, Plaza-Faverola et al., 2010). So far these are the main patterns of hydrate accumulation that have been seen more than once in different areas around the world.

1.1.2 Detecting marine hydrate in the subsurface

Hydrate can be identified visually in cores brought to the surface. Direct observation of the gas hydrate in cores sampled from the deep-water sediments has been recorded in the Okhotsk Sea for example (Ginsburg et al., 1993). It has been found in veins, nodules or sub-horizontal layers (Ginsburg et al., 1993; Kvenvolden, 1993). The Pressure Core Sampler (PCS) tool is used to directly measure the gas released from hydrate under in-situ *P*-*T* condition (Dickens, 1997; Milkov et al., 2004; Yun et al., 2011) and it allows for an assessment of the amount of methane stored in hydrates in an area of interest. The photos taken by a remote operated vehicle (ROV) have shown that hydrate mounds exposed at the seabed can be partly or completely covered by chemosynthetic communities, such as bacterial mats and tube worms (Hovland and Svensen, 2006; Roberts et al., 2006). During its dissociation, hydrate absorbs heat and leaves low temperature anomalies in the extracted core (Ford et al., 2003). Therefore, the temperature profile obtained by scanning using infrared rays can indicate where hydrate dissociated before (Ford et al., 2003; Tréhu et al., 2004). Other core-scale data that can indicate the presence of gas hydrate is an anomalously low chloride concentration as hydrate dissociation releases water and therefore decreases the salinity of pore fluid (Hesse and Harrison, 1981; Tréhu et al., 2004). Hydrate can also be found in the sedimentary succession based on the analysis of well-logs such as the electrical resistivity log and the acoustic transit-time log

(Collett, 2001). An increase in resistivity and a decrease in transit times indicates the presence of gas hydrate (Collett, 1999; Collet and Wendlandt, 2000; Lee et al., 1993).

Hydrate can be revealed by seismic imaging. The bottom simulating reflector (BSR) is a robust indirect proxy for the presence of hydrate (Tréhu et al., 2003). These reflections were first reported in the 1970s (Shipley et al., 1979) and since then examples have been found along continental margins (e.g. Tréhu et al., 2006) and in lakes (e.g. Vanneste et al., 2001). The occurrence of BSRs is a seismic response to the transition from hydrate-bearing sediment to underlying sediment hosting free gas. Reflections occur even when the saturation of trapped gas is as low as 1%-5% (MacKay et al., 1994). The BSR shallows landwards until it intersects the seabed and this zone is termed the feather edge (more introduction please see section 5.2). In the HSZ an isolated gas hydrate deposit can be detected on the basis of an acoustic impedance contrast between hydrate-bearing and hydrate-free sediments and it is normally lower than that at the BHSZ (Zhang et al., 2012). Hydrate concentration can be calculated based on rock physics models and assumptions regarding whether it is part of the pore fluid or the cementing sediment grains (e.g. offshore Svalbard, Chabert et al., 2011). Up until now this is the geophysical approach that has been used most commonly in assessing hydrate resources. Electromagnetic method is an additional tool to seismic surveys and have the potential to detect the hydrate and its volume due to its higher electrical resistivity than water-saturated sediments (Weitemeyer et al., 2006). The concentration of gas hydrate is estimated to be 0-30% and 27-46% offshore Oregon using this method (Weitemeyer et al., 2006; Weitemeyer et al., 2011).

1.1.3 Significance of marine hydrate

The process of hydration significantly narrows the molecular spacing of gas. This means hydrate can host gas whose volume under standard temperature and pressure (STP) is ~164 times as that of the hydrate itself (Max et al., 2005). Therefore, hydrate accumulations can be taken as a concentrated hydrocarbon resource and its prospect of being an energy source has been recognised (Collett, 2002; Kerr, 2004; Boswell, 2009). To better assess this potential, we

have to know how much methane is trapped in marine hydrate (Kvenvolden, 1993). So far the error of the estimation of the global hydrate reserves might have orders of magnitude and this estimate has been updated several times (Kvenvolden, 1988; Gornitz and Fung, 1994; Harvey and Huang, 1995; Collett, 2002; Milkov, 2004; Johnson, 2011). The latest estimates of the global resources of methane trapped in hydrate are 4705 – 313992 trillion cubic feet (TCF) which is 133.2– 8891.3 trillion cubic metres (TCM) (Johnson, 2011). Even if a small proportion of this gas is exploitable, it exceeds the sum of the known terrestrial reserves of natural gas (Kerr, 2004). Nowadays methane hydrate as a source of methane is technically feasible (Boswell, 2009). Developing gas hydrate by means of depressurisation has been tested and the gas flow is got (Moridis, 2008; Yamamoto et al., 2014).

Gas hydrate has been referred to as a large carbon capacitor that accounts for a proportion of the potentially releasable carbon in the oceanic lithosphere (Dickens, 2003). The possibility of methane that is or was hosted in hydrate entering the ocean and atmosphere has been speculated before (Kennett et al., 2000). Whether this methane has contributed or could contribute in the future to climatic warming is an important geoscientific question, particularly because estimated global climatic temperatures closely track methane concentrations in the atmosphere (Kvenvolden, 1993; Loulergue et al., 2008). The answer, however, is much debated. Methane liberated from gas hydrate due to oceanic warming and massive methane release have been predicted (Berndt et al., 2014; Phrampus and Hornbach, 2012), but most of this methane (~60 %) would be consumed by oxidation in the ocean (Graves et al., 2015) and only modest quantities are thought to be able to reach the atmosphere. Even so, it can sometimes escape into the atmosphere through focussed gas venting within gas plumes (Graves et al., 2015; McGinnis et al., 2006; Myhre et al., 2016). However, Arctic ice records casts doubt as to whether methane escape from methane hydrates makes a contribution to atmospheric levels during late Quaternary rapid warming events (Sowers, 2006). Even if methane liberated from marine hydrate could enter the atmosphere, it is thought this entry would be slow, rather than resulting in the spike of the methane budget on a human time scale (Archer et al., 2009). Methane release

from hydrates in the Arctic and Subarctic area over the next century is predicted given different scenarios of future climate and sea level change (Hunter et al., 2013; Vadakkepuliyambatta et al., 2017) and the impact of this release on climate is under research (Ruppel and Kessler, 2016).

Marine hydrate is considered to have the potential to destabilise marine sediments and trigger submarine failures that could destroy submarine infrastructure (Kvenvolden, 1993; Lane and Taylor, 2002). Once hydrate has formed and filled pore space of marine sediments, consolidation and cementation are inhibited (McIver, 1982). Gas hydrate at the BHSZ is metastable and will decompose when ambient conditions change (e.g. bottom water temperature increases or sea level drops). As a result, sediment hosting hydrate may become under-consolidated and overpressured if dissociation occurs. This primes submarine slides that can be later triggered by gravitational loading or earthquakes (McIver, 1982). This mechanism may explain the formation of the Storegga slide offshore of Norway for example, although whether it is responsible is inconclusive (Berndt et al., 2002; Kvalstad et al., 2005; Mienert et al., 2005; Brown et al., 2006).

1.1.4 Fluid escape pipes

Fluid escape pipes were defined as a highly localised vertical to sub-vertical pathways of focused fluid (Carwright and Santamarina, 2015). There are other terms referring to these features, such as seismic chimneys and gas chimneys that both have a columnar shape and similar formation mechanisms and seismic features with pipes (Carwright et al., 2007; Carwright and Santamarina, 2015). Pipes are found in deep-water settings around the world and their presence suggests that over-pressured pore fluid, which normally carries considerable amount of gas, bypasses the overlying sediments and potentially enters the ocean (Carwright et al., 2007). The outcrop of pipe has been found in Greece and show metre-sized cavities at the bottom, circular tot oval structures in the middle and strongly sheared country rock at the top (Løseth et al., 2011). Most of the observation of pipes is made in seismic survey. Pipes manifest as vertical to sub-vertical zones of disrupted reflectivity (Fig. 1.3). The stratal reflections within

these zones may be offset, deformed, attenuated or are enhanced (Fig. 1.3, Carwright and Santamarina, 2015). The imaging quality of pipes decreases with increasing buried depth and decreasing pipe width (Løseth et al., 2011; Carwright and Santamarina, 2015). Pipes can form when (1) a network of hydraulic fractures triggered by excess pore pressure propagates towards the seabed (Carwright et al., 2007); (2) the fluidised grains of sediment are mobilised by seepage forces (Carwright et al., 2007; Moss and Cartwright, 2010b); (3) an accumulating gas column overcomes the capillary sealing and advances as a piston (Cathles et al., 2010); or (4) localised subsurface volume is lost hence vertical permeability is significantly increased (McDonnell et al., 2007; Sun et al., 2013).

1.2 Scope of thesis

Marine hydrate system and gas migration in the subsurface offshore of Mauritania have been documented. The BSR, gas seepages, mud volcanoes and slope failures are identified in the 2-D seismic survey (Lane and Taylor, 2002). 3-D seismic survey allows for more knowledge related to the hydrate system, including that gas can migrate along the gravity-driven faults (Yang and Davies, 2013) and the BHSZ (Davies et al., 2014) and through mass transport complex (MTC) (Yang et al., 2013). Gas can also be recycled in stratigraphy trap, which can lead to more gas accumulation and overpressure at its top (Davies and Clarke, 2010). Changes in bathymetry, such as sedimentation and canyon migration at the seabed, result in the resetting of the BSHZ (Davies and Clarke, 2010; Davies et al., 2012b). In general the presence of this widespread resetting is evidenced by tracking the relict bases of marine hydrates in the seismic dataset (Davies et al., 2012a). This research continues to focus on the marine hydrate system offshore of Mauritania.

The fundamental question addressed here is how the marine hydrate system responds to changes in ambient conditions and what the geological results and implications are. Hydrate dissociation due to bottom water warming has been predicted in high-latitude zones (e.g. Berndt et al., 2014), but whether this scenario takes place in the low-latitude zones such as offshore of

Mauritania has not been documented. In this research seismic features of the BSR and related to gas accumulation and migration are described and interpreted. Numerical modelling is used to estimate the depth of the present-day BHSZ at present and in the past and resetting of the BHSZ in a setting affected by a salt diapir. The modelling results combined with the interpretations of two 3-D seismic surveys provide new insights into the marine hydrate system. The link of marine hydrates to submarine failures, under what circumstances methane is vented and in what way is methane recycled will be investigated.

1.3 Thesis structure

Chapter 2 starts with the introduction of the geological setting offshore of Mauritania. This is followed by an explanation of the general workflow for acquisition and processing of the seismic datasets and the types of seismic attributes used in this research. Chapters 3-5 present the key results and interpretations in the form of the independent research papers. Each of them attempts to answer a scientific question so as to extend our knowledge of the marine hydrate system. The word 'we' refers to the authorship denoted in each chapter. Chapter 3 is published by the journal of Marine Geology. Chapters 4 and 5 are accepted by the journal of Marine and Petroleum Geology. All the words are written by the writer and revised by the co-authors. The modelling code is written through collaborating with Simon and Jinxiu. All of the reflections in this study are picked, tracked and mapped by the writer except the seabed reflection in chapter 3 and the BSR in chapter 5.

The title of chapter 3 is 'Gas trapped below hydrate as a primer for submarine slope failures'. 3-D seismic imaging reveals a shear zone at the base of a partially developed slope failure, immediately above a BSR. This is a rare example of a shear zone that did not lead to the complete development of a slope failure. It is proposed it provides the first seismic evidence that the buoyancy effect of gas below the hydrate rather than the hydrate dissociation is also a viable mechanism for large-scale slope failures.

The title of chapter 4 is ‘Methane hydrate recycling probably after the last glacial maximum’. Knowing how methane is recycled in marine hydrate system is important in assessing the contribution of marine hydrate to the carbon budget in the ocean and atmosphere. This research provides a new evidence of methane recycling by showing some hydrate deposits that are interpreted to be recycled from gases trapped below the HSZ. The trigger for the methane transport may be the oceanic warming since the LGM. This process is a mechanism buffering methane escape towards seafloor and speculated to in part explain why atmospheric methane in the late Quaternary is not recorded in the ice cores in the polar region.

The title of chapter 5 is ‘Gas venting that bypasses the feather edge of marine hydrate’. A venting system has been identified based on the spatial relationship between pockmarks and permeable faults. Methane is interpreted to be vented to the seafloor surface or trapped below the elongated up-domed BHSZ. The absence of the BSR landward of the venting system suggests that relatively few gases exist in the locale. Investigation into this venting allows for analysing the probable impact of venting on landward gas migration.

Chapter 6 discusses the uncertainties encountered throughout the research. They include uncertainties in seismic resolution, resetting of the BHSZ and input parameters into numerical models. Future work involves predicting methane release, its fate, what proportion of methane release would be retained in subsurface and implication for the climate change. The thesis ends with listing the key findings and the conclusions.

1.4 Figures

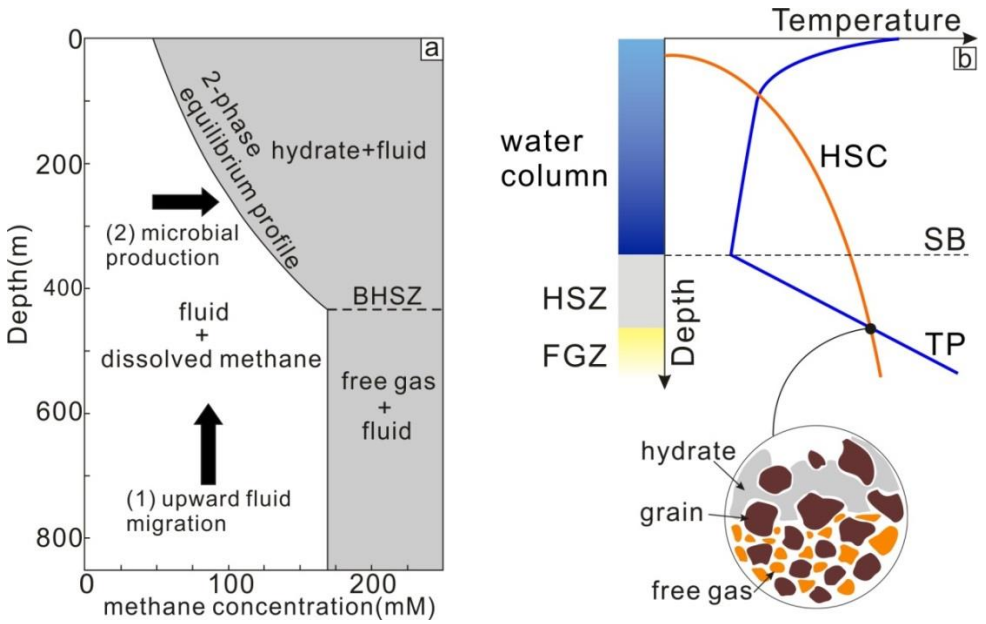

Fig.1.1 (a) Schematic diagram showing the relationship of phases between dissolved gas, free gas and gas hydrate (after Davie and Buffett, 2003, their figure 2). Two mechanisms of formation of gas hydrate: (1) Saturated methane-bearing fluid to form hydrate as it migrates upwards into the HSZ; (2) Methane concentration is increased by microbial production of methane until its solubility is exceeded and hydrate forms. (b) *T-D* diagram showing the HSZ. HSC –hydrate stability curve, SB – seabed, TP – temperature profile, HSZ – hydrate stability zone, FGZ – free gas zone.

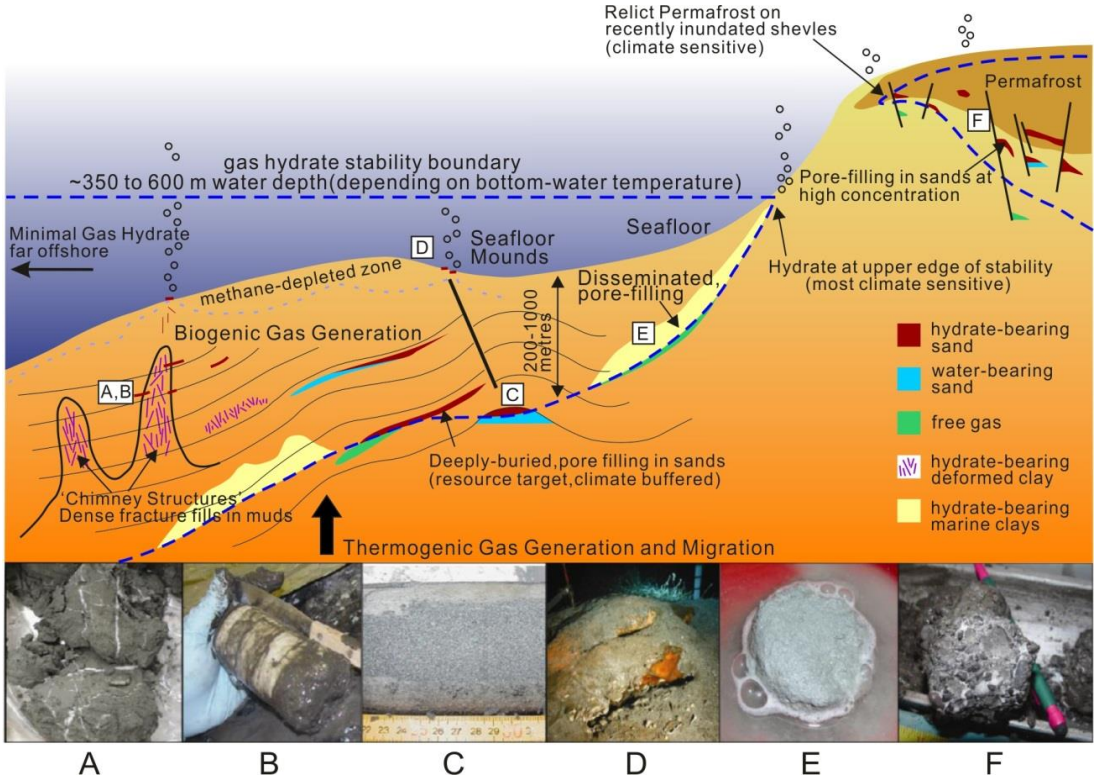

Fig.1.2 Schematic showing modes of hydrate accumulation at continental slope (after Beaudoin et al., 2014, their figure 2.1). The figure is not to scale but the width of the section is likely to be tens to hundreds of kilometres and the depth is probably < 2 km. A, B, C, E and F are core photos and the width is 7 – 10 cm. D is a photo taken at the seabed.

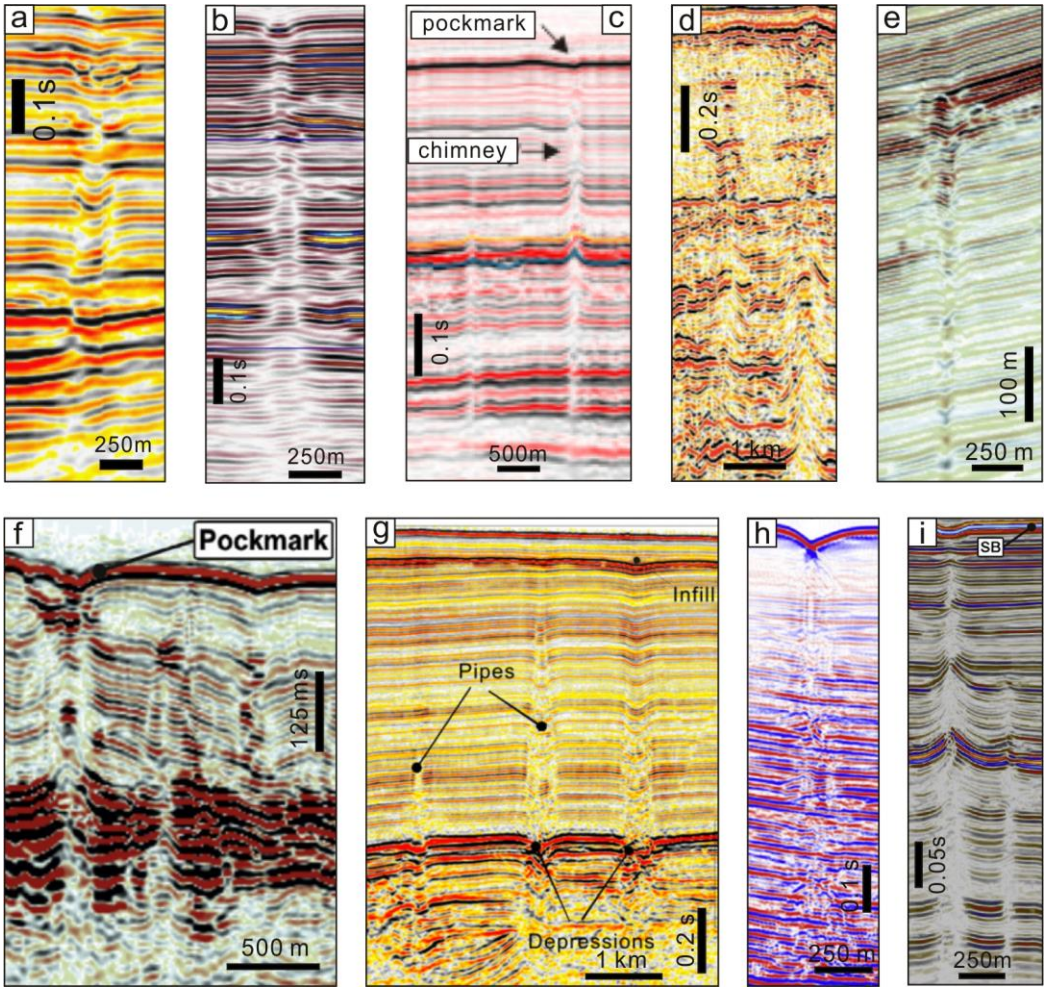

Fig.1.3 Seismic expressions of gas chimneys in cross sections. These exampes are from: (a) offshore Namibia (Moss and Cartwright, 2010); (b) offshore Nigeria (Løseth et al., 2011) ; (c) offshore mid-Norway (Hustoft et al., 2010); (d) Faeroe-Shetland Basin (Cartwright, 2007); (e) offshore Mauritania (Davies and Clarke, 2010); (f) offshore Angola (Andresen et al., 2011); (g) South China Sea (Sun et al., 2013); (h) East Japan Sea (Horozal et al., 2017) and (i) offshore Norway (Plaza-Faverola et al., 2011).

Chapter 2 Geological Setting, Seismic Dataset and Methodology

2.1 Geological setting

The Northwest African continental margin formed after seafloor spreading which began in late Triassic to mid-Jurassic times (Rad et al., 1982). After rifting, thick sediment packages accumulated and at present the sediments deposited in the Senegal-Mauritania Basin are more than 10 km thick (Rad et al., 1982). The continental shelf offshore Mauritania is typically 25-50 km wide, while in the north it expands to up to 150 km wide and forms the shallow marine platform of the Banc d'Arguin (Henrich et al., 2010; Zühlsdorff et al., 2007). Some canyons incise the continental slope such as the Timiris and Tioulit Canyon (Fig. 2.1; Seibold and Fütterer, 1982; Antobreh and Krastel, 2007). Seismic reflection profile EXPLORA 78-48 along with the DSDP 367 and 368 constrain the age of the sedimentary rocks offshore of Mauritania as younger than Jurassic (Rad et al., 1982). The presence of salt diapirs indicates that evaporates were deposited on the subsiding continental basement blocks in a narrow elongate zone between 16^{o} N and 19^{o} N (Rad et al., 1982). A prominent sedimentary feature is the Mauritania Slide Complex that formed as a result of multiple failure events (Antobreh and Krastel, 2007). More details about the sedimentary setting and the petroleum system will be introduced in the section of geological settings in chapters 3 to 5.

The studied succession, which extends from the seabed down to ~500 m below it, were deposited from Pliocene to present day and this age is constrained by the exploration well of Ras El Baida A-1 ($20^{o}15'48''$ N, $17^{o}52'02''$ W). Along the continental margin there is strong seasonal upwelling caused by the interaction between the trade wind system in the northern hemisphere and the African monsoonal system in a southern direction (Wefer and Fischer, 1993; Nicholson, 2000).

2.2 Seismic dataset

2.2.1 Acquisition and processing of marine seismic dataset

The author was not involved in the acquisition and processing of the seismic dataset and there was limited information available on how it was acquired and processed. The conventional operation of marine seismic data acquisition involves that a ship towing the equipment of source and hydrophone streamer at the water depth of a few metres (Fig. 2.2). The operation normally proceeds at 11 km/h (Sheriff and Geldart, 1995) on a clockwise or counter-clockwise basis, each cycle with a lateral offset. An ideal environment for data acquisition is windless and acoustically quiet in the water. The air guns, the most widely used seismic source, are towed by the same ship or another one synchronised with the ship receiving data. During the operation, the air guns are spaced ~30-45 m apart and in turns give an energy pulse at an interval of 10-15 s (Sheriff and Geldart, 1995). The expansion and collapse of the air bubble in the water act as an acoustic source sending sound waves through the water and into the subsurface below the seabed (Bacon et al., 2007). The waves are reflected at interfaces that represent acoustic impedance contrasts and the wave path can be predicted by the Zoeppritz's equations (Sheriff and Geldart, 1995). Then the reflected wave is recorded by a hydrophone, or marine pressure geophone, the signal receiver kept at the water depth of 10-20 m and normally deployed in more than one streamer (Sheriff and Geldart, 1995). In modern equipment including multiple-source and multiple-streamers (e.g. Fig. 2.2), the separation between the recorded lines is between 25 and 37.5 m, while the one between traces recorded along the line, which is determined by the receiver spacing, is between 6.25 and 12.5 m (Bacon et al., 2007).

After the data are acquired, they cannot be used for interpretation until they have been processed. The objective of the processing is to reshape the information into the more understandable form, usually images of reflections (Sheriff and Geldart, 1995). The typical sequence of seismic processing is shown in Fig. 2.3. It can be varied to account for the specific needs of the interpreter. Some key steps are briefly introduced here. In general there are three main sub-sequences of processing: editing, principal processing and final processing (Sheriff

and Geldart, 1995). (1) In editing, the data are rearranged or demultiplexed from the time-sequential to the trace-sequential. (2) Dead and very noisy traces are detected here and along them the unwanted values are zeroed out or replaced with interpolated ones. (3) The data, commonly recorded with a 2 ms sampling interval, are then resampled to 4 ms. The recorded data are sufficient to record frequencies up to 125 Hz and the number of the sampling points halves after this resampling to speed up the later processing stages (Bacon et al., 2007). (4) In the principal processing pass, deconvolution, defined as convolving with an inverse filter, is a very important step, aiming to extract the reflectivity function from the seismic trace and hence improve vertical resolution and recognition of events (Sheriff and Geldart, 1995). More than one deconvolution operation is used to remove different types of distortion such as a short period of reverberation (Sheriff and Geldart, 1995). (5) Common-midpoint stacking, or common-midpoint gather, has traces for a specific midpoint arranged side by side and for both sides the distance between source and geophone is same. The traces within a common-midpoint gather are summed to yield a singly stacked trace and hence this considerably improves data quality (Sheriff and Geldart, 1995). (6) In a case of midpoint gathering where the source-to-receiver distance increases symmetrically, the increase in the travel-time from the zero-offset case is called the normal moveout (NMO). The NMO correction is necessary before traces can be stacked together. (7) Apart from the NMO correction, the dip moveout (DMO) is needed due to not considering the effect of a dipping reflection on the correct zero-offset trace. (8) After these corrections are done, a common-midpoint stack is yielded by combining a sequence of common-midpoint gathers, then the output amplitude is divided by the number of live traces entering the stack given that all traces have equal weight. (9) The stacked data can be repositioned from the recorded location to the correct spatial location. This process is called migration and it is done for the need of further interpretation.

2.2.2 Seismic dataset and attributes

Two 3-D seismic surveys used in this research were acquired over blocks C-6 in March 2000 and C-19 in December 2012. They are provided by Tullow Oil and Chariot Oil & Gas

Limited and their partners, respectively. They are both offshore Mauritania and the regions are 18.4-19.0° N, 16.6-17.4° W and 19.7-20.5° N, 17.3-18.1° W, respectively (Fig. 2.1). They show the seismic features at the seabed and in the subsurface along the Mauritania continental margin. At the seabed there are canyons (including the Timiris Canyon and Tioulit Canyon), moats, coral reefs pockmarks and fault scarps, while in the subsurface buried canyons, mass transport complexes (MTCs), faults can be observed. The BSR can be observed over most areas of the study area. The background reflections in the HSZ are well-stratified and show few amplitude anomaly. The clear seismic features and little noise make these surveys good for research of gas hydrate. The geophysical details of the seismic surveys are introduced in the methodology section of chapters 3, 4 and 5.

The seismic polarity and phase are the key to translate seismic reflection images into the information of major stratal interfaces through the process of seismic interpretation. The seismic phases seen mostly by interpreters are the zero- and minimum-phase (Fig. 2.4). A zero-phase wavelet, such as the Ricker wavelet, is symmetrical about its centre, while a minimum-phase wavelet starts at time zero and most of its energy is near the time zero. An ideal output after data processing is that an acoustic impedance contrast convolves with a zero-phase wavelet, as it has the best resolution for any given bandwidth. Such a wavelet, however, cannot be produced by air guns due to the non-output before time zero (Bacon et al., 2007). The seismic record of air guns is close to the minimum-phase. Additionally, even if a zero-phase wavelet is available, a filter is required during processing to remove the phase distortion produced by attenuation when waves pass through the underground (Bacon et al., 2007). Therefore, for a better interpretation result, the recorded data will firstly be acquired through using air gun that produces wavelet close to the minimum-phase. Then the data are converted to zero-phase. The polarity convention that has been most widely used is the standard of Society of Exploration Geophysicists (SEG). It defines for a minimum-phase wavelet and a positive reflection (a reflection from an interface where the acoustic impedance increases), the waveform starts with a marked trough represented by negative values and followed by positive ones displayed as a small peak (Fig. 2.5a). For a

zero-phase positive reflection, the waveform is symmetrical with the largest positive number locating at the stratal interface (Fig. 2.5b). A minority use the opposite standard, so for any 3-D seismic survey the phase and polarity are supposed to be noticed with caution prior to interpretation. If the 3-D marine seismic survey is provided but without accurate geophysical details such as polarity and phase, which happens in this research, an effective way to determine the wavelet phase and what reflection package represents acoustic impedance increase is to analyse the reflection marking the seabed (Fig. 2.6). For instance, in the C-6 survey, the seabed reflection starts with a bright red reflection consisting of the trough along each trace and underlain by a relatively dim black one (Fig. 2.6). This is consistent with the seismic signature of the minimum-phase wavelet. For the C-19, the seabed reflection is a black-red-black reflection and the values of the two black reflections are similar (Fig. 2.6). Its vertical symmetry suggests that the data were converted to zero-phase during processing. For the rest of the reflections in either survey, the reflection package having the same colour with the seabed indicates the increase in the acoustic impedance.

Reflection amplitude measured at the crest of an identified reflection is by far the most extensively used seismic amplitude attribute in interpretation (Brown, 2010). Its spatial variation can be displayed in a freely picked cross section, a time or depth slice, or a map tracking any specific surface, usually along a reflection. The values of this amplitude represent the reflection coefficient (RC) at the interface between different medium. In a normal incidence of P-wave propagation, the reflection coefficient is defined as:

$$R = \frac{Z_2 - Z_1}{Z_2 + Z_1} \qquad \text{Eq. 2.1}$$

where R is the reflection coefficient, Z_1 and Z_2 are the acoustic impedances of two different medium. The acoustic impedance is defined as:

$$Z = \rho \times v \qquad \text{Eq. 2.2}$$

where ρ is the density of the medium and v is the velocity of primary wave (P-wave) passing through medium. From this equation we can see that the medium density and the velocity of the

P-wave passing through them are the key parameters determining strength of amplitude. For a porous medium, such as rock, its velocity can be empirically predicted by Wylie's equation without considering the structure of a rock matrix, the connectivity of pore spaces, cementation, or past history:

$$\frac{1}{v} \equiv \phi\frac{1}{v_f} + (1-\phi)\frac{1}{v_m} \qquad \text{Eq. 2.3}$$

where ϕ is the porosity, v_f is the fluid velocity and v_m is the velocity of rock matrix. The monotonic relation between velocity and porosity, which is revealed by Eq.2.3, works best when: 1) the rocks have relatively uniform mineralogy, 2) the rocks are fluid-saturated and 3) the rocks are at high effective pressure. This model has limitations and is not working when the rocks are unconsolidated and charged with gases (Mavko et al., 2009). Therefore, in this research the velocity of gas-charged sediment is from the data recorded before, not calculated using Eq.2.3. There are other models to better show the relation between velocity and porosity such as Raymer-Hunt-Gardner model (Mavko et al., 2009). For most of the interface encountered by P-waves, the density and velocity contrasts are small, so a small portion of energy is reflected at any one interface. The reflectance will be enhanced positively when P-wave touches hard horizon, such as carbonate, salt, or igneous body, or gas/oil and oil/water fluid contact and negatively if wave encounters gas reservoir or the BHSZ (Brown, 2010). In this research the used amplitude attribute is the root mean square (RMS) amplitude. The amplitude value, A_{RMS}, is calculated from the neighbouring values by:

$$A_{RMS} = \sqrt{\frac{1}{n}\sum_{i=1}^{n} A_i^2} \qquad \text{Eq. 2.4}$$

where A_i is the amplitude value of the neighbouring points sampled within the specified window in the post-stack dataset. This attribute resembles a smoother version of reflection strength. It is applied in the same way as reflection strength to reveal bright spots and amplitude anomalies in the seismic data.

The second used seismic attribute is the dip-magnitude, a time-derived horizon attribute addressing issues of structural details with the convenient units of samples per trace scaled by 100. The inline and crossline spacings are taken to be 1 and the true spacings are not used. Dip magnitude, p, can be expressed as:

$$p = \sqrt{\left(\frac{\partial z}{\partial x}\right)^2 + \left(\frac{\partial z}{\partial y}\right)^2} \qquad \text{Eq. 2.5}$$

where $\partial z/\partial x$ and $\partial z/\partial y$ are the slope in the x and y direction, respectively. Dip represents the magnitude of the maximum slope of the seismic reflection at a point. This attribute is used to detect the structural features such as fault, canyon and pockmark.

2.3 Figures

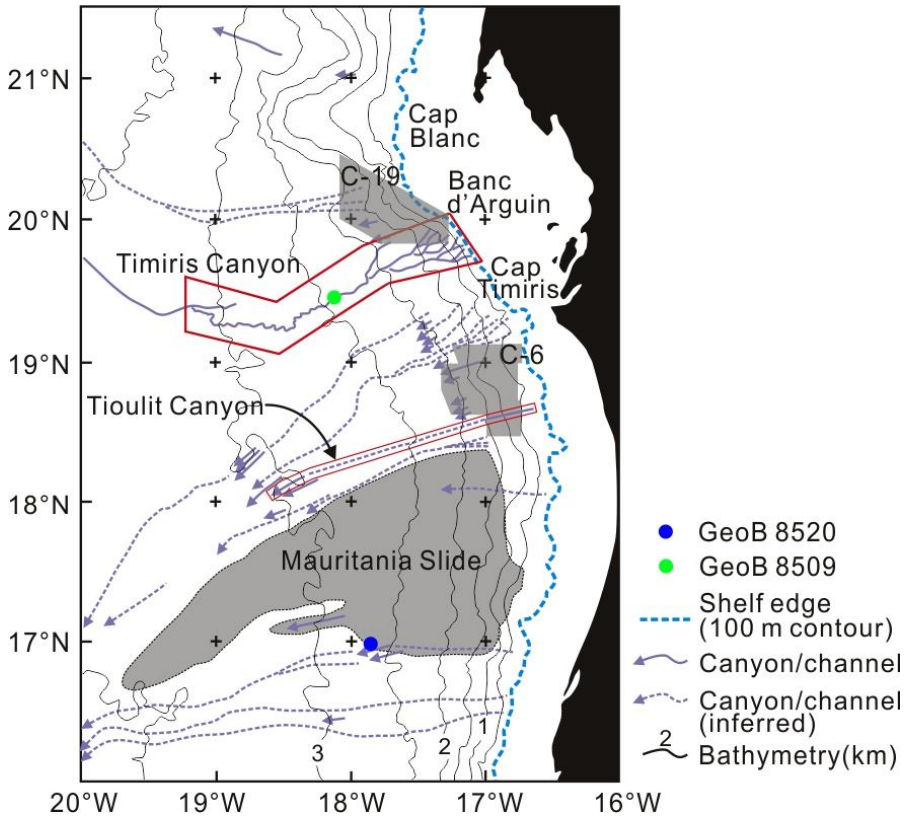

Fig.2.1 Bathymetric map showing the locations of the seismic surveys of C-6 and C-19 (after Krastel et al., 2006, their figure 3)

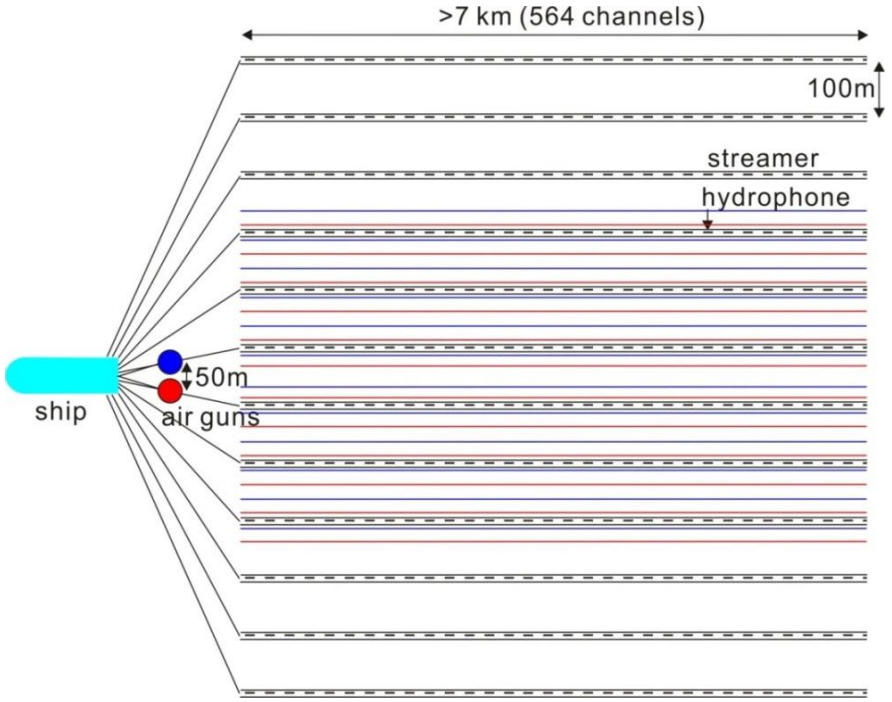

Fig.2.2 The schematic figure of the data-acquisition gear. It is based on the information of the seismic header recorded in the C-19 seismic survey. As the boat sails along, the blue and the red air gun in turns fire. The blue and red lines are the subsurface lines corresponding to the blue and the red air gun when activated, respectively. Modified from Fig.2.6 by Bacon et al., 2007.

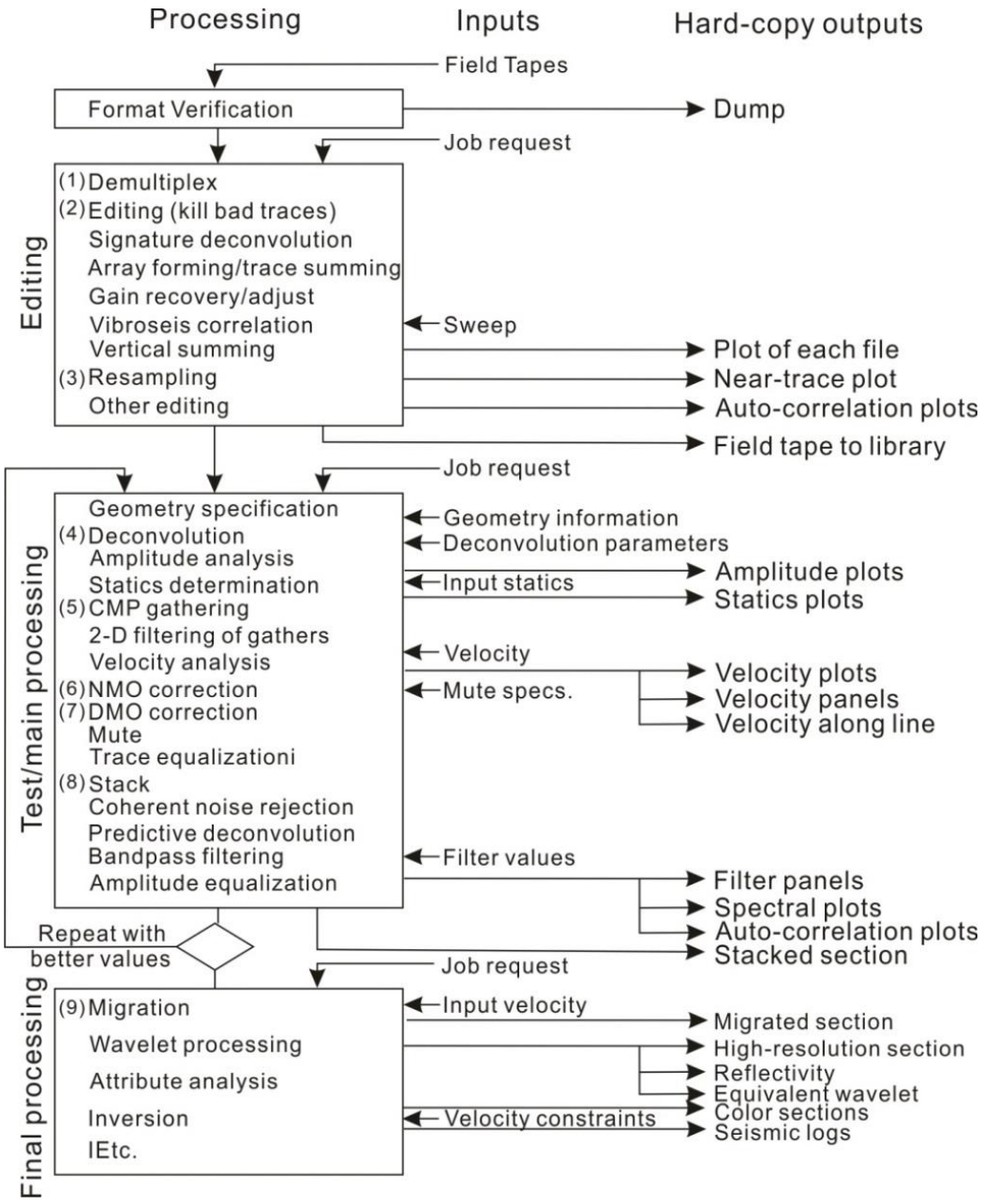

Fig.2.3 Typical processing flow chart (Sheriff and Geldart, 1995, their figure 9.62). The steps marked by (1) to (8) are introduced in the text.

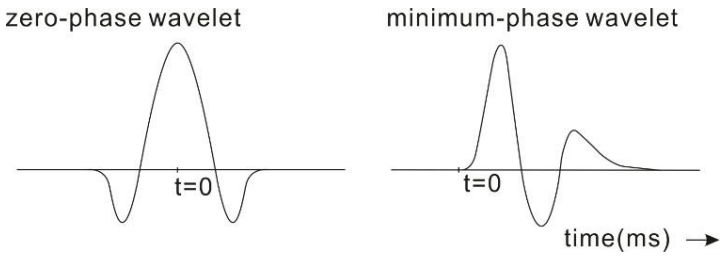

Fig.2.4 Zero-phase and minimum-phase wavelet (from http://wiki.aapg.org/Amplitude_(seismic)).

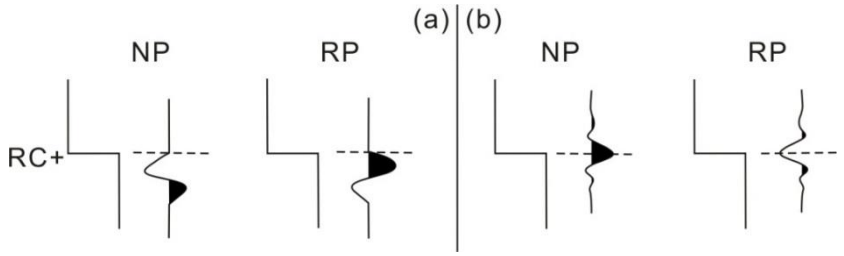

Fig.2.5 Standard polarity. Modified from Sheriff and Geldart, 1995. NP – normal polarity, RP – reversed polarity, RC+ – positive reflection coefficient.

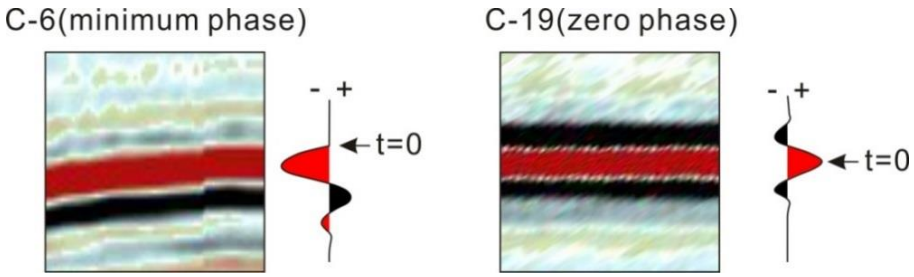

Fig.2.6 Seabed reflection and the phase wavelet in seismic surveys of C-6 and C-19.

Chapter 3 Gas Trapped below Hydrate as a Primer for Submarine Slope Failures

Ang Li [a*], Richard J. Davies [b], Jinxiu Yang [c]

[a] Centre for Research into Earth Energy Systems (CeREES), Department of Earth Sciences, Science Labs, Durham University, DH1 3LE, UK
[b] School of Civil Engineering and Geosciences, Newcastle University, Newcastle upon Tyne, Tyne and Wear, NE1 7RU, UK
[c] Research Institute of Unconventional Oil & Gas and New Energy, China University of Petroleum (East China), No.66 Changjiang West Road, Huangdao District, Qingdao, Shandong, 266580, China

Abstract:

Interpretation of a three-dimensional (3-D) seismic dataset from offshore of Mauritania reveals a shear zone at the base of a partially developed slope failure. The shear zone is at a depth of ~220 m below the seabed, immediately above a hydrate bottom simulating reflector (BSR). We propose that a paleo-gas accumulation trapped below hydrate was the primer for what would have been a substantial submarine slope failure of ~220 m thickness, covering ~50 km^2. This is based on the following observations: (a) the shear surface is, at the level of seismic resolution, coincident with some present gas accumulations located immediately below sediment that hosts hydrate; (b) there are remnants of a more extensive paleo gas accumulation that would have generated sufficient buoyancy pressure for the shear surface to be critically stressed and therefore primed the failure; (c) seismic pipes are a common seismic feature within the studied succession but absent in the area of the shear zone, which supports the hypothesis that a high gas column could have existed. This is a rare example of a shear zone that did not lead to the complete development of a slope failure. It provides the first seismic evidence that the buoyancy effect of gas below the hydrate rather than the hydrate dissociation is also a viable mechanism for large-scale slope failures.

Key words: BSR, gas accumulation, submarine failure, buoyancy, gas hydrate

3.1 Introduction

Gas hydrates are ice-like crystalline compounds, each with a gas molecule trapped by a rigid cage of water molecules (Sloan, 1998). Their occurrence is controlled by the appropriate combination of pressure and temperature conditions (Kvenvolden, 1993). They occur mostly in permafrost regions and on continental slopes where the water depth is greater than 500 m (Kvenvolden, 1993; Brown et al., 1996). The base of the hydrate stability zone (HSZ) is commonly marked approximately by a BSR on seismic reflection data. Typically, it is a high amplitude reflection with the opposite polarity to the seabed. It can cross-cut stratal reflections and mimic the geometry of the seafloor (Shipley et al., 1979).

Gas hydrates are considered to have the potential to trigger submarine slope failures, an important type of geohazard (Kvenvolden, 1993; Lane, 2002). Furthermore, the methane-dominated gases, which are thought to be liberated during failure by the removal of the overlying sediments, could escape into the seawater and potentially the atmosphere (Paull et al, 2002; Skarke et al., 2014). Methane is a potent greenhouse gas and its release from hydrate may contribute to the concentration of methane in the atmosphere (Kennett et al., 2003). Generally, two mechanisms for failure initiation associated with hydrates have been proposed (McIver, 1982; Booth et al., 1994; Sultan et al., 2004; Bunz et al., 2005; Bull et al., 2009b). Firstly, near the level of the BSR large volumes of water and gas could be released during hydrate dissociation when the base of the HSZ shifts upwards. This potentially causes liquefaction of the sediment within the zone where dissociation occurred (McIver, 1982; Sultan et al., 2004; Xu and Germanovich, 2006). The final product of such a process can include submarine slides with the gas-bearing sediment ejected laterally or glide planes and remobilized hydrate-bearing sediment transported along them (McIver, 1982). The second mechanism involves buoyancy provided by an inter-connected gas column underlying the incipient failure plane (McIver, 1982; Berndt et al., 2012). But a spatial relationship between the BSR, the gas column trapped below the hydrate in a free gas zone (FGZ) and a submarine failure has never been documented.

The objective of this paper is to describe the architecture of a shear zone for a partially developed failure and interpret a probable underlying paleo gas accumulation that was likely to have been trapped by the hydrate. These spatial relationships have not been identified to our knowledge before and are used here to support our theory on the potential role of gas buoyancy rather than hydrate dissociation as a mechanism for priming slope failures.

3.2 Geological setting

The study area is located on the passive continental margin of West Africa, ~75 km offshore of Mauritania, where sedimentary features include gullies, canyons and mass transport deposits developing on a slope with an angle of 1°-3° (Krastel et al., 2006) (Fig. 3.1). The composition of these hemi-pelagic sediments is dominated by silt-sized quartz and clay, which was mostly derived from the aeolian sediment transported from Sahara Desert (Krastel et al., 2006; Antobreh and Krastel, 2007; Henrich et al., 2008). There are other significant slope failures along the Mauritanian continental margin, for example the Mauritania slide. The area of the seafloor affected by it is ~30,000 km^2 (Henrich et al., 2008).

Several exploration wells have been drilled up dip from the landward termination of the hydrate as this region is a hydrocarbon province (Vear, 2005). To the south of the study area, Aptian, Cenomanian, Turonian and Danian mudstones are the possible hydrocarbon source rocks (Vear, 2005). According to the previous research, gas migrates vertically along a wide variety of pathways (e.g. gravity-driven faults or seismic pipes), indicated by localized or widespread high amplitude anomalies on the seismic reflection data (Davies and Clarke, 2010; Yang and Davies, 2013; Yang et al., 2013).

3.3 Seismic dataset and methodology

The 3-D seismic data, which cover an area of ~4000 km^2, have been processed by multiple suppression and post-stack time migration. These data are displayed in two-way-travel time (TWTT). The velocity is likely to be ~1800 m/s and the dominant frequency of seismic data is

~50 Hz, which together yields a vertical resolution of ~9 m (one quarter of the wavelength of the dominant frequency). The final bin spacing is 25 m × 25 m. The positive acoustic impedance is recorded as a seismic trough. The seismic response of an increase in acoustic impedance is a red-black reflection, like that of the seabed.

Four reflections have been selected as they allow the relationships between the lower boundary of the shear zone, the underlying FGZ, the seabed and the present BSR to be analyzed. The seismic attributes of these reflections have been displayed using root-mean-square (RMS) amplitude maps and dip magnitude maps. RMS is defined as the square root of the average of the squares of the original amplitudes in an analysis window. RMS amplitude maps provide information on the distribution of high amplitudes but disregard their seismic polarity. Therefore, they are useful for mapping the BSR which is an interface with a moderate to high acoustic impedance contrast. Dip-magnitude maps highlight structural features, such as faults and pockmarks (Brown, 2010; Moss and Cartwright, 2010a; Ho et al., 2012; Yang et al., 2013).

3.4 Observations

3.4.1 Seismic pipes

There are 30 seismic pipes, examples of which can be seen in the seismic cross section (Fig. 3.2a-d). On the seismic profile the typical internal features of these pipes are acoustic wipe-out or localized enhanced amplitude reflections bending upwards or downwards (Fig. 3.2a-d). Their bases are somewhat unclear but whether their tops terminate at or above BSR is easily discerned (Fig. 3.2a-d). The locations of these pipes are revealed by a dip-magnitude map which shows the positive or negative relief at the intersection between the pipes and the stratal reflections (Fig. 3.2e). More than half of these pipes are located to the northwest of the shear zone (Fig. 3.2e).

The seismic pipe is a sub-cylindrical fracture cluster that allows vertical fluid migration to by-pass the less permeable sediment (Cartwright et al., 2007; Moss and Cartwright, 2010b). Its

genesis is commonly associated with overpressured pore fluid (Cartwright, 2007; Cartwright and Santamarina, 2015). The occurrence of pipes has been extensively documented in the Lower Congo Basin (Gay et al., 2005), at the Scotian Shelf (Hovland and Judd, 1988), the Vestnesa Ridge (Petersen et al., 2010), offshore NW-Svalbard (Hustoft et al., 2009), Mauritania (Davies and Clarke, 2010), Norway (Hustoft et al., 2010), Namibia (Moss and Cartwright, 2010b) and Nigeria (Løseth et al., 2011).

3.4.2 Architecture of the shear zone

The shear zone is recognized on the basis of a number of the characteristic deformational features. In dip-parallel cross sections the down-dip displacement of the sediment is consistently tens of meters. The upper and lower boundaries are parallel (Fig. 3.3a) and merge with each other near the up-dip and down-dip terminus. The lower boundary is sub-parallel to the seabed and represents the detachment plane of the partially developed failure. We refer to this slope failure as a partially developed one because the basal shear surface did not propagate to the seabed and the translational distance was very small. The wall rocks are practically unstrained and well stratified everywhere, except on the top of the up-dip end where there are some slightly sagging seismic reflections (Fig. 3.3). These reflections may imply the volume change of the sediments at the up-dip end (Ramsay, 1980).

The shear zone is ~40 m thick, ~6.5 km wide and covers an area of ~50 km^2. At the up-dip end it is characterized by a set of the en-echelon faults (Fig. 3.3a, b). They are ~400 m in width, up to ~50 m in height and their horizontal separations are ~130 m (Fig. 3.3b). The disturbed reflections terminate here (Fig. 3.3a, b), while the ones outside the shear zone are undisturbed. The RMS amplitude map of the lower boundary shows that in planform the up-dip boundary has an arcuate geometry (Fig. 3.3c). Additionally, in planform the faults are characterized by a series of low-amplitude ridges which mimic the geometry of the up-dip boundary. All these features are similar to that of the headwall in a typical mass transport failure model, in which the sediments between the faults are interpreted as transported blocks (Bull et al., 2009a). At the

down-dip end we identify an imbricate fold and thrust system (Fig. 3.3d), which is a typical feature in failures and this has been seen in offshore Israel (Martinez et al., 2005) and Norway (Bull et al., 2009a). The thrust cannot be well detected but can be inferred empirically based on the previous research (e.g. Lewis, 1971; Martinez et al., 2005). In planform the area covered by the fold and thrust system is roughly 1200 m wide, 20 m high and the folds have an angle of dip of 5°-6°. It is characterized by a series of convex-downslope ridges, buttressed against the surrounding strata (Fig. 3.3e).

The lower boundary of the shear zone is a red-black (negative polarity) reflection (Fig. 3.4a). The strike-parallel seismic section shows that the upper boundary merges with the lower one at the southeastern and northwestern margin of the shear zone, producing a wedge-like geometry (Fig. 3.4a). In planform there is no clear difference between the amplitude values inside and outside the shear zone (Fig. 3.4b). A series of high amplitude lineations can be seen on the amplitude map of the lower boundary (Fig. 3.4c). The lineations can also be detected on the dip-magnitude map and their terminations are aligned, thereby marking the side boundary of the shear zone (Fig. 3.4d). Similar features have been seen in the Tampen Slide offshore Norway (Solheim et al., 2005, Bull et al., 2009a).

3.4.3 High amplitude at the BSR

There are three high-amplitude zones revealed by an RMS amplitude map of the BSR in the area of the shear zone (Fig. 3.5a – marked with HA1, HA2 and HA3). The area of HA1 is lobe-shaped with its western end linking to the pipe cluster and partially connected to HA2 at the eastern end of the lobe (Fig. 3.5). HA2 encompasses two high-amplitude features which both have a width of ~400 m and a geometry of the band. Their orientation is SW-NE and sub-parallel to the southern lateral margin of the shear zone (Fig. 3.5). The RMS amplitude value of the BSR is highest at the central part of each band and declines gradually to both of its edges (Fig. 3.5a). HA3 is in close proximity to the up-dip boundary and not completely within the shear zone area (Fig. 3.5a). The portion within it, which is southwest of the up-dip boundary,

displays a collection of linear features (Fig. 3.5a). The spacing between these features is consistent with that of the low-amplitude ridges at the lower boundary (Fig. 3.3).

3.5 Interpretations

3.5.1 Hydrate-capped gas accumulation

Immediately below the BSR there are a series of the high amplitude reflections which have negative polarities and form curvilinear bands in planform (Fig. 3.5b, c, d). This reflection feature is consistent with the presence of gas accumulations at the level of the BSR, which reduces the P-wave velocity and hence increases the acoustic impedance contrast (Andreassen et al., 1997; Carcione and Tinivella, 2000; Haacke et al., 2007). This interpretation is in good agreement with the typical configuration of gas accumulations underlying hydrate. It clogs the pores of the host sediment and provides an effective baffle for underlying gases (Hornbach et al., 2004; Tréhu et al., 2004; Bangs et al., 2005). Below the BSR the gas saturation calculated from the well-log and seismic data could be 1-5% (Lu and McMechan, 2002), or as high as 17% (Flemings et al., 2003) or even 90% (Tréhu et al., 2004). When the gas saturation is high (>~10%), the capillary pressure in the gas-containing sediment may exceed the displacement pressure of pore throats which is required to form a continuous filament of gas phase flow (Schowalter, 1979). We interpret these bands to be narrow, elongate gas accumulations below the hydrate. Even though most recorded values of gas saturation in the FGZ point towards a continuous gas accumulation and it has been proposed before for this dataset as an explanation for the development of seismic pipes (Davies et al., 2010), verifying that it was a connected gas column is an uncertainty.

Near the southern part of the shear zone there are nine curvilinear high-amplitude bands described by Davies et al. (2015; their fig. 2), two of which lie within the shear zone and compose HA2. The bands appear to be sub-parallel to each other, similar in width and amplitude variation. The geometry of the bands is a result of the intersection between the concave-up BSR and the flat, less steep stratal reflection cross-cut by it (Fig. 3.6b, c, d). When the BSR cross-

cuts the porous thin bed, it hosts hydrate above the BSR and gas below it, which will produce high and low acoustic impedance, respectively. As a result, at the hydrate/gas contact a phase reversal will show up on the seismic section (Fig. 3.6b, d). In HA3 some sub-vertical faults with small offset (<10m) that occur near the up-dip boundary (Fig. 3.5d). The juxtaposed high amplitude at the sides of the fault may imply the gas migration along the permeable faults.

3.5.2 Paleo-gas accumulation prior to the failure

The buoyancy effect of the interconnected gas accumulation can reduce the effective stress of the sediment (Flemings et al., 2003). In this case the sediments that have the lowest effective stress will be at the up dip, shallowest region of the gas accumulation. In the following section we will semi-quantitatively assess the role of the buoyancy in priming the failure plane. To do this we firstly estimate the extent of the paleo-gas accumulation prior to the failure. Even though three independent gas accumulations (HA1, 2 and 3) are interpreted to be trapped below the hydrate, the original geometry of the pre-failure gas accumulation may be different from what it is now. A series of dip-parallel seismic sections (an example is shown in Fig. 3.7a) reveal a potentially contiguous gas accumulation below the hydrate, although this is questioned after we observe the planform amplitude map which shows this possible paleo-accumulation is disrupted by a low-amplitude zone (Fig. 3.7b). We interpret that it did not exist until the failure happened. A portion of gas located up-dip would migrate due to the fault activation and as a result the remnant is HA3 (Fig. 3.5a). Nevertheless, the failure itself did not result in the complete leakage of the underlying gas accumulation. After the failure partially developed, most of the gas was still trapped below it. Therefore, it is very likely that these high-amplitude zones are the remnants of a spatially more extensive pre-failure gas accumulation. This pattern of fluid flow has been documented in the Eivissa Channel of the Western Mediterranean Sea, where the overpressured pore fluids play a role in the repeated destabilization of the slope sediments (Berndt et al., 2012).

3.6 Discussion

3.6.1 Buoyancy and its effect

The buoyancy effect of the interpreted paleo-gas accumulation is equivalent to that of the gas column marked in figure 7a. Its top and bottom correspond to the shallowest and deepest point of the dipping pre-failure gas accumulation respectively. We estimate the height of the gas column by using the TWTT data recorded in the seismic data and assuming the seismic velocity in the seawater and the succession to be 1500 m/s and 1800 m/s respectively. This 263 m-high gas column can produce considerable buoyancy pressure calculated by the liquid pressure formula:

$$P = \int_0^h \left(\rho_w - \rho_g(d)\right) g \, dz$$

where $\rho_g(d)$ is the density of free gas (assumed to be 100% of methane, it varies with the depth and could be calculated from the Clapeyron Equation), ρ_w is the seawater density (1.024×10^3 kg/m^3), g is the gravitational acceleration (9.81 m/s^2) and h is the height of the gas column. At the accumulation top, the pore pressure boosted by buoyancy would be sufficiently close to the lithostatic pressure, which facilitated the forthcoming failure. The effective stress of the sediment overlying the gas column, σ', has been significantly reduced (Fig. 3.7c). The shear strength can be found in (Mello and Pratson, 1999; Jeager et al., 2008):

$$\sigma'_n tan\varphi + C$$

where σ'_n is the effective normal stress, φ is the angle of the internal friction (30°, Nixon and Grozic, 2006; Jeager J.C. et al., 2008) and C is the cohesive strength (assumed to be zero, Honbach et al, 2004; Nixon and Grozic, 2006). To compare the numeric relationship between shear stress and shear strength under the guidance of Coulomb failure criterion (Jaeger and Cook, 2007), we assume the gravity of overlying sediments as the only provider for the shear stress:

$$\tau = \rho_s g h_s sin\theta cos\theta$$

where τ is the shear stress, ρ_s is the sediment bulk density (assumed to be constant, 2.1×10^3 kg/m^3), h_s is the thickness of sediments above the BSR, θ is the angle of the continental slope

(3°). The final result reveals that the shear stress exceeds the shear strength (0.27 MPa > 0.11 MPa), confirming the hypothesis that paleo gas accumulation is the potential primer for the failure. In addition, the inverse calculation suggests that the critical height of gas column required to fully prime the failure is 231 m (here we define that full priming happens when the shear stress exceeds the sediment strength). Therefore, the sediments over the top 32 m high of the paleo gas accumulation are fully primed (Fig. 3.8).

The semi-quantitative estimate of the buoyancy effect is entirely based on the 3-D seismic dataset, which will unavoidably give rise to some uncertainties. Although we make reasonable arguments that three high-amplitude zones once constituted an extensive gas accumulation prior to the failure event, its precise geometry or extent is hard to determine. The lateral migration along the base of the hydrate and changes in the position of the base of the HSZ would have led to changes in the spatial extent of the gas accumulation once the gas started to accumulate (Davies and Clarke, 2010). Furthermore, the inferred top and bottom ends of the gas column are ambiguous as they are marked by the high amplitude fading instead of sudden termination. The gradual variation of the amplitude values makes the interpretive decision of the gas accumulation margin less accurate. Therefore, determining the precise height of the gas column prior to the failure seems impossible in this case.

3.6.2 Preserved overpressure

When the base of the HSZ resets upwards, the released methane progressively adds to the gas column until the excess pore pressure can be cumulated until the shear surface is critically stressed. Such process of the overpressure build-up could be disturbed by the seismic pipes because they are good conduits with pressure communication. They are probably clusters of fractures and will discharge overpressured pore fluids to zones of lower pressure (Hovland and Judd, 1988; Cartwright, 2007; Hustoft et al, 2007; Liu and Flemings, 2007; Cartwright and Santamarina, 2015). Thus it is reasonable to speculate when pipes passing through the gas accumulation, they would have hindered the development of overpressure (Davies et al., 2010).

Only 8 seismic pipes occur within the failure area and, more importantly, all these pipes terminate below or at the BSR (Fig. 3.2e). This supports the notion that excess pore pressure could have developed at the level of the BSR in the area of the failure. In contrast, outside the failure we identify 22 seismic pipes (diameter > 100 m). In particular, 5 of these pipes pass through the base of the hydrate marked by the BSR with their tops occurring immediately below the seafloor. The presence of these pipes implies the seal by-passing at the level of the BSR (Cartwright, 2007; Moss and Cartwright, 2010b). In summary, the distribution of pipes and their spatial relationship with the BSR may indicate the possible locations where high pore pressure could have developed.

3.6.3 Dissociation-related failure mechanism

Hydrate dissociation is commonly considered as a trigger for submarine slope failure and there are models proposed for the Storegga Slide (Sultan et al., 2004) and the Blake Ridge (Dillon et al., 2001). In general, the key of this mechanism is a decomposed zone where hydrates were trapped before but later dissociated due to the sedimentation or the variation of the bottom water temperature (McIver, 1982, their fig. 4). The huge volumetric expansion during the dissociation of these hydrates can lower the effective stress and thus reduce the strength of sediment in the decomposed hydrate layer. Additionally, once dissociation has occurred the hydrates no longer play a role in the cementation and consolidation of the host sediment (Xu and Germanovich, 2006), which further reduces the effective stress and facilitates the imminent failure. According to the failure model associated with hydrate dissociation, the most likely position for the failure plane would be near the base of the decomposed zone due to its relatively high concentration of gas hydrate (McIver, 1982). We cannot be completely sure that hydrate dissociation had no role in priming this partially developed submarine landslide. But there is no evidence to support this.

3.7 Conclusions

We propose this is a rare example where the evidence for the failure mechanism is preserved because slope failure did not go to completion. Although the evidence for a contiguous gas column at the time of failure is not conclusive, buoyancy-related mechanism for submarine failure is more likely than hydrate dissociation. Our preferred model is that this process starts with a paleo gas accumulation below the hydrate and as more gases accumulated, the vertical height of the gas accumulation increased until the pore pressure reached a level such that shear strength of bedding planes was achieved and the feature was then susceptible to an external trigger. This model highlights the role of the gas accumulation trapped by the hydrate in the formation of submarine failures.

3.8 Figures

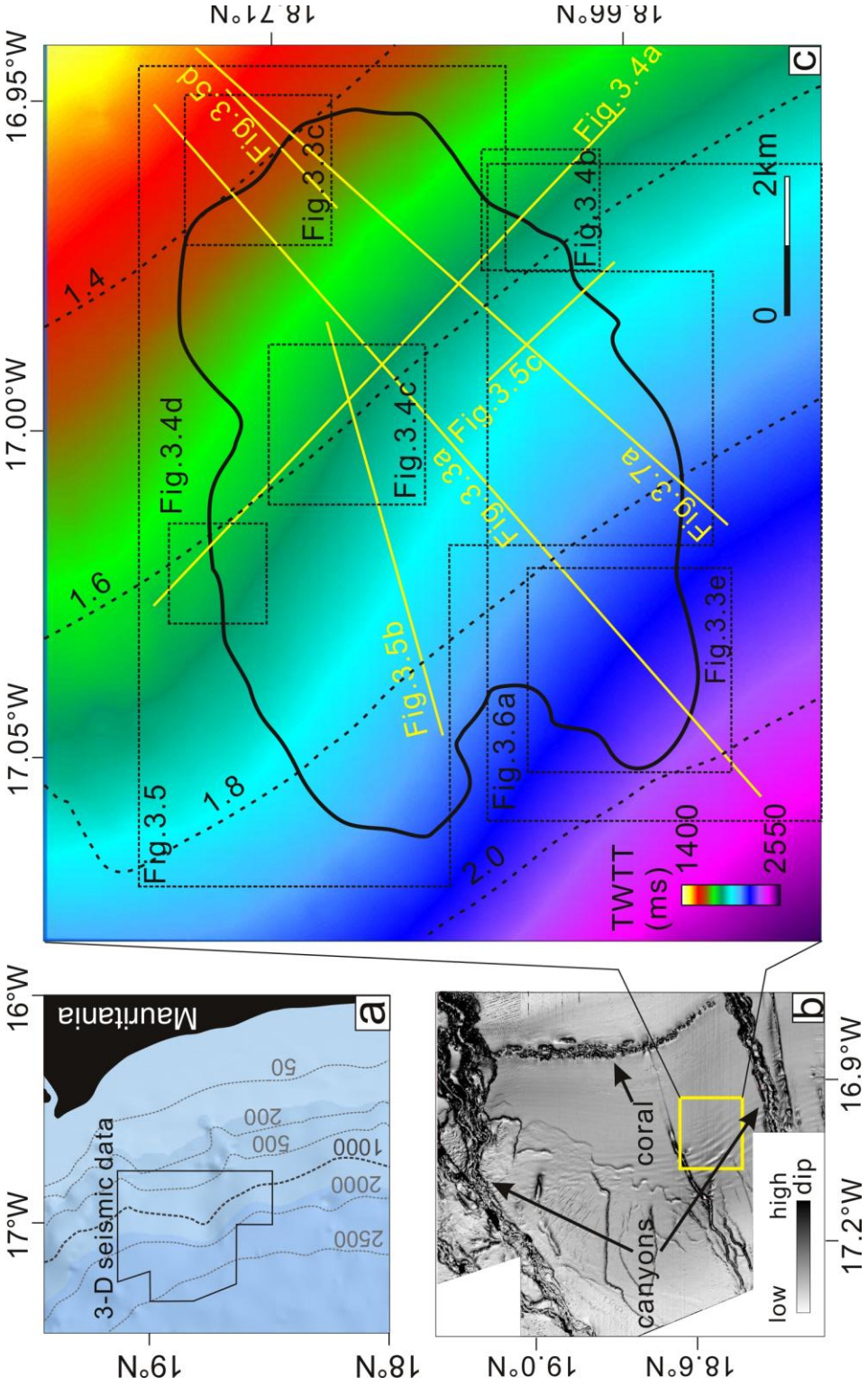

Fig.3.1 (a) Extent of the area covered by the 3-D seismic dataset and its location in relation to the bathymetry of the continental margin. (b) Dip magnitude map of the seabed revealing the main sedimentary features at the seabed. The yellow box shows the location of the study area. (c) Outline of the incompletely developed failure. The present BSR (its depth is marked in color map) is spatially sub-parallel to the seafloor (contours indicated by dashed lines, TWTT in seconds).

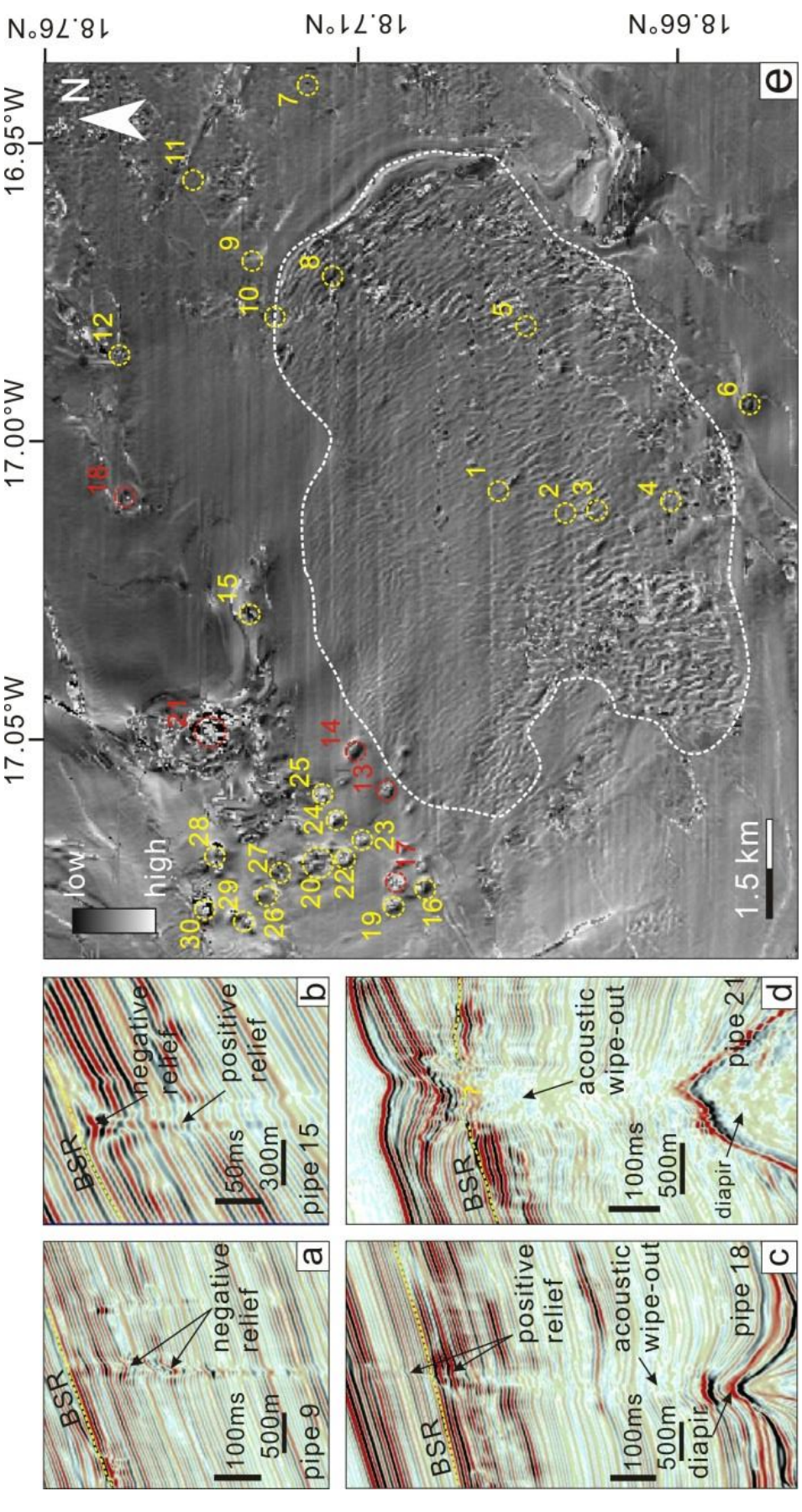

Fig.3.2 (a-d) Seismic features of typical pipes. The orientations of these seismic cross sections are not shown here. (e) Dip magnitude map of BSR, showing the location of pipes terminating at or below the BSR (marked in yellow circle) and bypassing the hydrate-containing sediment (marked in red circle). Note that no pipes penetrate the BSR in the area of the shear zone. The dashed white line marked the area of the shear zone.

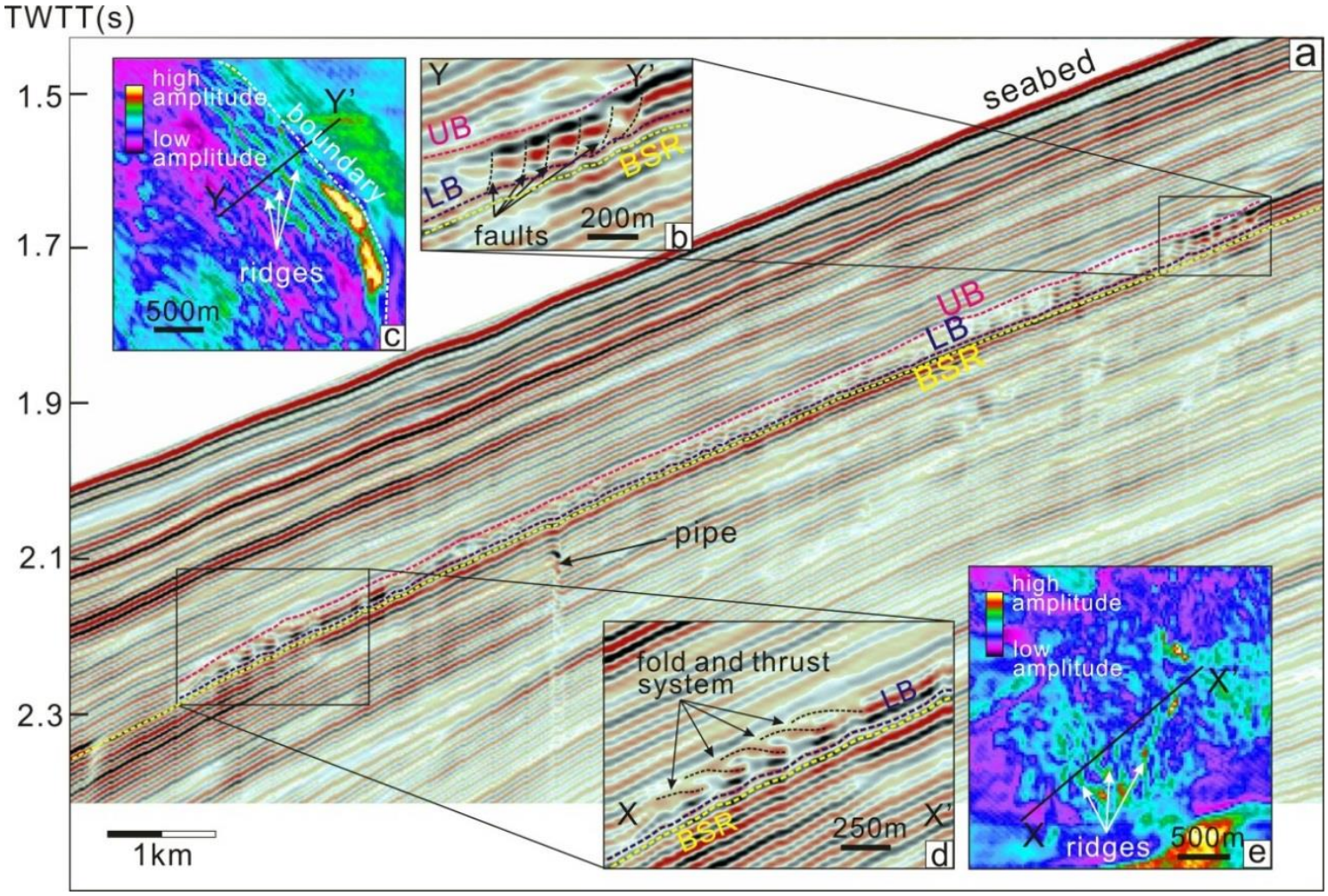

Fig.3.3 (a) A representative seismic cross section (orientation marked in Fig. 3.1c) showing the architecture of the shear zone. Note that a seismic pipe terminates at the BSR. UB – upper boundary, LB – lower boundary, TWTT – two way travel time. (b)(d) Zoomed-in images exhibiting features at the up-dip (Fig.b) and down-dip (Fig.d) end. (c)(e) RMS amplitude map of the lower boundary displaying features at the up-dip (Fig.c) and down-dip (Fig.e) end.

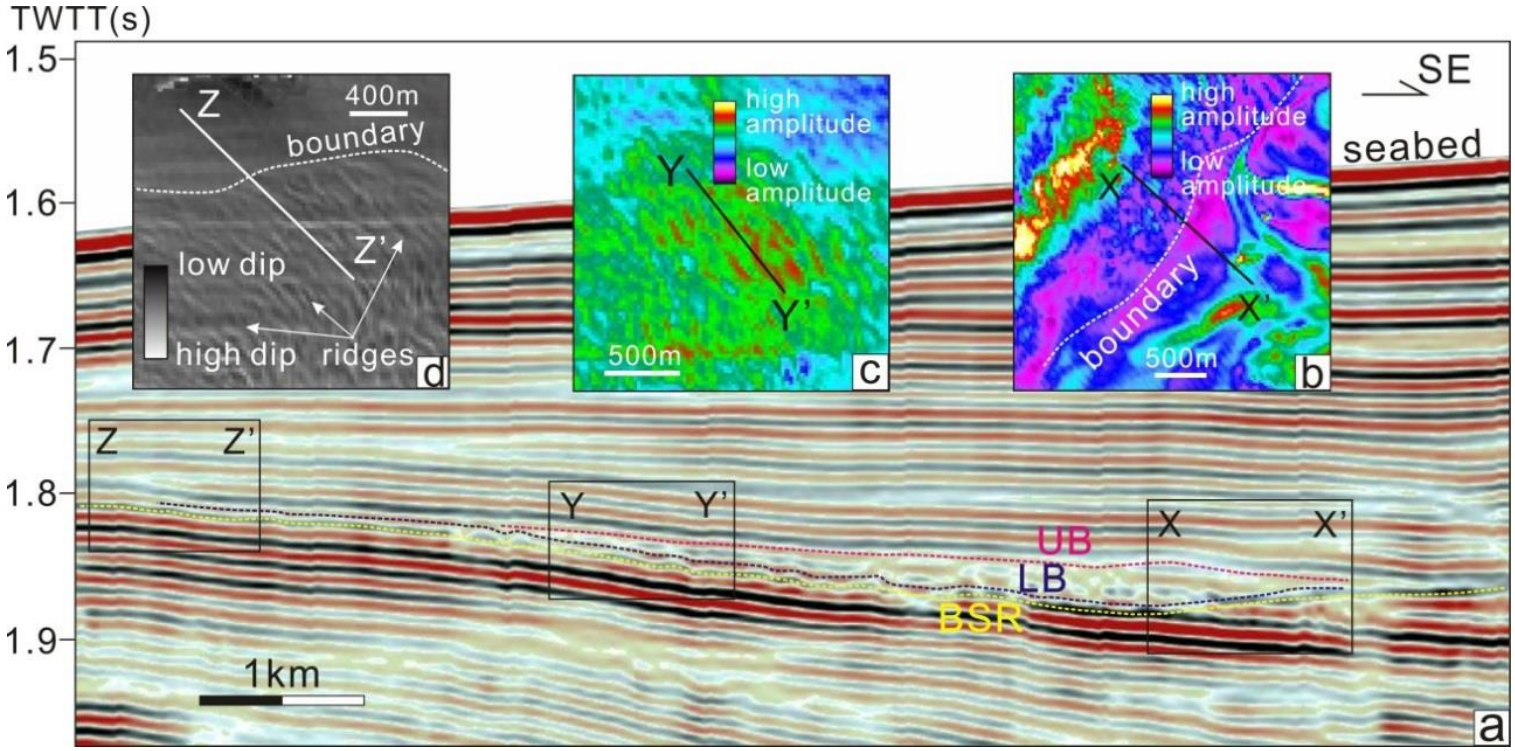

Fig.3.4 (a) A representative seismic line (orientation marked in Fig.3.1c) showing the architecture of the shear zone. (b)(c) RMS amplitude map of the lower boundary exhibiting its planform features. (d) Dip magnitude map of the lower boundary. Note the ridges occur both on the amplitude map and dip-magnitude map.

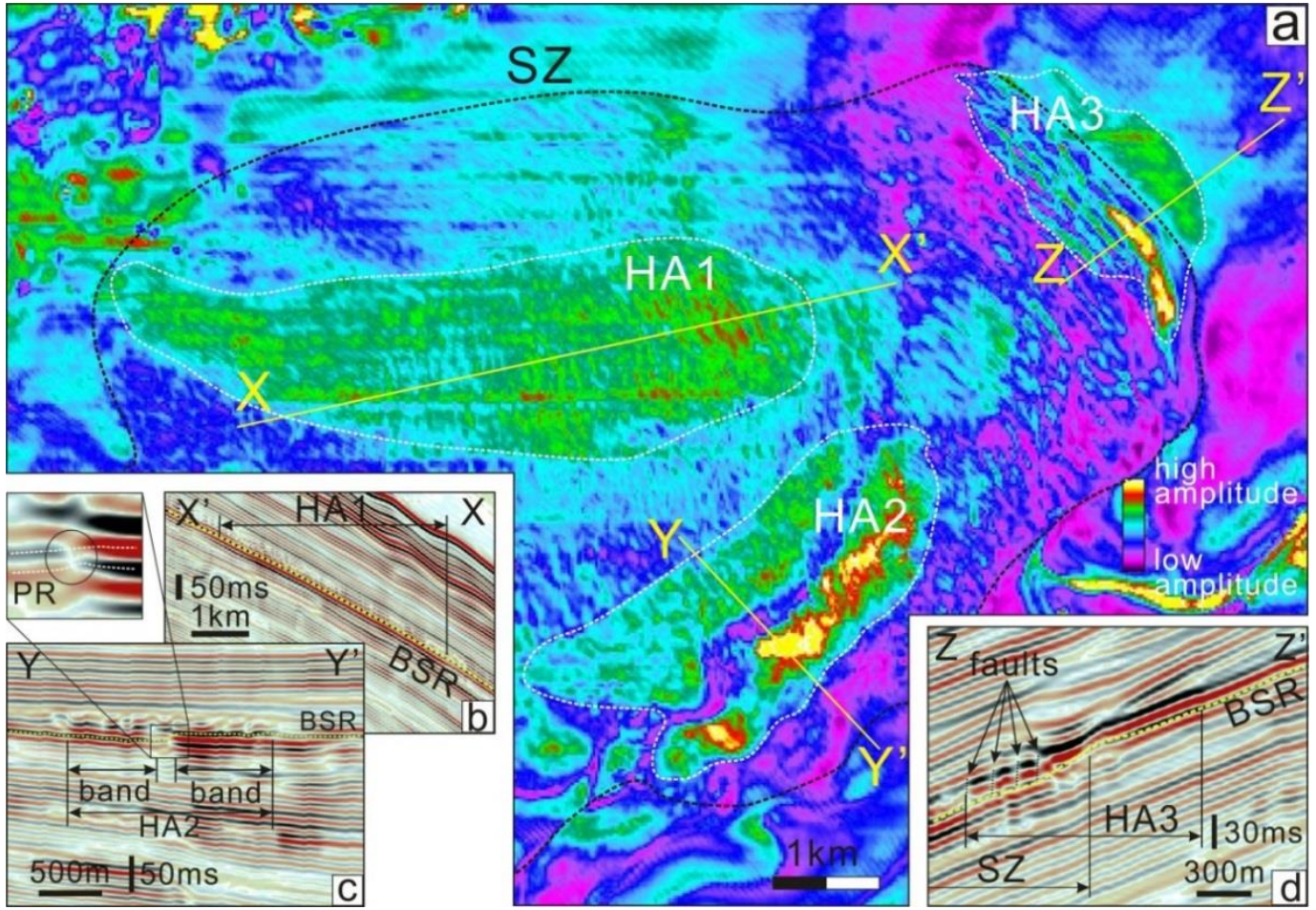

Fig.3.5 (a) RMS amplitude map of the present BSR, showing three areas with high seismic amplitude (named HA1, HA2 and HA3). The western end of HA1 is stratigraphically linked to the top of pipe clusters. Part of HA3 stays outside the shear zone and is interpreted as gas leakage. SZ – shear zone. (b-d) Seismic sections displaying high amplitude reflections within three high-amplitude areas. The 'band' is a seismic feature of the BSR, describing its geometry of high-amplitude section in planform. It is further discussed in section 5. PR – phase reversal.

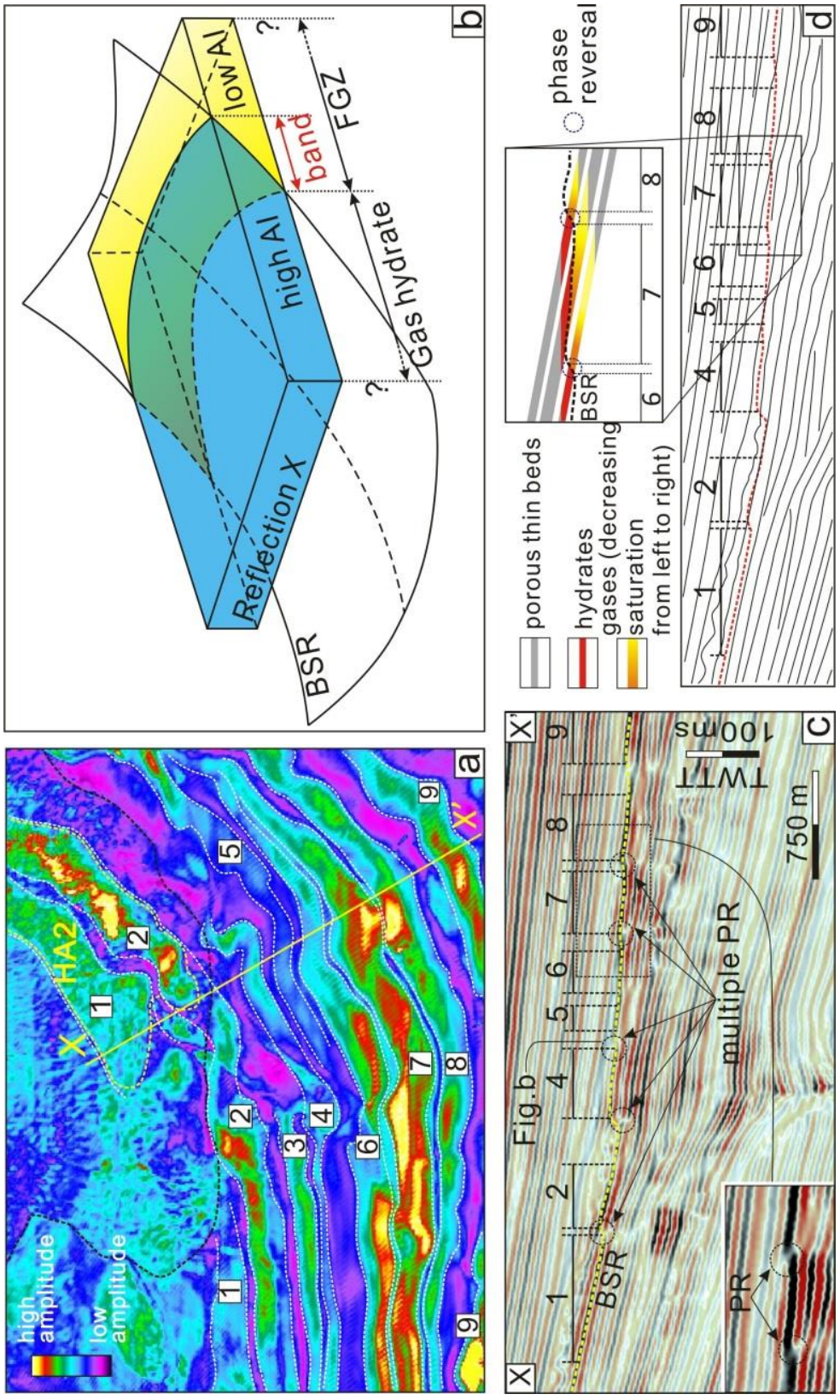

Fig.3.6 (a) RMS amplitude map of BSR showing a series of high amplitude bands surrounding the southern margin of the shear zone. (b) Schematic model of how high amplitude band formed. Reflection X represents a porous bed cross-cut by the BSR. AI – acoustic impedance. FGZ – free gas zone. (c) Seismic section showing the relationship between BSR and bands. Where strata is cross-cut by the BSR is commonly marked by seismic phase reversal. HA – high amplitude, PR – phase reversal. (d) Line drawing of figure c. The phase reversal is the result of the thin porous beds containing hydrates above the BSR and gases below it.

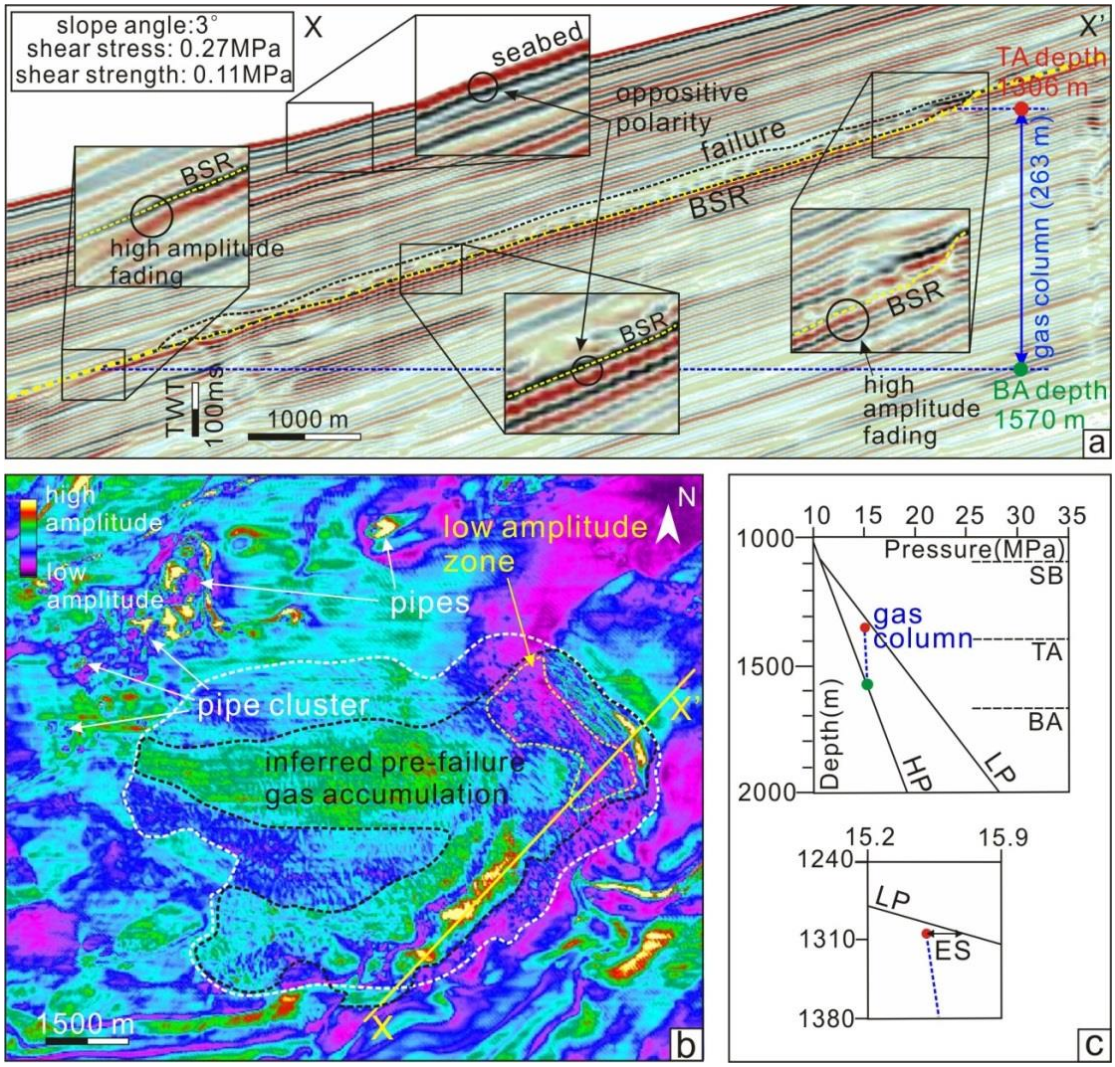

Fig.3.7 (a) Seismic cross section showing the inferred original gas column. Its extent is defined by the continuous high-amplitude reflections with seafloor-reversed polarity. (b) An RMS amplitude map of the BSR showing the possbile extent of the pre-failure gas accumulation. (c) Depth-pressure plot showing the buoyancy provided by the inferred gas column below the failure could reduce the effective stress to the degree that shear stress exceeds the shear strength. SB – seabed, TA – top of accumulation, BA – bottom of accumulation, LP – lithostatic pressure, HP – hydrostatic pressure, ES – effective stress.

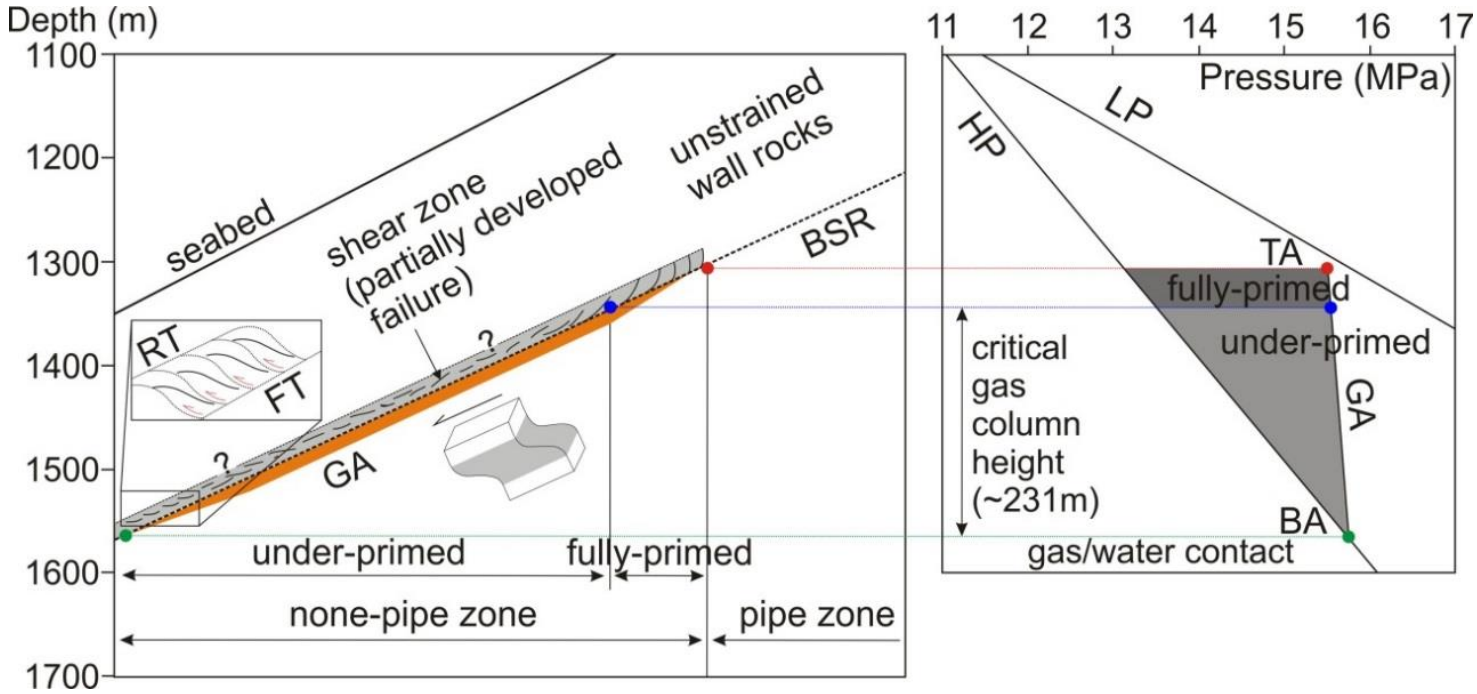

Fig.3.8 The schematic diagram of the buoyancy-related failure mechanism. The gas accumulates under the hydrate (marked by the BSR) and forms a 263 m-high gas column. It primes the overlying sediment hosting hydrate, where no pipes develop. The critical height of the gas column is ~231 m. When the shear stress is less than the shear strength, the failure plane is under-primed. HP – hydrostatic pressure, LP – lithostatic pressure, TA – top of accumulation, BA – bottom of accumulation, GA – gas accumulation, RT – roof thrust, FT – floor thrust.

Chapter 4 Methane Hydrate Recycling probably after the Last Glacial Maximum

Ang Li [a*], Richard J. Davies [b], Simon Mathias [a]

[a] Centre for Research into Earth Energy Systems (CeREES), Department of Earth Sciences, Science Labs, Durham University, DH1 3LE, UK
[b] School of Civil Engineering and Geosciences, Newcastle University, Newcastle upon Tyne, Tyne and Wear, NE1 7RU, UK

Abstract:

To what extent methane liberated from marine hydrate will enter the ocean during a warmer world is unknown. Although methane release due to hydrate dissociation has been modelled, it is unclear whether or not methane will reach the seafloor during a warmer world and therefore contribute to oceanic and atmospheric budgets. Here we show, using a new three-dimensional (3-D) seismic dataset, that some hydrate deposits surround the gas chimneys passing through the HSZ. Bottom water warming since the last glacial maximum (LGM) is speculated to cause hydrate dissociation but critically some of the released methane was not vented to the ocean. The released gas caused seal failure and free gas entered the hydrate stability zone (HSZ) through vertical gas chimneys to where new hydrate accumulations formed. This process is a new evidence for methane recycling and could account in part for the lack of methane in ice core records that cover warming events during the late Quaternary. This research provides new insight into how methane could be recycled rather than vented during a warmer world.

Key words: gas hydrate, gas chimney, BSR, methane recycling

4.1 Introduction

Methane is a potent greenhouse gas and vast quantities of it are locked in marine hydrate along the continental margins (Kvenvolden, 1993). Methane released from hydrate could have a role in accelerated climatic warming, ocean acidification and de-oxygenation (Biastoch et al., 2011; Dickens, 2003). There is already potential evidence, such as plumes of gas bubbles, for methane liberated from hydrates venting into the ocean due to oceanic warming in the Arctic (Westbrook et al., 2009) and along the US Atlantic margin (Phrampus and Hornbach, 2012; Skarke et al., 2014). But isotopic records that cover rapid Quaternary climate change events from ice cores of polar region indicate that methane from hydrate is not released during periods of rapid warming (Sowers, 2006). Methane stored in hydrate is probably a contributor rather than the main source of atmospheric methane budget after the last glacial maximum (LGM, Chappellaz et al., 1993). The fundamental question of whether large amount of methane from hydrate escapes into oceans and the atmosphere remains unanswered. If it did not reach the seabed, how is methane retained in the subsurface?

Hydrates are usually identified in marine settings through the identification of bottom simulating reflectors (BSRs) in seismic reflection datasets. BSRs mark the base of the hydrate stability zone (BHSZ) below which free gas is often trapped and this configuration yields a medium to high acoustic impedance contrast (Shipley et al., 1979). As the water depth shallows at continental margins, the BSR also shoals and seismic imaging sometimes shows examples of it intersecting the seabed at a water depth between ~350 and ~600 m (Boswell and Collett, 2011). In general the ascent of methane into the hydrate stability zone (HSZ) should be impeded, as hydrates clogs interconnected pores and fractures (Nimblett and Ruppel, 2003). But methane can sometimes pass through the HSZ and arrive at the seabed (Liu and Flemings, 2006). Seismic evidence for this methane venting is often gas chimneys with pockmark at the seabed and they are thought to represent the occurrence of vertical migration of pore fluid (Hovland and Judd, 1988; Cartwright and Santamarina, 2015).

Venting into the atmosphere is not necessarily the fate of gas that has been liberated from methane hydrate. Methane could be recycled to the BHSZ (Davies and Clarke, 2010; Paull et al., 1994), dissolved into the ocean and replaced by other gases such as oxygen during its ascent (McGinnis et al., 2006) and oxidised aerobically in the shallow ocean (Ward et al., 1987) or anaerobically in the sub-seabed sediment (Hoehler et al., 2000). Using a new 3-D seismic survey offshore of Mauritania, we consider the fate of methane liberated due to oceanic warming since the LGM as a potential scenario for how marine hydrates will behave due to a future warmer world.

4.2 Geological setting

The area covered by the 3-D seismic survey is offshore of Mauritania (Fig. 4.1) where the water depth ranges from 50 to 1800 m (Fig. 4.1b). The shelf-slope break occurs at ~120 m water depth and the continental slope dips at ~3°. In the southeast of the survey there are a number of canyons that are part of the Cap Timiris Canyon system. The study area is located between two of these canyons and covers an area of ~23 km^2 and the uppermost ~100 m of the sedimentary succession. It is most likely dominated by the fine-grained hemi-pelagic sediment interbedded with turbidite mud and sand, deposited during alternating climatic periods of aridity and humidity in the Pleistocene and Holocene (Henrich et al., 2008; Zühlsdorff et al., 2007). The gravity cores of GeoB 8507-3 (Fig. 4.1a) record the uppermost 10 m-thick sediments in the Timiris Canyon and show that the sedimentation rate averages at 190 m/my (metres per million years) in the Holocene (Zühlsdorff et al., 2007), but this rate may not be typical in the study area. This rate can be up to 685 m/my in the records of GeoB 8509-2 (Zühlsdorff et al., 2007). The commercial wells, Ras Al Baida-1 and Al Kinz-1, show that there are traces of hydrocarbons throughout late Cretaceous and Paleogene sediments (Vear, 2005).

4.3 Seismic data and methodology

The 3-D seismic data cover an area of ~3800 km^2. The bin spacing is 12.5 m × 25 m. The recording is cut by a frequency filter of 3 – 200 Hz. The dominant frequency in the upper 100 m-thick sediment is 55 Hz. These data have a sampling rate of 2 ms and are zero-phased. They are displayed in the depth domain after being Kirchoff depth migrated. The velocity model for this migration is not provided in this research. A positive polarity is defined by a peak on the seismic trace and displayed by a black-red-black seismic loop on the cross section, which represents an increase in the acoustic impedance. The extracted seismic attributes include RMS (root mean square) amplitude and dip-magnitude. The maps of these attributes are utilised to pinpoint the hydrate/gas and visualise the migration-related features (e.g. pockmarks) in an area of interest.

The BSR is picked along the troughs of the seismic traces that together produce a reflection usually cross-cutting the stratal reflections. At the places where this cross-cutting cannot be identified the BSR depth is inferred by linear interpolation or consistent with the high-amplitude, horizon-parallel reflection. A numerical model for 2-D heat conduction is used to simulate the location of the BHSZ (appendix 2) and validate the interpretation of the BSR.

4.4 Observations

4.4.1 Seabed and BSR

The seabed dips to the southwest and only one pockmark (~200 m in diameter) is found to the northeast of the landward terminus of the BSR (Fig. 4.1b). No seabed amplitude anomaly can be seen in or near this pockmark, indicating the absence of the carbonate crust that has been documented at venting sites (e.g. Hovland et al., 1987). The BSR is observable over most of the region at the water depths of 750 – 1300 m, dipping at ~4° and deepening southwestern. On a seismic profile it is characterised by a negative high-amplitude reflection and cross-cutting stratal reflections at low angles (<5°) (Fig. 4.2). The BSR does not intersect with the seabed reflection. Instead, it often terminates at ~70 mbsf (metres below the seafloor) (Fig. 4.2a). The

seabed intersection depth (SID) is estimated by the numerical model of heat conduction to be 711 m (Fig. A2.1, appendix 2), though at some sites outside the study area we observe that the SID is ~740 m.

4.4.2 Seismic chimneys and high-amplitude anomalies

4.4.2.1 Seismic chimneys

15 seismic chimneys have been identified in the study area. They are 130 – 180 m in height, 80 – 200 m in diameter and characterised by vertically aligned discontinuities in seismic reflections (Fig. 4.3). The discontinuity takes the form of a localised, sub-circular region of positive relief at each reflection above the BSR. The relief is 5 – 10 m and the diameter of the regions of positive relief maximises at the reflections D and E (Fig. 4.4). Apart from the reflections near to the top of the gas chimney (e.g. reflection B, Fig. 4.3, 4.4), those inside the chimneys have lower amplitude than surrounding reflections. The observations are similar to gas chimneys identified offshore mid-Norway (Hustoft et al, 2010). The bases of the gas chimneys are identified on the basis of where reflections show no deflection. We also see that the alignment of the bases is sub-parallel to the present BSR. The root zone is 30 – 70 m below the present BSR (Fig. 4.3). Their tops are located at the reflection immediately below the seabed but there is no evidence, such as pockmarks, for their presence at the current seabed (Fig. 4.3). The chimneys are most unlikely to be the velocity pull-up artefacts. Such artefacts are characterised by distorted reflections or obscure imaging vertically below the anomalous velocity unit, while in this case the reflections in the deep subsurface are intact and show no difference with the nearby reflections (Fig. 4.3).

4.4.2.2 High-amplitude anomalies

Around the seismic chimneys, but only detected by mapping certain reflections (D and E, Fig. 4.3c) are sub-circular, sub-elliptical or irregularly shaped high amplitude anomalies that have the same polarity with the seabed (Fig. 4.3 and 4.4). We term these ‘positive high-amplitude anomalies’ (PHAAs). They are ~70 m below the seabed and ~2.4 km away from the

termination of the BSR in the seaward direction. Chimney 10 for example, is surrounded by three regions of high amplitude, each with an irregular geometry. The high-amplitude values among these regions occur closest to the chimney (Fig. 4.4). The isolated PHAA adjacent to chimney 7 covers an area of ~0.08 km^2 and has a sub-elliptical geometry. Its long axis is sub-parallel to the dip of the continental slope. The amplitude values of this PHAA are largest near the gas chimney and diminish progressively along the reflections towards its periphery. In plan-view, chimney 7 is not in the centre of the PHAA. A third example has two associated chimneys (8 and 12, Fig. 4.4). They both are surrounded by PHAAs which coalesce to form a larger PHAA with an area of 0.21 km^2. Again in plan form these two chimneys are not central to their respective PHAAs (Fig. 4.4).

4.5 Interpretation

4.5.1 Gas trapped below the BSR

The amplitude map of the BSR shows a set of high-amplitude bands (Fig. 4.2). Similar bands have been identified before offshore of Mauritania (Li et al. 2016). In both examples they have the opposite polarity to the seabed (Fig. 4.2a), suggesting a decrease in acoustic impedance. There are also multiple phase reversals along the BSR (Fig. 4.2a, c). They occur at the edge of the band, where we predict the pores of the thin beds are filled with hydrate above the BSR and gas below it, producing high and low acoustic impedance, respectively (Fig. 4.2c). The transition of the seismic phase in a step-like pattern in space causes the aligned high-amplitude termination along the BSR. This configuration coincides with the other known marine hydrate systems (e.g. Bünz and Mienert, 2004).

Representative seismic lines where these enhanced reflections are present show that the gas chimneys root into a zone below the BSR (marked FGZ on Fig. 4.3). This spatial relationship, coupled with the knowledge that the gas chimneys are probably a migration pathway for pore fluid (Cartwright and Santamarina, 2015) implies that free gas trapped below the BSR was

transported to the shallower subsurface. Because there is no evidence for pockmarks or indeed any other morphological features at the seabed we propose there was no significant escape of methane into the ocean. Therefore, similar to Ivanov et al. (2007), the gas chimneys did not intersect a free surface.

4.5.2 Hydrate deposits

The PHAAs are interpreted to be primarily caused by gas hydrate deposits that have a higher P-wave velocity, probably between 3760 – 4000 m/s (Sloan and Koh, 2008), than that of the pore fluid of seawater filling in background sediment. A high hydrate saturation (e.g. >35%, Hornbach et al., 2003) can increase the acoustic impedance of hydrate-filled sediment to the level such that should be detected on seismic dataset. The thickness of the PHAAs is estimated to be up to ~16 m at the seismic scale based on the vertical resolution of ~8 m (the P-wave velocity of the seawater-filled sediment is assumed to be 1800 m/s and the vertical resolution is one quarter of the wavelength). But gravity cores sampled at the Timiris Canyon indicate the thickness of sands is likely to be no more than 10 m (Zühlsdorff et al., 2007). Therefore, we think the PHAA is the seismic response to one or more than one hydrate-containing porous sands.

We propose the hydrate accumulations were sourced from free gas transported through the gas chimneys. Methane carried within pore fluid migrated through the fractures and then flowed laterally along permeable beds in an up dip direction where hydrate would have formed around the chimney point source (Davies et al., 2014; Xu and Ruppel, 1999). As the PHAAs are discrete regions surrounded by lower seismic amplitudes, our preferred interpretation is that hydrate at this level was absent or at a low concentration before the chimneys formed and fed the new hydrate accumulations.

Our interpretation suggests that the geometry of the PHAA is the result of methane migration after leaving the gas chimneys. Given that the pore fluid could form a frictionless

buoyant gravity current, its spreading out will be a function of the time, the density difference, the input flux and the effective permeability of the porous medium (Lyle et al., 2005). As the base of the dipping cap rock can be considered as an inclined plane and there is a density contrast between free gas and seawater, the buoyancy has a role in driving the fluid migrating up dip, which leads to the ellipsoidal geometry of the PHAA elongated in the direction that is parallel to the dip of the continental margin (Vella and Huppert, 2006). Such a pattern of migration has been seen in the Sleipner field of the North Sea, where CO_2 has been injected into subsurface sands. The geometry of the CO_2 reservoir can be detected by the seismic imaging that displays a comparable high amplitude zone (Boait et al., 2012). Another example of this geometry is lateral migration of gas along the BHSZ offshore of Mauritania, in which case tear-drop shaped high amplitudes that loop around and envelope point-source gas chimney have been imaged (Davies et al., 2014).

It cannot be completely ruled out that the PHAAs are the seismic response to the authigenic carbonate-cemented sediment. An example outcropping at the seabed was seen in the Gulf of Mexico (Roberts et al., 2006). The carbonate cements could form as a result of anaerobic methane oxidation that develops in the methane-rich environment (Hovland et al., 1987). But the PHAAs, which are ~70 mbsf, may be too deep for this methane oxidation to take place as the sulfate-methane interface (SMI), which is at the base of the sulfate reduction zone, is normally at < 70 mbsf (Borowski et al., 1999).

4.6 Discussion

4.6.1 Methane passing through the HSZ

In general methane entering the HSZ will be trapped within it in some way or added to its base when the base of HSZ deepens, but free gas can also exist within or pass through the HSZ. Some hypotheses have been proposed to explain this phenomenon. (a) Once gas enters the HSZ, it will form hydrates, depleting pore water and therefore increasing its salinity (Liu and

Flemings, 2006). Furthermore, the hydrate clogging slows the removal of the highly concentrated ionised salt (Milkov et al., 2004). The resulting hypersaline pore environment will inhibit further hydration (Sloan and Koh, 2008) and this will allow gas for some time to pass by (Liu and Flemings, 2006; Liu and Flemings, 2007). (b) Excessive methane may consume all in-situ water to form hydrate, which will create a water-free environment in the low-permeability sediment without no more gas being trapped (Tréhu et al., 2004). In this case all the water can be depleted when the methane accounts for >70.8% of the total volume of pore fluid (the in-situ temperature and pressure are 10.23 ^{o}C and 9.54 MPa respectively). (c) Where the chimney intersects with the BSR, the base of the HSZ is redefined by the vertical intrusion of the warm advecting fluid. The perturbation zone, which coincides with the outline of gas chimney, is physically stable for gas to exist (Wood et al., 2002). Here either one or any combination of these mechanisms may contribute to the process of gas passing through the HSZ.

4.6.2 Model

We interpret that the gas chimneys did not reach the modern seabed. The vertical distance between the tops of the gas chimneys and the seabed reflection cannot be clearly identified in the seismic dataset and is probably less than 8 m (vertical resolution). Given that the sedimentation rate ranges from 190 m/my to 685 m/my (Zühlsdorff et al., 2007), the age of the gas chimneys is estimated to be up to 12 – 42 kyr. A prominent, millennial-scale warming event in the past 12 – 42 kyr is the global warming since the LGM that is interpreted to cause the upward shift of the BHSZ and hence the hydrate re-incorporation. The interpretation of this shift is consistent with those in offshore of Oregon (Bangs et al., 2005) and on the Cascadia margin (Musgrave et al., 2006). We did not rule out the possibility that this warming event could be older than the LGM due to the uncertainty of the sedimentation rate. To probe into how this hydrate re-incorporation took place, we introduce the numerical modelling.

Here we developed a 2-D finite diffusive heat-flow model that allows us to propose how the hydrate deposit formed after the LGM (Fig. 4.5, appendix). The model output of the

variation of the bottom water temperature (BWT, Bintanja and van de Wal, 2008) and the relative sea level (RSL, Siddall et al., 2003) are taken as the input into this model to predict the shift of the BHSZ since the LGM. We determine the geothermal gradient by seeing whether the modelled BHSZ at steady state has a good match with the seismic observation (35 ^{o}C km^{-1}, appendix 2). The modelling results, which are impacted by the uncertainties of the input parameters (appendix 2), show that the BHSZ probably has shoaled by ~60 m since the LGM. The thinning of the HSZ caused dissociation of the hydrate located at the BHSZ. The buoyancy of the released gas would have generated excess pore pressure that could have led to the development of hydraulic fractures (Xu and Germanovich, 2006). Therefore, the gas chimneys are interpreted to form during the period of rapid shallowing of the BHSZ. The hydrate started to accrete after the gas conduit was established between the sediments below the BHSZ and at the level of reflections D and E. Since then the hydrate accretion would continue as the BHSZ shoaled (Fig. 4.5). It is unlikely but cannot be ruled out entirely that the spatial relationship between the gas chimneys and the BSR is coincident.

4.6.3 Implications

The presence of the hydrate deposits implies that some of the gases released from hydrate since the LGM were recycled. We propose the sediments above the base of the HSZ prevent the escape of methane. The amount of methane recycled as hydrate can be amplified once this process has repeated at multiple horizons (e.g. Davies et al., 2014). But the volume of these accumulations is significantly lower than that of sediment that would have undergone dissociation after the LGM, which implies there are other mechanisms related to trapping and consuming methane. To our knowledge, they involve methane oxidisation (Treude and Ziebis, 2010), being trapped stratigraphically in situ, or recycled as new hydrate at the base (Davies and Clarke, 2010; Paull et al., 1994). To what extent methane can be re-incorporated before reaching seabed is still a question to be answered. But this mechanism is speculated to account in part for why ice cores do not record methane from marine hydrate during episodes of rapid climatic warming.

4.7 Conclusions

We found a good example for the re-incorporation of methane into hydrate during oceanic warming. Due to this warming methane released from hydrate entered the HSZ via vertical fractures and was recycled as marine hydrate. From this model we can say methane escape towards the seabed was buffered. This offers a new evidence for methane recycling that could in part explain why methane from marine hydrates is not thought to be a main contributor to the atmospheric budget.

4.8 Figures

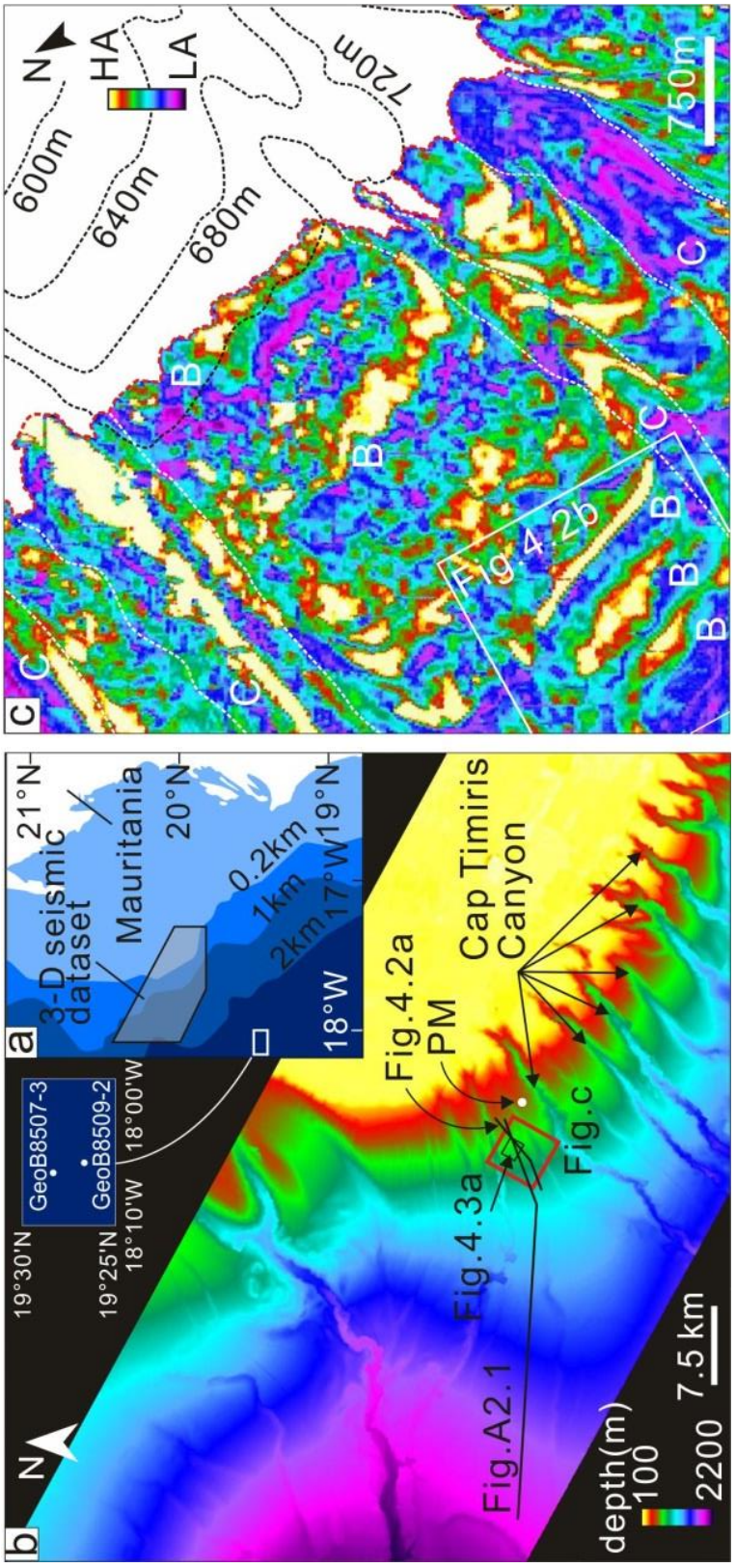

Fig.4.1 (a) Location of the 3-D seismic survey. (b) Bathymetric map showing the morphology of the seabed. Red box – study area. PM – pockmark. (c) The RMS amplitude map of the BSR in the study area. Red dashed line marks the landward extent of BSR and black dashed lines represent isobaths. The seismic features of bands (B) are interpreted in section 5.1. C – canyon, HA – high amplitude, LA – low amplitude in this and subsequent figures.

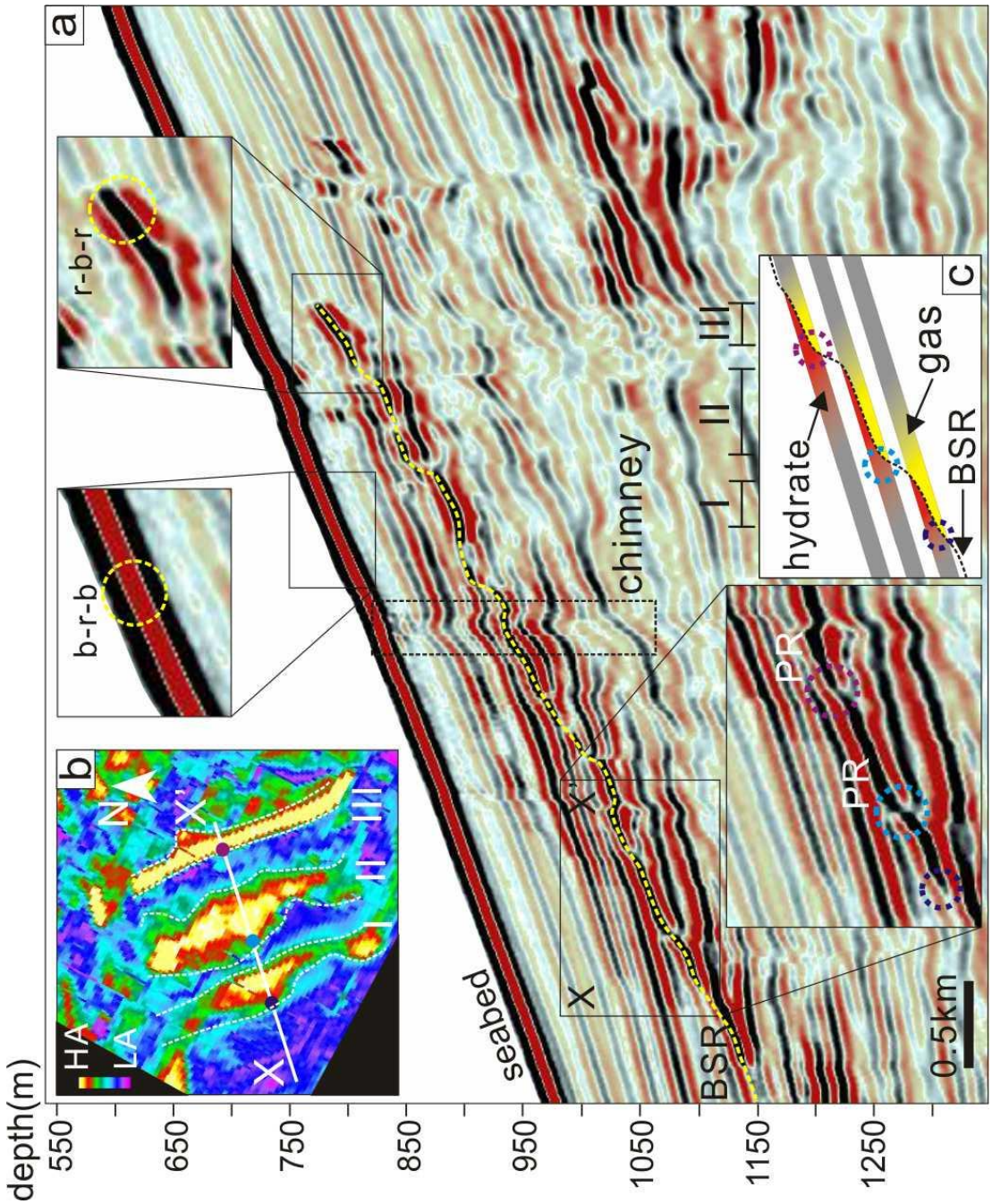

Fig.4.2 (a) A representative seismic section showing the typical features of a BSR and the gas accumulations sealed beneath it. B-r-b and r-b-r refer to the black-red-black and red-black-red seismic loop, respectively. (b) The RMS amplitude map of the BSR displaying three strike-parallel high amplitude bands (marked by I, II and III). (c) Interpretation of the cross section X-X'. At the seaward edge of the band feature, phase reversal sometimes can be seen. The grey colour represents a set of porous thin beds interbedded with less porous ones. The brighter red and yellow colours mark the higher saturation of hydrate and gas, respectively. PR – phase reversal.

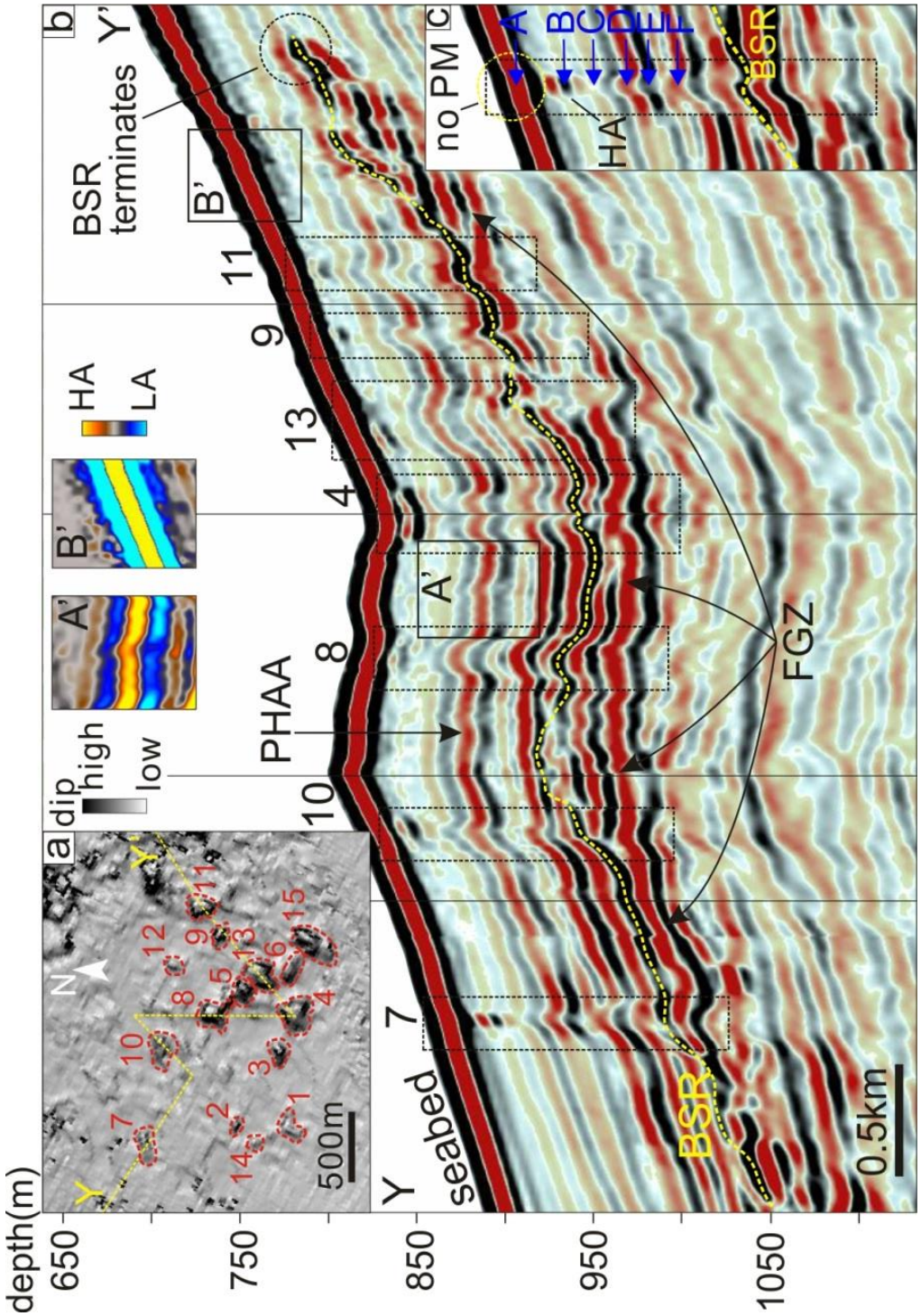

Fig.4.3 (a) Dip magnitude map of the reflection D. It is marked in Fig.c. In plan view the positive relief of the chimney is marked in the darker colour. (b) A seismic section revealing the spatial location of some seismic chimneys. They are marked by the black box. We use another colour scheme to highlight the seismic polarity of reflections of the seabed (B') and D (A'). PHAA – positive high amplitude anomalies, FGZ – free gas zone. (c) Inset of chimney 7. Six reflections (named as A–F) are picked to describe the amplitude variation around gas chimney and the result is shown in Fig.4.4. PM – pockmark.

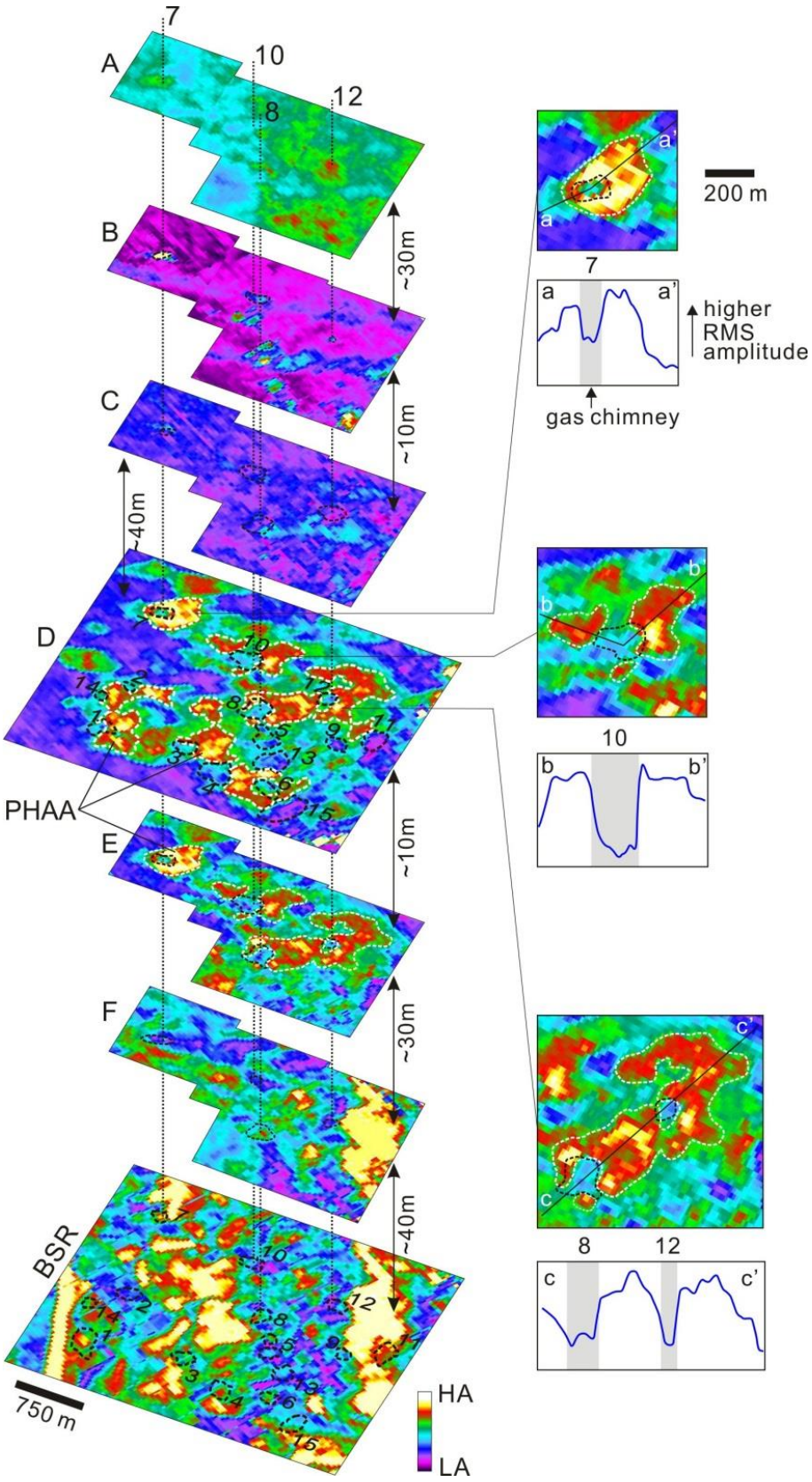

Fig.4.4 RMS amplitude map of the reflections A–F and the BSR (on the left). Their depths are marked in Fig. 3c. Vertical black dotted lines indicate the spatial location of chimneys 7, 8, 10 and 12. PHAAs at the reflection D and E (outlined by white dashed line) are identical and interpreted as hydrate deposits. Note that the amplitude values in the reflection A (the seabed) are very high and its colour scheme is different from others. The selected examples of the PHAAs are zoomed in (on the right).

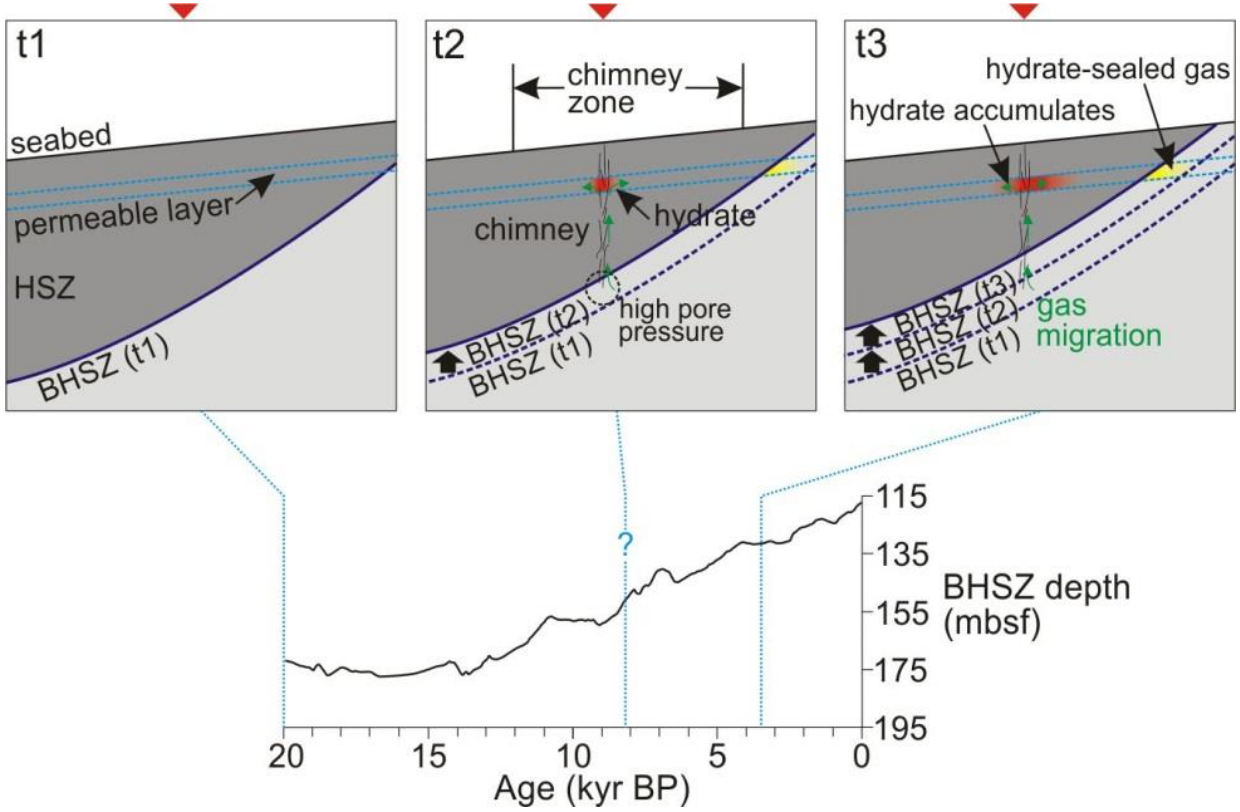

Fig.4.5 The modelling result of the BHSZ depth varying with time since the LGM. The snapshots at three timings (t1-t3) show how the hydrate deposit formed. The red triangle marks the location where the depth of the BHSZ is modelled in appendix 2.

Chapter 5 Gas venting that bypasses the feather edge of marine hydrate, offshore Mauritania

Ang Li [a], Richard J. Davies [b], Simon Mathias [a], Richard Hobbs [a], Miles Wilson [a]

[a] Centre for Research into Earth Energy Systems (CeREES), Department of Earth Sciences, Science Labs, Durham University, DH1 3LE, UK
[b] School of Civil Engineering and Geosciences, Newcastle University, Newcastle upon Tyne, Tyne and Wear, NE1 7RU, UK

Abstract:

Methane can be released from the vast marine hydrate reservoirs that surround continents into oceans and potentially the atmosphere. But how these pathways work within the global carbon cycle now and during a warmer world is only partially understood. Here we use 3-D seismic data to identify what we interpret to be a venting system that bypasses the hydrate stability zone (HSZ) offshore of Mauritania. This venting is manifested by the presence of the acoustic wipe-out (AWO) across a densely faulted succession above a salt diapir and a set of morphological features including a substantial, 260 m wide and 32 m deep, pockmark at the seabed. The base of the HSZ is marked by a bottom simulating reflector (BSR) which deflects upwards above the diapir, rather than mimicking the seabed. We use numerical modelling to show that this deflection is caused by the underlying salt diapir. It creates a trapping geometry for gas sealed by hydrate-clogged sediment. After entering the HSZ, some methane accumulated as hydrate in the levees of a buried canyon. Venting in this locality probably reduces the flux of gas to the landward limit of feather edge of hydrate, reducing the volume of gas that would be susceptible for release during a warmer world.

Key words: gas hydrate, BSR, gas venting, diapir

5.1 Introduction

Methane is a potent greenhouse gas and vast quantities of it are stored in marine hydrate, a crystalline lattice of water and methane-dominated gas (Sloan and Koh, 2008). Its susceptibility to ambient conditions makes it an unstable large carbon capacitor (Dickens, 2003; Ruppel, 2011). Long-term atmospheric temperatures could change if a small proportion of released gas entered the atmosphere (Archer et al., 2009). Therefore, understanding under what circumstances methane can bypass hydrate-bearing sediment and enter the atmosphere is important for assessing the impact of deep-buried methane on climatic change. Vigorous gas plumes in which gas bubbles rise within clusters and reach sea surface before not all of these gases are dissolved and oxidised in water body (McGinnis et al., 2006). This mechanism could take place where effective venting systems operate.

The feeder system for the gas vents can be detected by seismic imaging and can take the form of gas chimneys, which are vertically aligned reflections that probably represent clusters of hydraulic fractures (Hovland and Judd, 1988; Cartwright et al., 2007). Gas-rich pore fluid can be vented at different flux rates (Roberts, 2001). As a result, the morphological feature at the seabed can be pockmarks (Moss and Cartwright, 2010), pingoes that host hydrate in the near-seabed sediment (Serié et al., 2012) and mud volcanoes produced by the outflowing mud and water (Milkov, 2000). Gas venting from these point sources constitutes an important part of the known output of gas escaping from marine sediments (Judd, 2003).

Here we use 3-D seismic dataset to image what we interpret to be a venting system in which gas bypasses a marine hydrate accumulation and pockmarks are distributed along leaking faults. This provides a mechanism under which free gas could potentially reach shallow water. What is unique here is the spatial relationship between the feather edge of marine hydrate and the venting. Its presence prevents free gas from migrating landward, thus reducing the gas located in the most vulnerable feather edge of hydrate that is susceptible to melting during short-term ocean warming.

5.2 Gas hydrate and feather edge

In deep-water settings gas hydrates can be revealed by a bottom simulating reflector (BSR) in seismic reflection data. It marks the base of the hydrate stability zone (HSZ) and is produced by an acoustic impedance contrast between sediments containing gas and hydrate (Shipley et al., 1979; MacKay et al., 1994). This base shallows landwards until it intersects the seabed and this zone is termed the feather edge, a critical site for understanding the dynamics of marine hydrate (Ruppel, 2011; Berndt et al., 2014). Here ~3.5% of the global gas hydrate inventory is trapped (Ruppel, 2011) and warming of bottom water can destabilise the near-seafloor gas hydrate, which is evidenced by the presence of gas plumes (Skarke et al., 2014) and predicted by numerical modelling (Phrampus and Hornbach, 2012). The released methane can lead to ocean acidification and deoxygenation and perhaps climatic warming (Kvenvolden, 1993; Archer et al., 2009; Biastoch et al., 2011).

5.3 Geological setting

The sedimentary features along the Mauritanian continental slope include canyon channel systems, submarine slides and contourite moats (Krastel et al., 2006). The sedimentation rates in different locations vary considerably (Krastel et al., 2006). Core samples of up to 10 m long were recovered from GeoB 8509-2, GeoB 8520, GeoB 9624-1, GeoB 9623-2 and GeoB 9626-1 and show that the near-seabed deposit is predominately turbidite and hemi-palegic sediments (Zühlsdorff et al., 2007; Henrich et al., 2008; Henrich et al., 2010). Halokinesis is evidenced by the diapiric structures in a narrow elongate zone between 16 °N and 19 °N offshore the West Africa Continent and the age of the salt is probably Early Jurassic (Rad et al., 1982). A salt diapir (located in 18°30’N, 16°50’W) has been revealed by the negative Bouguer Anomaly. The study area is to the south of the Tioulit Canyon (Fig. 5.1). To the north seismic features of complete feather edge have been recorded before (marked by yellow box in Fig. 5.1a, Davies et al., 2015).

Two wells, Chinguetti-6-1 and V-1, have been drilled within the 3-D seismic survey and ~30 km north of the study area, confirming that the coastal basin of Mauritania is a potential petroleum province and the Cenomanian-Turonian mudstones are able to generate hydrocarbons (Vear, 2005). Seismic features linked to vertical gas migration include seismic chimneys (Davies and Clarke, 2010) and large-scale gravity-driven faults (Yang and Davies, 2013). The BSRs, either relict or modern ones, can be observed, which makes this site ideal to research methane recycling in marine hydrate system (Davies and Clarke, 2010; Davies et al., 2012a).

5.4 Seismic dataset and methodology

The 3-D seismic data cover an area of ~4000 km^2. They have been processed by multiple suppression and post-stack time migration. The final bin spacing is 25 m × 25 m. These data are displayed in two-way-travel time (TWTT). The velocity of succession investigated here is likely to be ~1800 m/s and the dominant frequency of seismic data is ~50 Hz, which together yield a vertical resolution of ~9 m. The positive acoustic impedance is recorded as a seismic trough, which is a red-black loop in the seismic profile. A good example of the reflection having such loop is the seabed one. The BSR is a black-red loop, consistent with a negative acoustic impedance contrast. The seismic attributes used here are root mean square (RMS) amplitude and dip magnitude. Both help identify bright spots (e.g. potential hydrocarbons) and structural features (e.g. pockmarks and faults), respectively (Brown, 2010).

5.5 Observations

5.5.1 Fault system and seabed morphology

13 planar faults (named F1 to F13) with a NNW-SSE trend are identified on the basis of clear offsets in stratal reflections (Fig. 5.1c). They all have a curved, concave-up geometry in cross section (Fig. 5.1c, d). There are additional faults that are not so clearly imaged due to acoustic wipe-out (AWO), particularly in the area bounded by F1, F2 and F4 (Fig. 5.2a, b). All the faults are normal, though the throw of some of the faults is indiscernible at the seismic scale. The faults have a similar angle of dip of ~50° and together form a crestal collapse graben

system (Fig. 5.1c, d). The lower tip points of the faults are located at the top of a salt diapir (Fig. 5.1d). F1, F2 and F4, which are the major faults, have a throw of <10 ms (*c.* <9 m) near the seabed and break surface whereas other faults tip out below the seabed (Fig. 5.1d). The spatial correlation between the intruding diapir and the resultant faulting pattern has been seen in other settings, for example offshore of North Carolina (Schmuck and Paull, 1993) and Angola (Serié et al., 2012).

The morphological features at the seabed include fault scarps and a set of mounds and depressions (Fig. 5.1b, Fig. 5.2). Four of them are selected for description here. Their expression at the seabed varies from sub-circular to well-rounded (Fig. 5.2g-j). The long axis ranges from 170 m to 410 m and the positive and negative deflections are ~27 – 53 m and ~32 m, respectively (Fig. 5.2). Their morphologies on the seismic profile are a symmetrical mound (II, IV) or a depression (III), or the asymmetrical complex with a combination of both (I) (Fig. 5.2). The positive relief have a comparable morphology with the Arctic ice-cored hills in Canada which are driven by growth of segregated ice or intrusion and progressive freezing of a sub-pingo water lens (Mackay, 1987).

5.5.2 BSR and diapir

The BSR is identified based on the characteristic features of high seismic amplitude and negative polarity over the area covered by the entire seismic dataset. In this case the BSR has a geometry of an elongate, upward deflection that is analogous to an anticline (Fig. 5.3a), rather than mimicking the seafloor in most cases (cf. offshore Oregon, Bangs et al., 2005). Along the intersection between the faults and the BSR we identify some examples of positive relief of ~20 – 30 m in height (Fig. 5.2d and f, Fig. 5.3a). A salt diapir is ~1050 ms (*c.* 945 m) below seabed and characterised by a chaotic internal seismic facies. Its top reflection is a red-black loop representing the same polarity with seabed (Fig. 5.2). The diapir is elongated along the NNW-SSE direction that is similar to the trend of the faults. Its hinge line is spatially coincident as the region of maximum deflection of the BSR.

The RMS amplitude map of the BSR displays some high-amplitude anomalies, most of which are within the convex upward part of the BSR (Fig. 5.3b). These anomalies, which we refer to as high-amplitude bands, have a crescent or linear geometry (Fig. 5.3b). Their strike does not coincide with the depth contour of the BSR. Their width ranges from 150 m to 500 m. For each band, the amplitude variation is symmetrical, with the highest amplitude in the middle of the band and decreasing to both of its sides (Fig. 5.3b).

5.5.3 Positive high amplitude anomalies in levees

There are a set of ENE-WSW oriented buried canyons which have a low sinuosity (Fig. 5.3 and 5.4) above the BSR. These canyons have a multistory, aggradational and laterally offset stacking pattern (Fig. 5.4a), which is similar to that of the channel-levee system in offshore Nile delta (Catterall et al., 2010). The paleo-canyons are buried 50 – 65 ms (*c.* 45 – 58.5 m) below the seabed and have a V-shaped cross-sectional morphology. The steepness of the canyon walls decreases with decreasing burial depth. Sediments filling in the canyons have sub-horizontal reflections (Fig. 5.4a). Three paleo-canyons are recognised and of our interest is the oldest one that has a width of ~450 m in seismic cross section (marked in blue in Fig. 5.4a). The depth of the channel ranges from 25 to 45 ms in TWTT (*c.* 22.5 – 40.5 m) and increases with water depth. The thalweg trend is sub-parallel to the dip of the modern seabed (Fig. 5.3b). It bifurcates near F1 (Fig. 5.4d), but the accurate location of divergence is unclear due to the overprinting effect of the BSR.

The reflections, which downlap upon the paleo-seabed G (marked in orange dashed line of Fig. 5.4a), are interpreted to represent sediments deposited in levee. Some positive high amplitude anomalies (PHAAs) are found within these reflections. These PHAAs originate from the place where the BSR intersects with F1 (Fig. 5.4c, d). They juxtapose F2 and fade out in an up-dip direction (Fig. 5.4d). The amplitude map of reflection H shows that the PHAAs occur at both flanks of the canyon, each with a wedge-like geometry (Fig. 5.4d). In plan view they are bounded by the canyon wall and F2. The maximum value of the PHAA is largest near F2 and the amplitude values decrease updip and also away from the canyon (Fig. 5.4d).

5.6 Interpretation

5.6.1 Gas venting

AWO is a seismic response to gas filling in pores of sediment, which causes decrease of P-wave velocity, severe ray bending, signal scattering and high transmission loss (Anderson and Hampton, 1980). The result of signal lost or scattered is presented as acoustic fade-out or wipe-out in the seismic cross section. The cores sampled as the shallow sediment in the Bering Sea confirmed that AWO is caused by gas (Abrams, 1992). Therefore, we interpret that the AWO zones, either ~200 m wide below the features of I–IV or km-scale wide ~300 m below the BSR (Fig. 5.2), indicate the presence of free gases and escaping of gas along faults towards the seabed.

The sub-circular depression (III, Fig. 5.2), which is a pockmark, suggests the occurrence of venting of gas-rich pore fluid (Cartwright and Santamarina, 2015; Hovland and Judd, 1988). The positive relief of I, II and IV could be the mud cone, the sediment of which is unloaded onto the seabed after being transported vertically in a liquefied way (Dimitrov, 2002). Their morphology is comparable to the mud volcanos found in the Gulf of Cadiz but of smaller dimension (Somoza et al., 2003). The rate of the migration related to formation of mud cones is documented to be fast (Roberts, 2001). Alternatively, the local up-bending of the seabed could solely result from hydrate accretion, during which pore volume will expand due to the less density of methane hydrate than that of seawater (Soloviev and Ginsburg; 1994). Such features, named as pingos, were seen in offshore of Angola (90 – 300 m in extent and 5 – 40 m in height, Serié et al., 2012) and Norwegian Sea (Hovland and Svensen, 2006), which were interpreted to suggest seepage of hydrocarbon gas. Actually when focused fluid expulsion has a varying flux, its expression at the seabed has a spectrum of features, rather than an exclusive one (Roberts, 2001; Roberts et al., 2006). In the venting system, the flux rate may vary with time and space, thus it is likely that some features mentioned above may occur in a locale simultaneously and

their seismic features could overprint on each other. Overall, the presence of these features coupled with AWO is compelling evidence of gas bypassing the feather edge of marine hydrate.

5.6.2 Gases trapped below the BSR

In seismic reflection data high-amplitude bands (Fig. 5.3d) are a common seismic response to the interface between hydrate-bearing sediments above the BSR and gas-bearing sediments below it (Davies et al., 2015). Similar features have been described before by Li et al. (2016) in the same seismic survey. Most of the bands here are within the upwarping region of the BSR (Fig. 5.3b). The relief in the BSR creates a trapping geometry for free gas (Kvenvolden, 1993). Furthermore, under the eastern flank of the upwarping BSR we found a set of flat spots (Fig. 5.3a), an evidence for the phase boundary between gas and water, or gas and oil (Brown, 2010). Therefore, we interpret that free gases are trapped below the BSR.

5.6.3 Hydrates hosted in levee sediment

Silty sand can be found in the cores sampled in levee successions near the seabed (Henrich et al., 2010) and it potentially traps gas and hydrate stratigraphically. Hydrate filling in pores of sediment can increase its acoustic impedance to the level such that it can be displayed as enhanced reflections in seismic data because of a higher P-wave velocity of methane hydrate (3750 – 3800 m/s, Helgerud et al., 2009). We interpret the PHAAs (marked in Fig. 5.4d) as an isolated methane hydrate trap. The fact that the PHAAs have lower amplitude than the BSR coincides with the synthetic seismic result which reveals that in marine sediment gas/hydrate phase boundary normally has a higher acoustic impedance contrast than the hydrate/brine interface (Zhang et al., 2012).

The amplitude variation of the PHAAs at reflection H may be the result of gas migration. Based on the AWO, we interpret that gas breached the sealing at the level of BSR near the intersection between faults and reflection H. If this gas could migrate along the levees,

Darcy's law would allow us to predict that the concentration of hydrate converted from gas decreases with distance towards up dip. This result is consistent with amplitude variation at reflection H. An alternative explanation for the amplitude variation in the PHAAs is the distribution of pores of sediment, the prediction of which can be guided by sedimentology. In a channel-levee system the coarser-grained sediment was unloaded near the channel, while the finer-grain one in distance. Given that the primary pores narrowed uniformly after compaction, the sediment near the channel can host more hydrate than that far away from channel. However, which factor controls the amplitude variation is uncertain in this case.

5.7 Discussion

5.7.1 BSR doming

The upward deflection of the BSR has been seen before (Hornbach et al., 2005) and is attributed to the underlying salt diapir which has a higher thermal conductivity and hence changes thermal regime. Here to test whether the salt diapir affects the BSR depth, we assume the thermal conductivity of the salt (6 W m^{-1} K^{-1}, Hornbach et al., 2005) then use the 2-D heat conduction modelling. Its steady state can be expressed as:

$$k_x \frac{\partial^2 T}{\partial x^2} + k_z \frac{\partial^2 T}{\partial z^2} = 0$$

where T is the sediment temperature, x and z are the sediment length and depth below the seafloor, respectively. k_x and k_z is the sediment thermal conductivity in the horizontal and vertical direction, respectively. The subsurface sediment is assumed to be isotropic and homogeneous, hence k_x=k_z. We obtain the pressure profile by assuming the hydrostatic pressure gradient of 10.09 MPa/km. Ocean temperature data used here are same with those by Davies et al. (2012). The BSR depth is determined by the intersecting point of geotherm and methane hydrate stability curve (we assume gases are 100% methane). The latter has been quantified by Lu and Sultan (2008) and a correction of seawater salinity of 35 ppt on this stability curve is made. The 2-D steady state equation is then discretised in space using finite

differences and solved using MATLAB's MLDIVIDE function. Any middle point of two known neighbouring points A and B at either side of a boundary has a thermal conductivity k_{AB}:

$$k_{AB} = 2(1/k_A + 1/k_B)^{-1}$$

where k_A and k_B is the thermal conductivity at point A and B, respectively. This modelling is first used in the places where the BSR mimics the seabed to get the geothermal gradient fitting best with the seismic observation ($32^oC\ km^{-1}$), then in the study area.

The result shows that the modelled BSR has a good match with the observed one, particularly across the crest of the diapir (Fig. 5.5). This implies that the salt diapir changed the thermal regime and hence controls the geometry of the BSR. This increases the vertical relief of the BSR and therefore the relief of the trap. We speculate that some of the local mismatches, in particular the ones characterised by the local positive relief that is ~100 – 300 m wide adjacent to some of the faults (marked by the right two black arrows in Fig. 5.5), may be caused by warm focused flow that leads to local hydrate re-equilibrium (Crutchley et al., 2014). Therefore, the BSR relocation is the result of heat transfer in the form of diffusion coupled with local advection. However, there are some uncertainties that lead to the inaccuracy of the modelling result. Salt carried by focused fluid along the faults, which is not considered in the model, may increase the local salinity in the near-BSR sediment. Ionised salt can hinder hydration, leading to the localised thinning of the HSZ (Sloan and Koh, 2008). Uncertainties in the modelled BSR depths may also stem from error estimates of geothermal gradient, sediment conductivity, velocity model in the subsurface and temperatures at the seabed.

5.7.2 Implication

In general, hydrate-bearing sediment is an effective barrier for free gas during its ascent in the subsurface (Nimblett and Ruppel, 2003). Occasionally this gas can reach the seabed by itself, such as when the pore pressure of its reservoir in a hydrate province reaches a level that the fault slip can occur (Hornbach et al., 2004). Given that the trap created by the BSR relocation is fully charged, the height of the gas column of the formed gas accumulation is

estimated to be no more than 50 ms (*c.* 45 m). This height of gas column is significantly lower than the critical height recorded in the Blake Ridge (~150 – 290 m, Hornbach et al., 2004). Furthermore, we see no seismic evidence of the presence of thick free gas zone. This suggests that the capillary entry pressure of overburden sediment along fault is lower than that of the unfaulted sediment and this offers permeable route for gas to reach the seabed.

A BSR is present over the study area but mostly absent landward of it (Fig. 5.6a-c). This is different from the area (marked in yellow box, Fig. 5.1a) to the north where sedimentary context is similar but the BSR can be commonly observed (Davies et al., 2015). An explanation for its absence landward is that methane venting above the diapir prevents landward gas migration (Fig. 5.6d). Absence of free gas near the landward limit of the feather edge implies less methane will be susceptible to being released in a warmer ocean in the future. Therefore, diapirism could release methane into the ocean before it gets warmer and melts the marine hydrate hosted in the sub-seabed sediment. Methane vented under this circumstance has high flux rate when leaving the seabed and is likely to reach the shallow water or, possibly, the atmosphere (McGinnis et al., 2006).

5.8 Conclusions

3-D seismic data provide compelling evidence for the occurrence of a gas venting system, offshore Mauritania. A salt diapir provides the conditions to create migration pathways for focused fluid of free gas that bypasses the feather edge of marine hydrate. The presence of this system inhibits gas migration landward into the shallow feather edge region. This reduces the volume of methane that would be susceptible to a warmer world in the future.

5.9 Figures

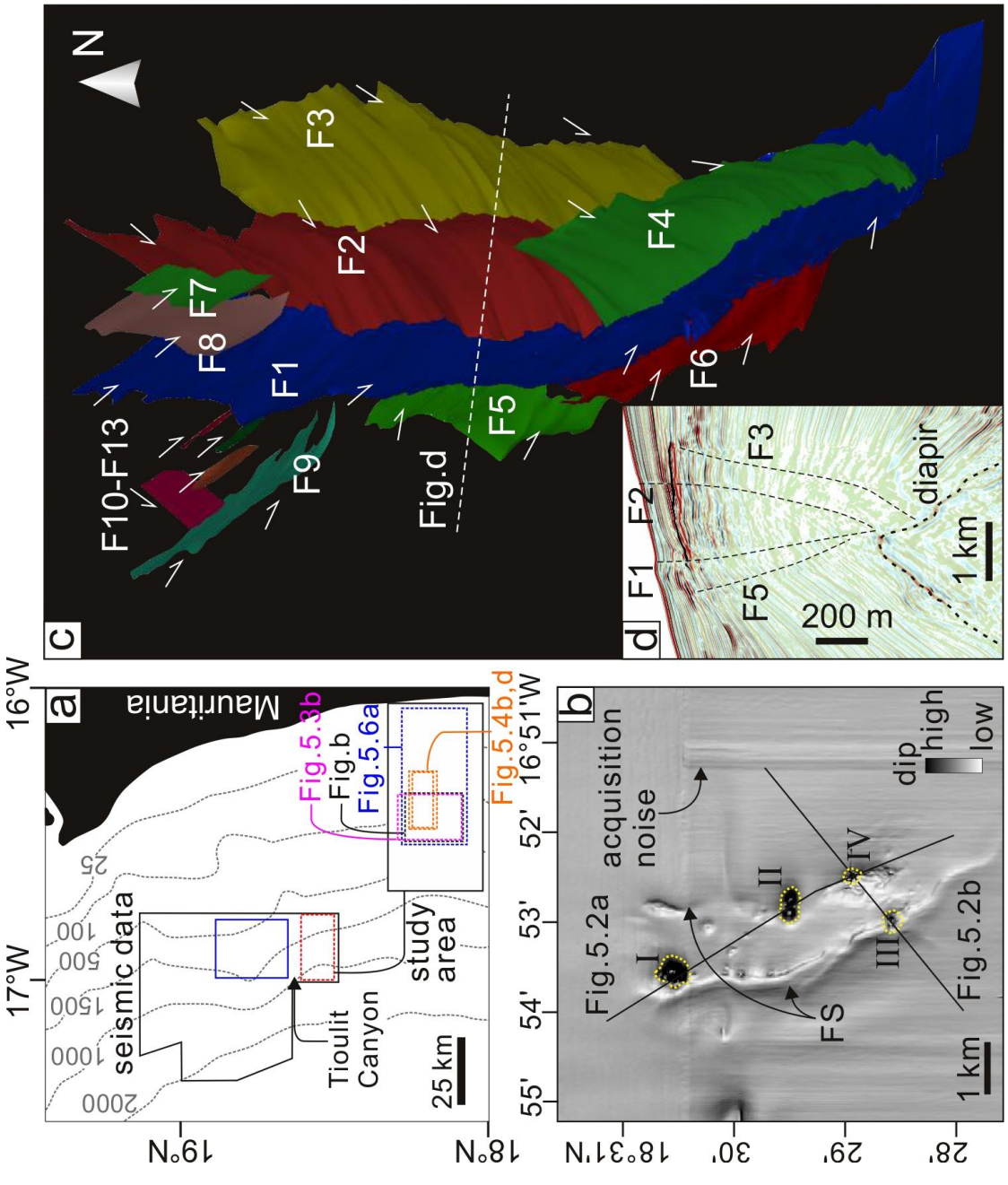

Fig.5.1 Extent of the area covered by the 3-D seismic survey and the location of the study area. The blue box of solid lines marks where the relatively complete feather edge was described by Davies et al. (2015). (b) Dip-magnitude map of the seabed in the study area showing the fault scarp and some reliefs (named as I, II, III and IV). FS – fault scarp. There are some linear features caused by acquisition noise and they are parallel to the inline direction. (c) 3-D imaging of the faults (named as F1–13) from top view. The white arrows mark the displacement direction of the hanging wall. Please note not all the faults terminate at the seabed. (d) A representative seismic cross section showing the pattern of the faults and their spatial relationship between the underlying salt diapir.

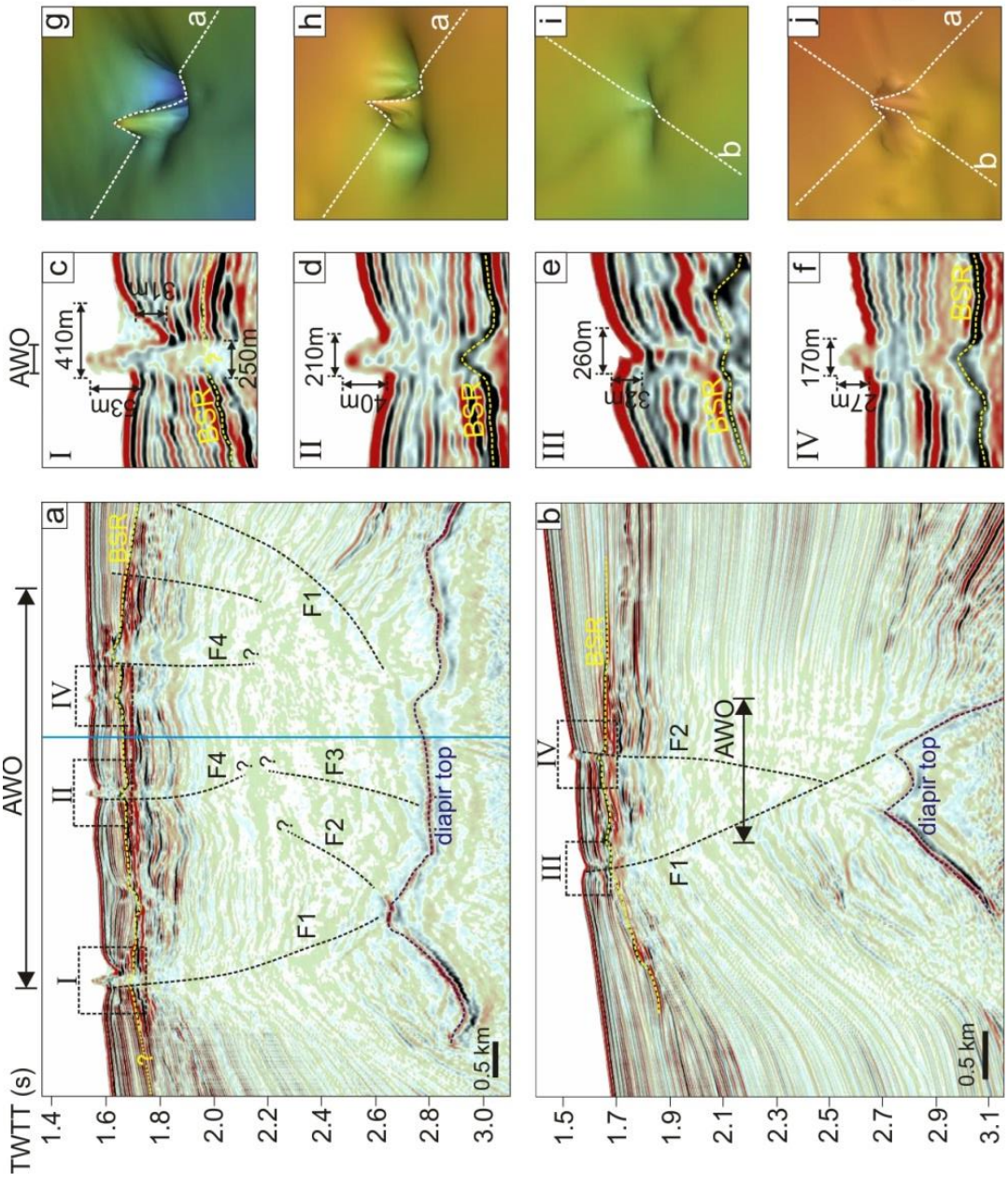

Fig.5.2 (a–b) Representative seismic cross sections displaying the spatial relationship between the reliefs at the seabed, the faults and the salt diapir. The acoustic wiping-out (AWO) shows up below I-IV and in the zone bounded by F1, F2 and F4. (c–f) Zoom-in figures showing the cross-sectional geometry of I-IV. (g-j) 3-D imaging of the bathymetry exhibiting the morphology of I-IV.

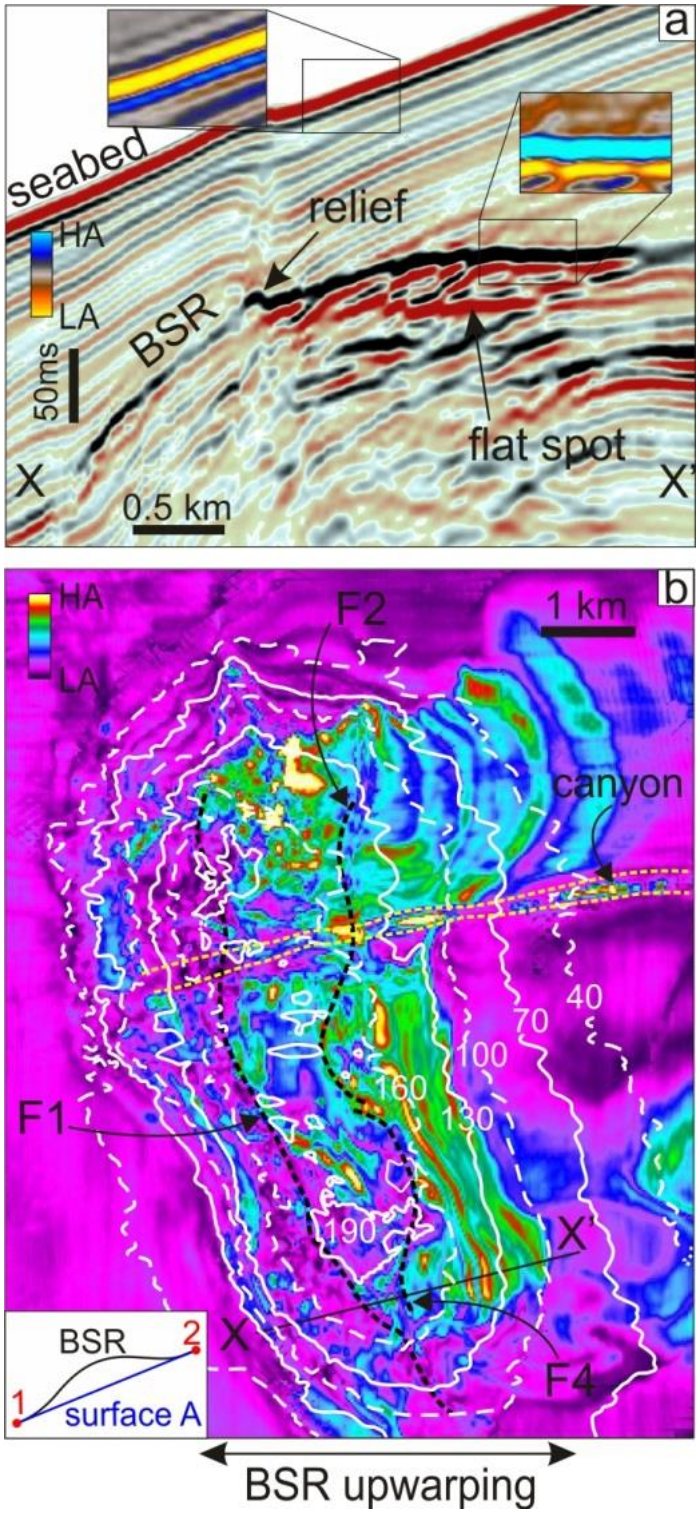

Fig.5.3 (a) A seismic cross section showing the upwarping section of the BSR. A different colour scheme is used to highlight its polarity (cyan-yellow loop) that is opposite to that of the seabed reflection (yellow-cyan loop). A flat spot is found under the upwarping BSR. Please note that this figure is exaggerated vertically. HA – high amplitude, LA – low amplitude in this and subsequent figures. (b) RMS amplitude map of the BSR. The white lines are the contours of the vertical distance (measured in ms, TWTT) between the BSR and surface A. Surface A is an assumed planar surface and on each cross line (E-W oriented) it is a segment defined by the down-dip (1, marked in inset) and the up-dip point (2) along the BSR. The yellow dashed lines mark the outline of a buried old canyon and it is described in section 5.6.3.

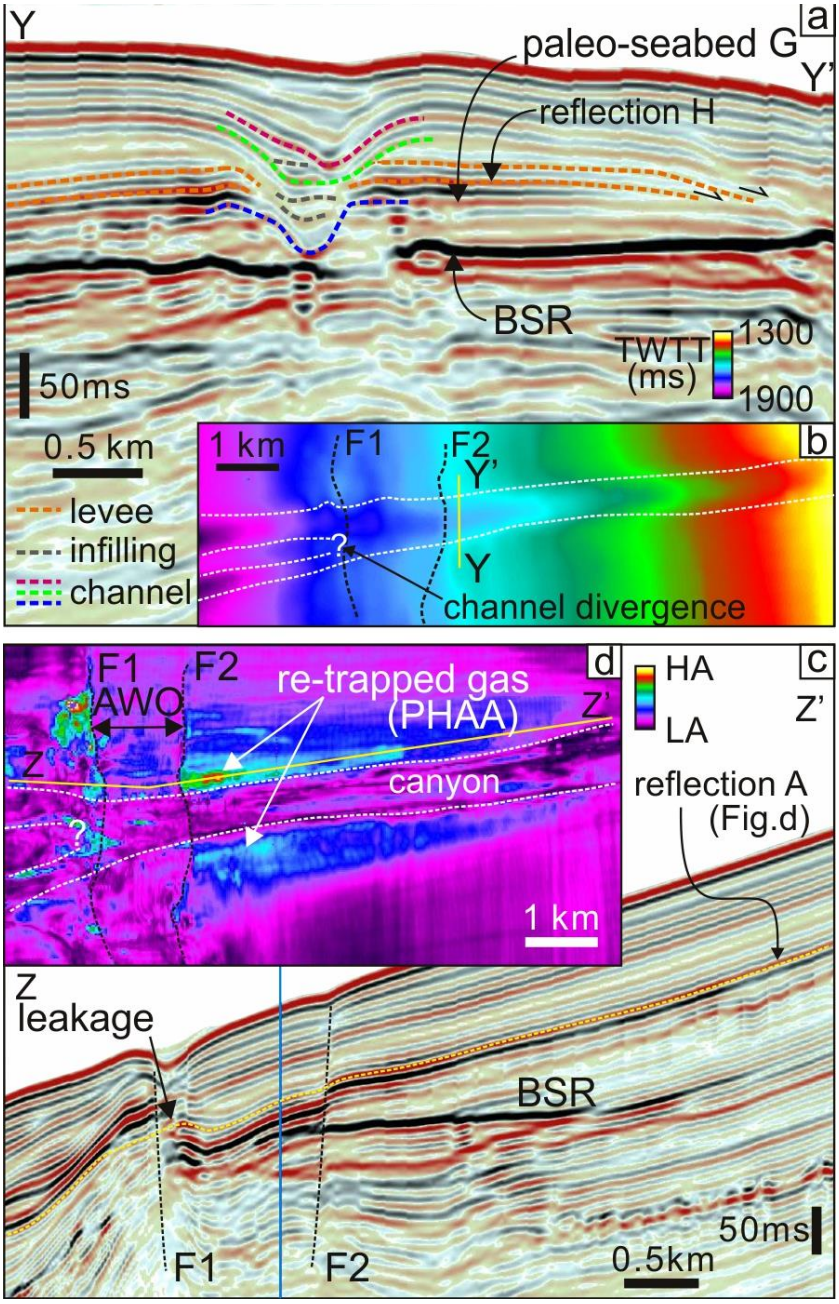

Fig.5.4 (a) Seismic cross section displaying the vertical stacking pattern of the multistory channel-levee systems. Reflection H, which is interpreted as the levee sediment hosting hydrates, downlaps upon a paleo-seabed G. (b) Map showing the depth of the paleo-seabed G. The place in where the old channel diverges is not clearly shown by the seismic dataset. (c) A seismic cross section showing the spatial relationship between the BSR and the reflection H. (d) RMS amplitude map of the reflection H. Some positive high amplitude anomalies (PHAAs) show up at both sides of the buried canyon.

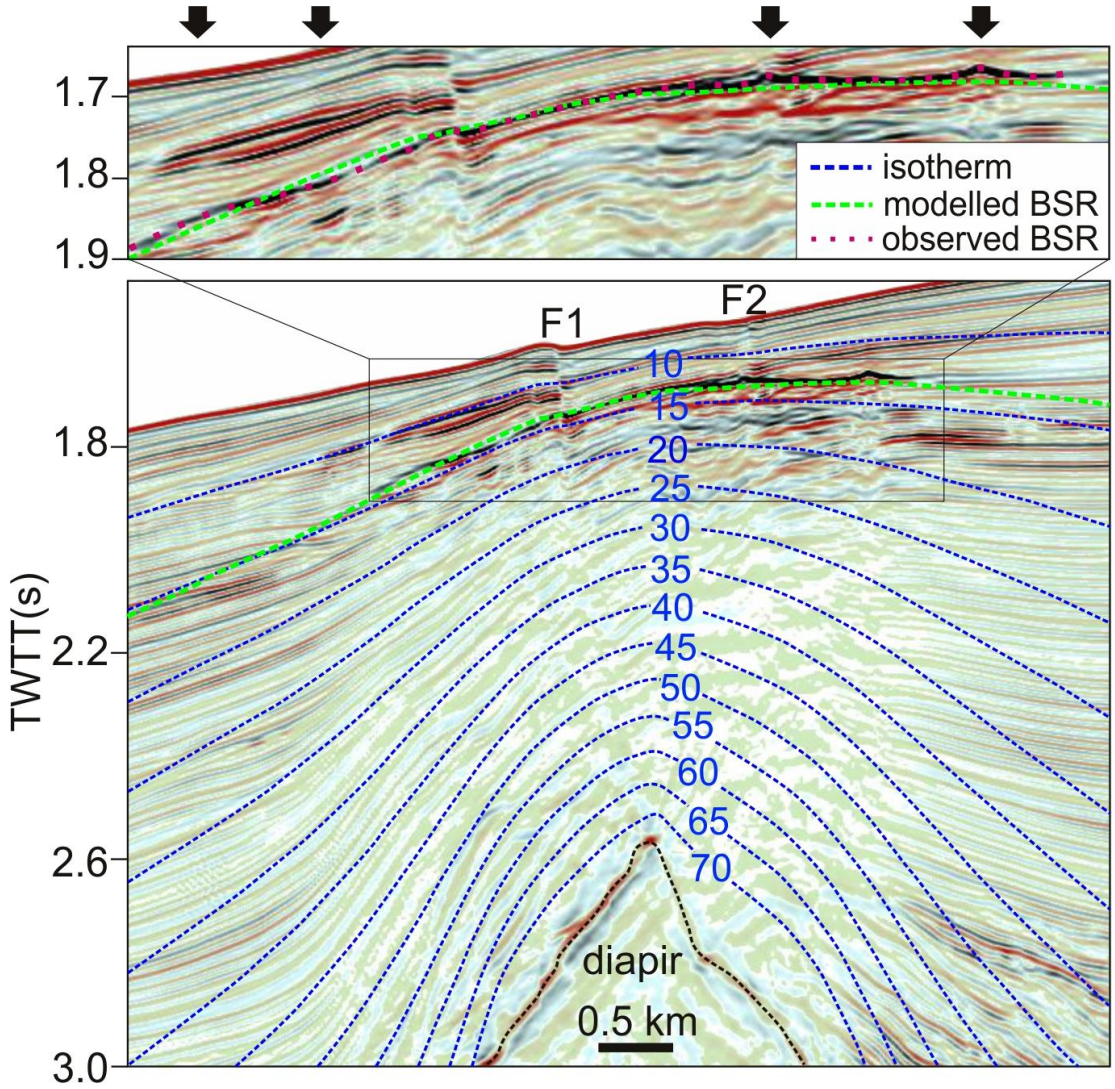

Fig.5.5 Modelling result of 2-D heat conduction. The black dashed line marks the top of the diapir. The blue numbers indicate the temperature of each isothermal line. The black arrows mark the places where there are some minor discrepancies between the modelled BSR and the observation result.

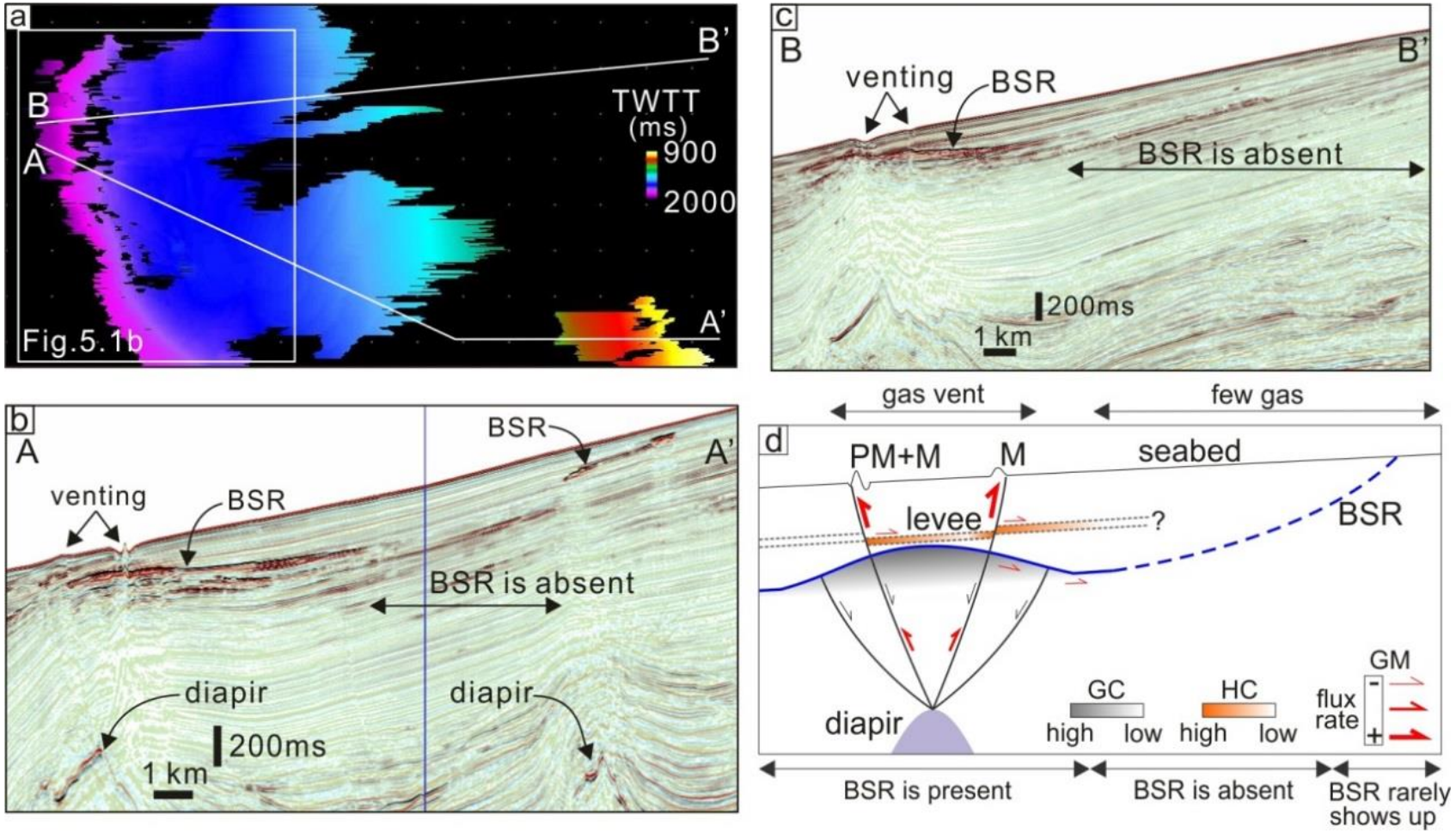

Fig.5.6 (a) The BSR depth measured in two-way travel time (TWTT). No-data places (black colour) indicate where the BSR cannot be observed in the seismic cross section. (b, c) Two representative seismic sections showing that BSR can be tracked above the studied diapir, but is absent elsewhere except the region to the southeast of it. (d) Schematic diagram showing gas migration and where the BSR is present. Black arrows mark the displacement direction of the hanging wall. The dimension of the diapir and the levee is not to scale. PM – pockmark, M – mound, GC – gas concentration, HC – hydrate concentration, GM – gas migration.

Chapter 6 Discussion and Conclusions

6.1 Uncertainties

6.1.1 Seismic resolution and interpretation

The vertical resolution of seismic data is commonly defined as one quarter of the wavelength and it is uncertain in this research because there are no direct measurements of P-wave velocity. The P-wave velocity in subsurface sediment is assumed to be 1800 m/s, but it could be 1600 to 2000 m/s at <400 mbsf (Hustoft et al., 2009; Rajan et al., 2012). This causes an error of ± 1 m in the vertical resolution, which is encountered in determining the height of the gas column in chapter 3 and the total thickness of the hydrate-bearing sediments in chapter 4.

The uncertainties caused by solely using the seismic attribute of amplitude cannot be eliminated but can be reduced by using appropriate rock physics tools (Avseth et al., 2010). The seismic response of hydrate-bearing sediments could be either enhanced reflections (Hornbach et al., 2003) or amplitude blanking (Lee et al., 1993). This uncertain seismic response may cause difficulty in interpreting hydrate deposits. Here the 1-D synthetic seismogram is used to discuss under what circumstances these responses will appear. The results (appendix 3) show how a seismic waveform varies in response to hydrate-bearing sediments at different saturations in the models of (a) an isolated hydrate in the HSZ and (b) hydrate-bearing sediments underlain by free gas at the BSR (Fig.A3.1). For the model a, amplitude does not necessarily increase with hydrate concentration. When the porosities of the hydrate reservoir and the clay are similar (e.g. 30% and 20%, Fig. A3.2), the amplitude responding to the interface between them increases with hydrate concentration. When the hydrate concentration is 30% and the difference of these porosities is 20% (Fig. A3.3), there is an apparent amplitude decrease at the interface. This suggests that either amplitude blanking or enhanced reflectance can indicate the occurrence of an isolated hydrate deposit. In addition, the absolute values of amplitude at the BSR are larger than those at the clay-hydrate interface (Fig. A3.4), even if the hydrate concentration reaches 90%. This supports the interpretation of the hydrate deposits in chapter 4 and 5.

6.1.2 Resetting of the BHSZ

When the BHSZ resets, driven by changes in ambient conditions, the magnitude of the shoaling or deepening distance has a range and could vary at different sites. An example is shown here (Fig. 6.1) to show the different resetting distances along the BHSZ in cross section. A 2-D steady-state heat conduction model is used to estimate how much BHSZ should have shoaled since the LGM. The governing equation and its solution are stated in section 5.7.1. Input parameters, including the estimated present ocean temperature at this location and the variation of the BWT and RSL are identical with those in chapter 4. The results (Fig. 6.1) suggest that the vertical distance between the present-day BHSZ and the BHSZ during the LGM decreases as the water depth reduces. In the 2-D heat diffusion model the BHSZ shoals by ~60 m (appendix 2) and this distance is larger than that estimated using the 2-D conduction method here (39.1 m, the site is marked in dashed line in Fig. 6.1). The reason for the differences between modelling results derives from the assumption of whether the thermal regime is at steady state. Therefore, to compare resetting distance of the BHSZ between marine hydrate systems around the world under the same circumstances, the modelling method and the site at which this resetting occurs should be stated.

6.1.3 Parameters in modelling

The reliability of modelling outcome depends on to what degree the input parameters are constrained (Harbaugh et al., 2001) and the method. In this research subsurface sediments are assumed to be homogeneous and isotropic and this simplification fails to reveal complex information, though it can accelerate computing of numerical models. An example is the thermal conductivity in the models of 2-D heat conduction, which is assumed to be the same along the horizontal (x) and vertical (z) directions. But in reality heat conduction in clastic sediment is anisotropic such that $k_x \neq k_z$ (Ozisik, 1993). Secondly, some parameters, such as BWT which in part controls the depth of the BHSZ, are not well constrained. Better constraining the BWT requires analysis of isotopic records and is out of scope of this research.

There are no direct measurements of past BWTs and therefore they are uncertain (Pekar et al., 2002; Waelbroeck et al., 2002). Quantitatively assessing the impact of these uncertainties for the modelling results is difficult solely by geophysical means. Another input parameter that has uncertainty is the methane density. In chapter 3 the density of methane trapped below hydrates is estimated under the assumption of being ideal gas, but actually it may be not. Peng-Robison equation of state (EOS) is used to get the methane density and compare to that calculated using Clapeyron equation. The results show that the density of ideal gas (100% methane) is ~28% smaller (Fig. 6.2). The methane density is estimated to be 114 kg/m^{-3} at the pressure of 13.1 MPa, the temperature of 13 ^{o}C using Peng-Robison EOS. The proposed mechanism that submarine failure can be primed is not affected after using this methane density but the critical height of gas column would be 236 m instead of 231 m.

6.2 Discussion: responses of hydrates to changes in ambient conditions and fate of released gas

The fundamental questions that this research attempts to answer are how methane in the marine hydrate system migrates towards the seabed or is retained in the subsurface and how marine hydrates along the continental margins behave during periods of ocean warming such as since the LGM. The answers to these questions are important in assessing a series of proposed consequences caused by methane release, including ocean deoxygenation and acidification (Biastoch et al., 2011; Yamamoto et al., 2014) and, which is controversial, the climatic warming (Kvenvolden, 1993; Kennett et al., 2000; Maslin et al., 2004; Myhre et al., 2016). Potential scenarios for the fate of gases in the shallow (< 150 mbsf) and deep sections (≥ 150 mbsf) of the feather edge of marine hydrates are discussed to comprehensively show the dynamics of marine hydrates in the passive continental margin setting (Fig. 6.3). The depth of 150 mbsf is determined arbitrarily to be the boundary between the deep and shallow section because at places greater than this depth hydrates are relatively stable at a timescale of 100 yrs.

In general there could be marine hydrates in the shallow section due to the feeding of methane carried by upward fluid advection, though methane is normally oxidised anaerobically by sulphate-consuming bacteria within the sediments that are < 70 mbsf (Borowski et al., 1999; Ussler and Paull, 2008). Some photos taken by remotely operated vehicles at the seabed show that gas hydrates occasionally occur at the seabed (e.g. Marcon et al., 2014). In the shallow section of the study area few BSRs are observed in the seismic data. This could be explained by that there are hydrates of low concentration underlain by few free gases, the configuration of which could not produce detectable acoustic impedance contrast at the phase boundary (Mackay et al., 1994; Davies et al., 2015). The small-scale presence of hydrates is also supported by the potential outcropping gas hydrates imaged by the seismic data and these hydrates are located at the irregular intersection between the BSR and the seabed (Fig. 6.3, Davies et al., 2015). Marine hydrates in the shallow section are more susceptible to variations in ocean temperature. Widespread methane release from the seabed, which is evidenced by gas plumes combined with numerical models, has been documented, driven by the fluctuation of ocean temperature at the timescales of one year (Berndt et al., 2014) and four decades (Westbrook et al., 2009; Hautala et al., 2014). On the contrary, marine hydrates in the shallow section of the study area may not release significant amounts of methane. The magnitude of the temperature change offshore of Mauritania from 2009 to 2013 is < 1 ^{o}C (data from WOD). It results in that less marine hydrates dissociated offshore Mauritania than those offshore West Spitsbergen (Westbrook et al., 2009) and therefore less methane was released from the seabed offshore of Mauritania after 2009. The seismic datasets show little evidence for hydrate dissociation and methane release from the shallow section but this could be revealed by other data such as P-wave velocity (c.f. Sarkar et al., 2012) and sonar images (c.f. Westbrook et al., 2009).

Gas hydrates in the deep section are more stable due to the relatively thick thermal buffer of the overlying sediments in the HSZ (Archer et al., 2009). In the previous chapters methane hydrate deposits are interpreted to be located at the base and in the HSZ, but not near the seabed (Fig. 6.3). The formation of gas hydrates in the HSZ is often the result of advection of methane (Pecher, 2002), which is supported by seismic features of vertical gas migration conduits including faults and gas chimneys. The responses of gas hydrates at these sites have a

longer delay due to heat conduction and can only respond to long-term (> 100 yrs) temperature changes. Relative sea-level change is another factor that can extensively control the stability of marine hydrates via affecting pore-fluid pressure (e.g. Crémière et al., 2016). In general the depth of the BHSZ primarily depends on temperature and to a lesser extent on pressure (Hornbach et al., 2008). For instance at the Blake Ridge, a 1 ^{o}C change in the geothermal gradient and a 100 m change in the seafloor depth shift the depth of the BHSZ by ~15 m and ~5 m, respectively (water depth of 2800 m, seafloor temperature of 3.4 ^{o}C and thermal gradient of 34.3 ^{o}C/km, Sloan Jr and Koh, 2007; Hornbach et al., 2008). Therefore, marine hydrates along the continental margin are more sensitive to ocean warming than sea-level rise over short term (<1000 yrs) in the past. Once methane has been liberated from hydrates, it will not immediately migrate through the effective barrier of the sub-seabed sediments. Instead, part of methane is recycled when reaching the newly formed HSZ (Brown et al., 1996; Davies and Clarke, 2010). Some other methane arriving at the BHSZ subsequently will be trapped below hydrate-bearing sediments (Davies and Clarke, 2010; Minshull et al., 2016). There are some ways that gases can bypass the impermeable sediment to reach the seabed: (a) accumulating gas below hydrates can reduce the strength of the overlying sediments to the level that submarine failures could happen (McIver, 1982; Li et al., 2016) then vast quantities of trapped gases will be released into the ocean (McIver, 1982; Paull et al., 2002; Talling et al., 2014). It is proposed that multiple failures could occur and this process may repeat itself before gas arriving at the seabed (Berndt et al., 2012). (b) Critically pressured gas accumulation below hydrates could result in the formation of vertical fractures (Davies and Clarke, 2010) and faults (Hornbach et al., 2004). Gases are charged into and discharged from the sediments through these conduits at intervals, which allows for episodic gas venting (Paull et al., 1995; Gorman et al., 2002; Crutchley et al., 2013). The seismic datasets show that there are no submarine failures extending from the BHSZ to the seabed and limited-scale substantial vents. Therefore, although some hydrates in the deep section may be subject to the delayed thermal effect and probably dissociate recently, the responses of hydrate to ambient conditions are slow and, more importantly, most of released gases are retained in the subsurface. Even if gas could enter the ocean, most of it will be oxidised during its ascent in the water column (McGinnis et al., 2006; Graves et al., 2015). Only a small proportion of it could enter the atmosphere via catastrophic released of gas bubbles coated by hydrates (McGinnis et al., 2006; Smith et al., 2014).

6.3 Future work

Offshore of Mauritania is an underexplored region for marine hydrate and there are new findings made in this research, but some fundamental questions with regard to marine hydrate system are unanswered. For instance how much of methane released from hydrates can enter the ocean and what is the proportion of this methane is retained in subsurface. Future work is needed to continue elucidating the fate of methane released from and captured in marine hydrate system offshore of Mauritania.

An upward shift of the BHSZ due to oceanic warming after the LGM is proposed, but the evidence for the link to the LGM has uncertainties. Compelling evidence is needed to corroborate the response of marine hydrate to temperature variation in the past. This response has been researched around the world at the time scale of one year (Berndt et al., 2014) and decades (Hautala et al., 2014) and during particular warming episodes, such as the Paleocene-Eocene Thermal Maximum (PETM, Minshull et al., 2016) and the Early and Late Jurassic (Hesselbo et al., 2000; Padden et al., 2001), but is still unclear in offshore of Mauritania. In the last 8 years the fate of methane in the feather edge offshore of Mauritania can be examined by taking the records of BWT in the World Ocean Database (WOD) as input parameters into the numerical models. The results could allow for an estimation of the amount of released methane and make the study area be a good example of short-term methane release at low-latitude regions. In addition, offshore of Mauritania is an upwelling region and future work may provide new insight into the flux rate of released methane in the context of deep ocean upwelling. To better constrain the amount of released methane, the thickness and saturation of the hydrate reservoir needs to be determined using seismic inversion and data from drilling (e.g. cores) with proper rock physical tools.

Gas released by hydrate dissociation could cause submarine failures, ocean acidification and deoxygenation. This gas would rise due to its buoyancy and attempt to reach a free surface by either priming overlying sediment until failures happen (chapter 3) or bypassing the HSZ

through gas chimneys (chapter 4) or along faults (chapter 5). After methane leaves the seabed, how much of it will dissolve into the ocean and under what circumstances it can reach the atmosphere or alternatively be recycled or oxidised are important in understanding its fate. Answering these questions goes beyond the scope of this research but progress could be made if any gas plume was found to sit right above a venting site in offshore of Mauritania. This could be of help in knowing how much methane could enter the shallow waters and thus assessing its impact.

6.4 Conclusions

Examining two exceptional-quality 3-D seismic surveys provides new insight into marine hydrate system and gas migration in the subsurface offshore of Mauritania. The BSR, which is an important tool to show the interface between hydrate-bearing and gas-charged sediments, is identified on the basis of reflectance enhancement, reversed polarity and cross-cutting stratal reflections. Linear high-amplitude features of different orientations at the level of the BSR are found in both of the seismic surveys and termed 'bands'. Their presence indicates the widespread presence of free gases trapped stratigraphically below hydrates.

Hydrate dissociation is thought to be a possible trigger for submarine failures (e.g. Storegga Slide offshore Norway, Sultan et al., 2004), as predicted by McIver (1982). His hypothesis related to submarine failures includes another idea that buoyancy provided by gases underlying hydrates could cause failures, which for the first time is supported by the seismic evidence in this research. A seismically-imaged shear zone sits immediately above the BSR. Buoyancy built up by the capped gas accumulation is calculated. It could prime the overlying sediment for the incipient submarine failure, though it is uncertain to what degree gas-filled pores within this gas accumulation are inter-connected.

The feather edge is an important site for warming-induced methane release into the ocean (Westbrook et al., 2009; Phrampus and Hornbach, 2012). In this research a venting

system was investigated and its existence is manifested by a series of pockmarks and mounds aligning along permeable faults. Their spatial relationship together with acoustic wipe-out indicates that gas-rich pore fluid bypasses the HSZ. The BHSZ at the feather edge is not marked by a BSR everywhere. The BSR is absent because gases were vented rather than migrating landwards along the BHSZ. Therefore, warming-induced methane release could not necessarily take place at the landward limit of the feather edge in the study area.

Methane can be recycled as hydrates after being liberated from them. New evidence involving some hydrate deposits fed by 15 gas chimneys indicates recycling could have occurred. These hydrates are interpreted to form due to the thinning of the HSZ after the LGM. This process implies that not all methane released from marine hydrates will necessarily enter the ocean. Therefore, the contribution of marine hydrate to the atmospheric methane budget could be less than that estimated before. Future work could focus on the amount of methane transfer from the lithosphere to the hydrosphere at a given time scale and quantitatively assess the implication of methane released from marine hydrate.

6.5 Figures

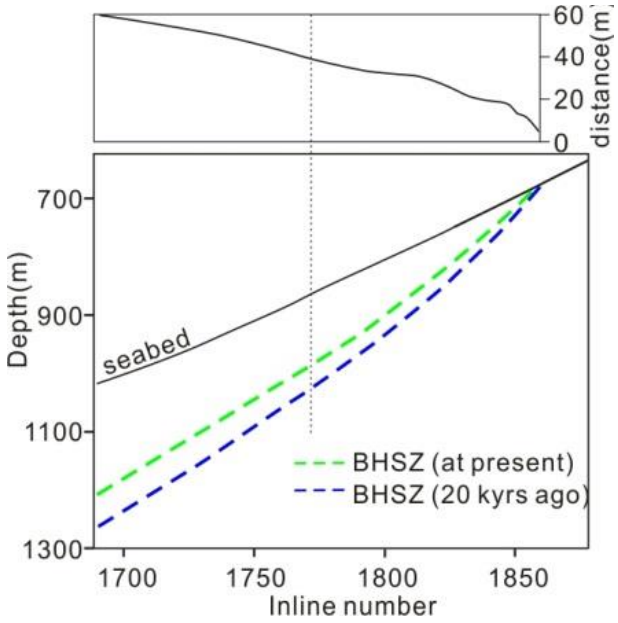

Fig.6.1 The 2-D heat conduction modelling results of the BHSZ at present and the LGM. The upper figure shows the distance between the two modelled BHSZs. The vertical dashed line marks the position where 2-D heat diffusion model is adopted in chapter 4.

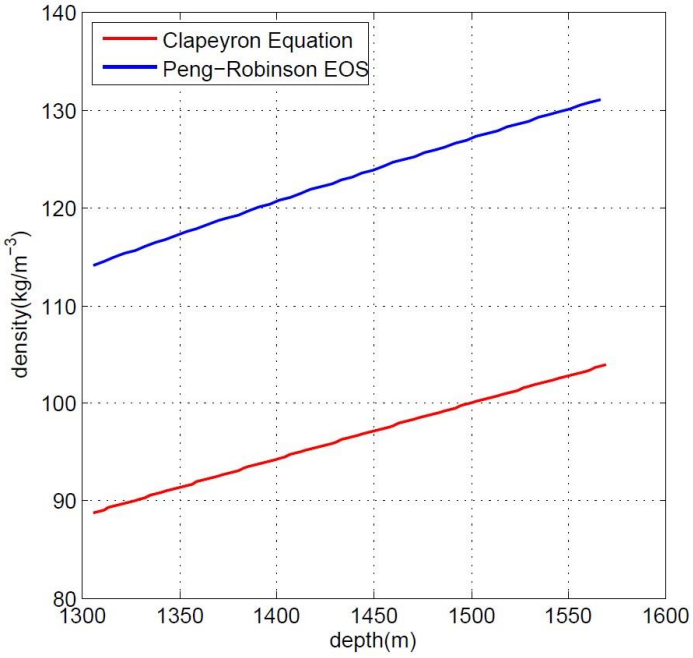

Fig.6.2 Methane densities at different depths. They are calculated using Clapeyron equation and Peng-Robinson equation of state.

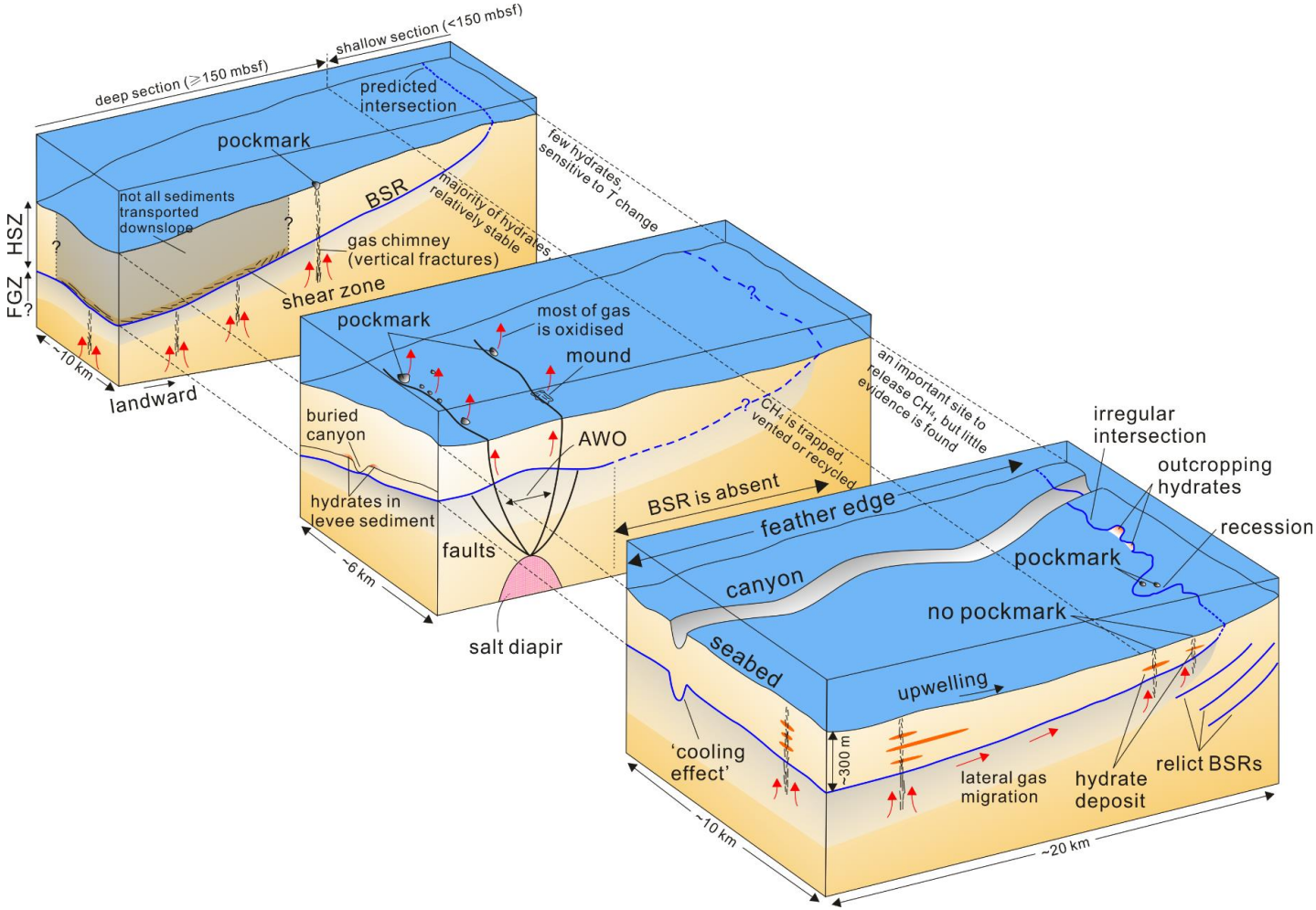

Fig. 6.3 Generic diagram showing the marine hydrate system offshore of Mauritania (not to scale). The upper section is a model for the mechanism proposed in chapter 3. A shear zone is observed along the base of hydrate-filled sediment. The underlying gas could reduce the shear strength of the hydrate-filled sediment and prime the submarine failures. Excess pore pressure could be preserved, which is supported by that no gas chimneys breach the BSR sealing in the shear zone. The middle section shows the venting system stated in chapter 5. Gas migrated along the diapirism-driven fault, bypassed the HSZ and entered the ocean, leaving the mounds and pockmarks at the seabed. Due to this vent, lateral gas migration is intercepted and the BSR cannot be observed landward of the venting system. The lower section summarises the interpretations in chapter 4 and others that are not stated in previous chapters. Methane is recycled as gas hydrate after entering the HSZ. The canyon affects the location of the BHSZ and allows gas to migrate laterally along the canyon wall. The intersection of the BHSZ and the seabed is irregular and along it pockmarks and outcropping hydrates can be found.

References

Abrams, M.A., 1992. Geophysical and geochemical evidence for subsurface hydrocarbon leakage in the Bering Sea, Alaska. *Marine and Petroleum Geology* 9(2), 208-221.

Anderson, A.L., Hampton, L.D., 1980. Acoustics of gas-bearing sediments I. Background. *The Journal of the Acoustical Society of America* 67(6), 1865-1889.

Andreassen, K., Hart, P.E., MacKay, M., 1997. Amplitude versus offset modeling of the bottom simulating reflection associated with submarine gas hydrates. *Marine Geology* 137(1-2), 25-40.

Andreassen, K., Mienert, J., Bryn, P., Singh, S.C., 2000. A double gas-hydrate related bottom simulating reflector at the Norwegian continental margin. *Annals of the New York Academy of Sciences* 912(1), 126-135.

Andresen, K.J., Huuse, M., Schodt, N.H., Clausen, L.F., Seidler, L., 2011. Hydrocarbon plumbing systems of salt minibasins offshore Angola revealed by three-dimensional seismic analysis. *AAPG bulletin* 95(6), 1039-1065.

Antobreh, A.A., Krastel, S., 2006. Morphology, seismic characteristics and development of Cap Timiris Canyon, offshore Mauritania: a newly discovered canyon preserved-off a major arid climatic region. *Marine and Petroleum Geology* 23(1), 37-59.

Antobreh, A.A., Krastel, S., 2007. Mauritania Slide Complex: morphology, seismic characterisation and processes of formation. *International Journal of Earth Sciences* 96(3), 451-472.

Archer, D., Buffett, B., Brovkin, V., 2009. Ocean methane hydrates as a slow tipping point in the global carbon cycle. *Proceedings of the National Academy of Sciences* 106(49), 20596-20601.

Avseth, P., Mukerji, T., Mavko, G., 2010. Quantitative seismic interpretation: Applying rock physics tools to reduce interpretation risk. Cambridge university press, 168.

Bacon, M., Simm, R., Redshaw, T., 2007. 3-D seismic interpretation. Cambridge University Press, 18-55.

Bangs, N.L., Musgrave, R.J., Tréhu, A.M., 2005. Upward shifts in the southern Hydrate Ridge gas hydrate stability zone following postglacial warming, offshore Oregon. *Journal of Geophysical Research: Solid Earth* 110, B03102, doi:10.1029/2004JB003293.

Beaudoin, Y.C., Dallimore, S.R., Boswell, R., 2014. Frozen heat: A UNEP global outlook on methane gas hydrates. *United Nations Environment Programme, GRID-Arendal*, 29.

Berndt, C., Feseker, T., Treude, T., Krastel, S., Liebetrau, V., Niemann, H., Bertics, V.J., Dumke, I., Dünnbier, K., Ferré, B., 2014. Temporal constraints on hydrate-controlled methane seepage off Svalbard. *Science* 343(6168), 284-287.

Berndt, C., Costa, S., Canals, M., Camerlenghi, A., de Mol, B., Saunders, M., 2012. Repeated slope failure linked to fluid migration: The Ana submarine landslide complex, Eivissa Channel, Western Mediterranean Sea. *Earth and Planetary Science Letters* 319, 65-74.

Berndt, C., Mienert, J., Vanneste, M., Bünz, S., Bryn, P., 2002. Submarine slope-failure offshore Norway triggers rapid gas hydrate decomposition, Proceedings of the Fourth International Conference on Gas Hydrates, Yokohama, Japan, 19-23, May, 71-74.

Biastoch, A., Treude, T., Rüpke, L.H., Riebesell, U., Roth, C., Burwicz, E.B., Park, W., Latif, M., Böning, C.W., Madec, G., 2011. Rising Arctic Ocean temperatures cause gas hydrate destabilization and ocean acidification. *Geophysical Research Letters* 38, L08602, doi:10.1029/2011GL047222.

Bintanja, R., Van de Wal, R., 2008. North American ice-sheet dynamics and the onset of 100,000-year glacial cycles. *Nature* 454(7206), 869-872.

Boait, F., White, N., Bickle, M., Chadwick, R., Neufeld, J., Huppert, H., 2012. Spatial and temporal evolution of injected CO2 at the Sleipner Field, North Sea. *Journal of Geophysical Research: Solid Earth* 117, B03309, doi:10.1029/2011JB008603.

Booth, J.S., Winters, W.J., Dillon, W.P., 1994. Circumstantial Evidence of Gas Hydrate and Slope Failure Associations on the United-States Atlantic Continental-Margin. *Annals of the New York Academy of Sciences* 715(1), 487-489.

Borowski, W.S., Paull, C.K., Ussler, W., 1999. Global and local variations of interstitial sulfate gradients in deep-water, continental margin sediments: Sensitivity to underlying methane and gas hydrates. *Marine Geology* 159(1), 131-154.

Boswell, R., 2009. Is gas hydrate energy within reach? *Science* 325(5943), 957-958.

Boswell, R., Collett, T.S., 2011. Current perspectives on gas hydrate resources. *Energy & Environmental Science* 4(4), 1206-1215.

Brooks, J., Kennicutt, M., Fay, R., McDonald, T., Sassen, R., 1984. Thermogenic gas hydrates in the Gulf of Mexico. *Science* 225(4660), 409-411.

Brown, A., 2010, Interpretation of Three-dimensional Seismic Data, seventh ed., AAPG and EGP, Tulsa, 31-60, 275-281.

Brown, H.E., Holbrook, W.S., Hornbach, M.J., Nealon, J., 2006. Slide structure and role of gas hydrate at the northern boundary of the Storegga Slide, offshore Norway. *Marine Geology* 229(3), 179-186.

Brown, K.M., Bangs, N.L., Froelich, P.N., Kvenvolden, K.A., 1996. The nature, distribution, and origin of gas hydrate in the Chile Triple Junction region. *Earth and Planetary Science Letters* 139(3-4), 471-483.

Bull, S., Cartwright, J., Huuse, M., 2009a. A review of kinematic indicators from mass-transport complexes using 3D seismic data. *Marine and Petroleum Geology* 26(7), 1132-1151.

Bull, S., Cartwright, J., Huuse, M., 2009b. A subsurface evacuation model for submarine slope failure. *Basin Research* 21(4), 433-443.

Bünz, S., Mienert, J., 2004. Acoustic imaging of gas hydrate and free gas at the Storegga Slide. *Journal of Geophysical Research: Solid Earth* 109, B04102, doi:10.1029/2003JB002863.

Bünz, S., Mienert, J., Bryn, P., Berg, K., 2005. Fluid flow impact on slope failure from 3D seismic data: a case study in the Storegga Slide. *Basin Research* 17(1), 109-122.

Bünz, S., Polyanov, S., Vadakkepuliyambatta, S., Consolaro, C., Mienert, J., 2012. Active gas venting through hydrate-bearing sediments on the Vestnesa Ridge, offshore W-Svalbard. *Marine Geology* 332, 189-197.

Carcione, J.M., Tinivella, U., 2000. Bottom-simulating reflectors: Seismic velocities and AVO effects. *Geophysics* 65(1), 54-67, doi:10.1190/1.1444725.

Cartwright, J., 2007. The impact of 3D seismic data on the understanding of compaction, fluid flow and diagenesis in sedimentary basins. *Journal of the Geological Society* 164(5), 881-893.

Cartwright, J., Huuse, M., Aplin, A., 2007. Seal bypass systems. *AAPG Bulletin* 91(8), 1141-1166.

Cartwright, J., Santamarina, C., 2015. Seismic characteristics of fluid escape pipes in sedimentary basins: Implications for pipe genesis. *Marine and Petroleum Geology* 65, 126-140.

Cathles, L.M., Su, Z., Chen, D., 2010. The physics of gas chimney and pockmark formation, with implications for assessment of seafloor hazards and gas sequestration. *Marine and Petroleum Geology* 27(1), 82-91.

Catterall, V., Redfern, J., Gawthorpe, R., Hansen, D., Thomas, M., 2010. Architectural style and quantification of a submarine channel–levee system located in a structurally complex area: offshore Nile Delta. *Journal of Sedimentary Research* 80(11), 991-1017.

Chabert, A., Minshull, T.A., Westbrook, G.K., Berndt, C., Thatcher, K.E., Sarkar, S., 2011. Characterization of a stratigraphically constrained gas hydrate system along the western continental margin of Svalbard from ocean bottom seismometer data. *Journal of Geophysical Research: Solid Earth* 116, B12102, doi:10.1029/2011JB008211.

Chappellaz, J.A., Fung, I.Y., Thompson, A.M., 1993. The atmospheric CH_4 increase since the Last Glacial Maximum. *Tellus B* 45, 228-241, doi:10.1034/j.1600-0889.1993.t01-2-00002.x.

Clennell, M.B., Hovland, M., Booth, J.S., Henry, P., Winters, W.J., 1999. Formation of natural gas hydrates in marine sediments: 1. Conceptual model of gas hydrate growth conditioned by host sediment properties. *Journal of Geophysical Research: Solid Earth* 104*(*B10*)*, 22985–23003, doi:10.1029/1999JB900175.

Collett, T., 1999. Detailed evaluation of gas hydrate reservoir properties using JAPEX/JNOC/GSC Mallik 2L-38 gas hydrate research well downhole well-log displays. *Bulletin of the Geological Survey of Canada*, 295-311.

Collett, T.S., 2001. A review of well-log analysis techniques used to assess gas-hydrate-bearing reservoirs. *Natural gas hydrates: occurrence, distribution, and detection*, 189-210.

Collett, T.S., 2002. Energy resource potential of natural gas hydrates. *AAPG Bulletin* 86(11), 1971-1992.

Collett, T.S., 2008. Assessment of gas hydrate resources on the North Slope, Alaska, 2008. *AGU Fall Meeting Abstracts*, 2008AGUFMOS43F..08C.

Collett, T.S., Wendlandt, R.F., 2000. Formation evaluation of gas hydrate-bearing marine sediments on the Blake Ridge with downhole geochemical log measurements, *Proceedings of the Ocean Drilling Program, Scientific Results* 164, 199-215.

Crémière, A., Lepland, A., Chand, S., Sahy, D., Condon, D.J., Noble, S.R., Martma, T., Thorsnes, T., Sauer, S., Brunstad, H., 2016. Timescales of methane seepage on the Norwegian margin following collapse of the Scandinavian Ice Sheet. *Nature communications* 7.

Crutchley, G.J., Berndt, C., Geiger, S., Klaeschen, D., Papenberg, C., Klaucke, I., Hornbach, M.J., Bangs, N.L., Maier, C., 2013. Drivers of focused fluid flow and methane seepage at south Hydrate Ridge, offshore Oregon, USA. *Geology* 41(5), 551-554.

Crutchley, G.J., Klaeschen, D., Planert, L., Bialas, J., Berndt, C., Papenberg, C., Hensen, C., Hornbach, M., Krastel, S., Brückmann, W., 2014. The impact of fluid advection on gas hydrate stability: Investigations at sites of methane seepage offshore Costa Rica. *Earth and Planetary Science Letters* 401, 95-109.

Davie, M.K., Buffett, B.A., 2003. Sources of methane for marine gas hydrate: inferences from a comparison of observations and numerical models. *Earth and Planetary Science Letters* 206(1), 51-63.

Davies, R.J., Clarke, A.L., 2010. Methane recycling between hydrate and critically pressured stratigraphic traps, offshore Mauritania. *Geology* 38(11), 963-966.

Davies, R.J., Thatcher, K.E., Armstrong, H., Yang, J., Hunter, S., 2012a. Tracking the relict bases of marine methane hydrates using their intersections with stratigraphic reflections. *Geology* 40(11), 1011-1014.

Davies, R.J., Thatcher, K.E., Mathias, S.A., Yang, J., 2012b. Deepwater canyons: An escape route for methane sealed by methane hydrate. *Earth and Planetary Science Letters* 323, 72-78.

Davies, R.J., Yang, J., Hobbs, R., Li, A., 2014. Probable patterns of gas flow and hydrate accretion at the base of the hydrate stability zone. *Geology* 42(12), 1055-1058.

Davies, R.J., Yang, J., Li, A., Mathias, S., Hobbs, R., 2015. An irregular feather-edge and potential outcrop of marine gas hydrate along the Mauritanian margin. *Earth and Planetary Science Letters* 423, 202-209.

Dickens, G.R., 2003. Rethinking the global carbon cycle with a large, dynamic and microbially mediated gas hydrate capacitor. *Earth and Planetary Science Letters* 213(3), 169-183.

Dickens, G.R., Paull, C.K., Wallace, P., 1997. Direct measurement of in situ methane quantities in a large gas-hydrate reservoir. *Nature* 385, 426-428.

Dillon, W.P., Nealon, J.W., Taylor, M.H., Lee, M.W., Drury, R.M., Anton, C.H., 2001. Seafloor collapse and methane venting associated with gas hydrate on the blake ridge: causes and implications to seafloor stability and methanerelease. *Natural gas hydrates: occurrence, distribution, and detection*, 211-233.

Dimitrov, L.I., 2002. Mud volcanoes – the most important pathway for degassing deeply buried sediments. *Earth-Science Reviews* 59(1), 49-76.

Egorov, A.V., Rozhkov, A.N., 2010. Formation of gas hydrate reservoirs in submarine mud volcanos. *Fluid Dynamics* 45(5), 769-778.

Flemings, P.B., Liu, X.L., Winters, W.J., 2003. Critical pressure and multiphase flow in Blake Ridge gas hydrates. *Geology* 31(12), 1057-1060.

Ford, K., Naehr, T., Skilbeck, G., 2003. The use of infrared thermal imaging to identify gas hydrate in sediment cores, *Proceedings of the Ocean Drilling Program, Scientific results. Ocean Drilling Program*, Texas A&M University, initial reports volume 201.

Foucher, J.P., Nouzé, H., Henry, P., 2002. Observation and tentative interpretation of a double BSR on the Nankai slope. *Marine Geology* 187(1), 161-175.

Gay, A., Lopez, M., Cochonat, P., Seranne, M., Levache, D., Sermondadaz, G., 2006. Isolated seafloor pockmarks linked to BSRs, fluid chimneys, polygonal faults and stacked Oligocene-Miocene turbiditic palaeochannels in the Lower Congo Basin. *Marine Geology* 226(1), 25-40.

Ginsburg, G., Soloviev, V., Cranston, R., Lorenson, T., Kvenvolden, K., 1993. Gas hydrates from the continental slope, offshore Sakhalin Island, Okhotsk Sea. *Geo-Marine Letters* 13(1), 41-48.

Golmshtok, A.Y., Soloviev, V.A., 2006. Some remarks on the thermal nature of the double BSR. *Marine Geology* 229(3), 187-198.

Gorman, A.R., Holbrook, W.S., Hornbach, M.J., Hackwith, K.L., Lizarralde, D., Pecher, I., 2002. Migration of methane gas through the hydrate stability zone in a low-flux hydrate province. *Geology* 30(4), 327-330.

Gornitz, V., Fung, I., 1994. Potential distribution of methane hydrates in the world's oceans. *Global Biogeochemical Cycles* 8(3), 335-347.

Graves, C.A., Steinle, L., Rehder, G., Niemann, H., Connelly, D.P., Lowry, D., Fisher, R.E., Stott, A.W., Sahling, H., James, R.H., 2015. Fluxes and fate of dissolved methane released at the seafloor at the landward limit of the gas hydrate stability zone offshore western Svalbard. *Journal of Geophysical Research: Oceans* 120, 6185-6201, doi:10.1002/2015JC011084.

Haacke, R.R., Westbrook, G.K., Hyndman, R.D., 2007. Gas hydrate, fluid flow and free gas: Formation of the bottom-simulating reflector. *Earth and Planetary Science Letters* 261(3), 407-420.

Harbaugh, J.W., Merriam, D.F., Davis, J.C., 2001. Geologic modeling and simulation: sedimentary systems. Springer Science & Business Media, 135.

Harvey, L., Huang, Z., 1995. Evaluation of the potential impact of methane clathrate destabilization on future global warming. *Journal of Geophysical Research: Atmospheres* 100*(*D2*)*, 2905-2926, doi:10.1029/94JD02829.

Hautala, S.L., Solomon, E.A., Johnson, H.P., Harris, R.N., Miller, U.K., 2014. Dissociation of Cascadia margin gas hydrates in response to contemporary ocean warming. *Geophysical Research Letters* 41, 8486-8494, doi:10.1002/2014GL061606.

Helgerud, M., Waite, W.F., Kirby, S., Nur, A., 2009. Elastic wave speeds and moduli in polycrystalline ice Ih, sI methane hydrate, and sII methane-ethane hydrate. *Journal of Geophysical Research: Solid Earth* 114, *B02212,* doi:10.1029/2008JB006132.

Henrich, R., Cherubini, Y., Meggers, H., 2010. Climate and sea level induced turbidite activity in a canyon system offshore the hyperarid Western Sahara (Mauritania): The Timiris Canyon. *Marine Geology* 275(1), 178-198.

Henrich, R., Hanebuth, T.J.J., Krastel, S., Neubert, N., Wynn, R.B., 2008. Architecture and sediment dynamics of the Mauritania Slide Complex. *Marine and Petroleum Geology* 25(1), 17-33.

Hesse, R., Harrison, W.E., 1981. Gas hydrates (clathrates) causing pore-water freshening and oxygen isotope fractionation in deep-water sedimentary sections of terrigenous continental margins. *Earth and Planetary Science Letters* 55(3), 453-462.

Hesselbo, S.P., Gröcke, D.R., Jenkyns, H.C., Bjerrum, C.J., Farrimond, P., Bell, H.S.M., Green, O.R., 2000. Massive dissociation of gas hydrate during a Jurassic oceanic anoxic event. *Nature* 406(6794), 392-395.

Ho, S., Cartwright, J.A., Imbert, P., 2012. Vertical evolution of fluid venting structures in relation to gas flux, in the Neogene-Quaternary of the Lower Congo Basin, Offshore Angola. *Marine Geology* 332, 40-55.

Hoehler, T.M., Borowski, W.S., Alperin, M.J., Rodriguez, N.M., Paull, C.K., 2000. Model, stable isotope, and radiotracer characterization of anaerobic methane oxidation in gas hydrate-bearing sediments of the Blake Ridge, *Proceedings of the Ocean Drilling Program, Scientific Results*. Ocean Drilling Program College Station, TX, 79-85.

Hornbach, M.J., Holbrook, W.S., Gorman, A.R., Hackwith, K.L., Lizarralde, D., Pecher, I., 2003. Direct seismic detection of methane hydrate on the Blake Ridge. *Geophysics* 68(1), 92-100, doi: 10.1190/1.1543196

Hornbach, M.J., Ruppel, C., Saffer, D.M., Van Dover, C.L., Holbrook, W.S., 2005. Coupled geophysical constraints on heat flow and fluid flux at a salt diapir. *Geophysical Research Letters* 32, *L24617,* doi:10.1029/2005GL024862.

Hornbach, M.J., Saffer, D.M., Holbrook, W.S., 2004. Critically pressured free-gas reservoirs below gas-hydrate provinces. *Nature* 427(6970), 142-144.

Hornbach, M.J., Saffer, D.M., Holbrook, W.S., Van Avendonk, H.J., Gorman, A.R., 2008. Three-dimensional seismic imaging of the Blake Ridge methane hydrate province: Evidence for large, concentrated zones of gas hydrate and morphologically driven advection. *Journal of Geophysical Research: Solid Earth* 113, B07101, doi:10.1029/2007JB005392.

Horozal, S., Bahk, J.J., Urgeles, R., Kim, G.Y., Cukur, D., Kim, S.P., Lee, G.H., Lee, S.H., Ryu, B.J., Kim, J.H., 2017. Mapping gas hydrate and fluid flow indicators and modeling gas

hydrate stability zone (GHSZ) in the Ulleung Basin, East (Japan) Sea: Potential linkage between the occurrence of mass failures and gas hydrate dissociation. *Marine and Petroleum Geology* 80, 171-191.

Houghton, J.T., Callander, B.A., Varney, S.K., 1992. The supplementary report to the IPCC scientific assessment. *Intergovernmental Panel on Cllmate Change, Cambrldge Univ Press, Cambridge*, 29.

Hovland, M., Judd, A., 1988. Seabed pockmarks and seepages: impact on geology, biology, and the marine environment. Springer, 119-131.

Hovland, M., Svensen, H., 2006. Submarine pingoes: Indicators of shallow gas hydrates in a pockmark at Nyegga, Norwegian Sea. *Marine Geology* 228(1), 15-23.

Hovland, M., Talbot, M.R., Qvale, H., Olaussen, S., Aasberg, L., 1987. Methane-related carbonate cements in pockmarks of the North Sea. *Journal of Sedimentary Research* 57(5), 881-892.

Hunter, S.J., Goldobin, D.S., Haywood, A.M., Ridgwell, A., Rees, J.G., 2013. Sensitivity of the global submarine hydrate inventory to scenarios of future climate change, *Earth and Planetary Science Letters* 367, 105-115, doi:10.1016/j.epsl.2013.02.017.

Hustoft, S., Bünz, S., Mienert, J., 2010. Three-dimensional seismic analysis of the morphology and spatial distribution of chimneys beneath the Nyegga pockmark field, offshore mid-Norway. *Basin Research* 22(4), 465-480.

Hustoft, S., Bünz, S., Mienert, J., Chand, S., 2009. Gas hydrate reservoir and active methane-venting province in sediments on < 20 Ma young oceanic crust in the Fram Strait, offshore NW-Svalbard. *Earth and Planetary Science Letters* 284(1), 12-24.

Hustoft, S., Mienert, J., Bunz, S., Nouze, H., 2007. High-resolution 3D-seismic data indicate focussed fluid migration pathways above polygonal fault systems of the mid-Norwegian margin. *Marine Geology* 245(1), 89-106.

Ivanov, M., Blinova, V., Kozlova, E., Westbrook, G., Mazzini, A., Minshull, T., Nouzé, H., 2007. First sampling of gas hydrate from the Vøring Plateau. *Eos, Transactions American Geophysical Union* 88(19), 209-216.

Jaeger, J.C., Cook, N.G., Zimmerman, R., 2009. Fundamentals of rock mechanics. John Wiley & Sons, 90-94.

Johnson, A.H., 2011. Global resource potential of gas hydrate – a new calculation. *Natural Gas & Oil* 304, 285-4541.

Judd, A.G., 2003. The global importance and context of methane escape from the seabed. *Geo-Marine Letters* 23(3-4), 147-154.

Kennett, J.P., Cannariato, K.G., Hendy, I.L., Behl, R.J., 2000. Carbon isotopic evidence for methane hydrate instability during Quaternary interstadials. *Science* 288(5463), 128-133.

Kennett, J.P., Cannariato, K.G., Hendy, I.L., Behl, R.J., 2003. Methane hydrates in quaternary climate change: the clathrate gun hypothesi. Spec. Publ. American Geophysical Union, Washington, DC, 1-9.

Kerr, R.A., 2004. Gas hydrate resource: smaller but sooner. *Science* 303(5660), 946-947.

Krastel, S., Wynn, R.B., Hanebuth, T.J.J., Henrich, R., Holz, C., Meggers, H., Kuhlmann, H., Georgiopoulou, A., Schulz, H.D., 2006. Mapping of seabed morphology and shallow Sediment structure of the Mauritania continental margin, Northwest Africa: some implications for geohazard potential. *Norwegian Journal of Geology* 86, 163-176.

Krustel, S., Wynn, R.B., Honebuth, T., Henrich, R., Holz, C., Meggers, H., Kuhlmann, H., Georgiopoulou, A., Schulz, H.D., 2006. Mapping of seabed morphology and shallow sediment structure of the Mauritania continental margin, Northwest Africa: some implications for geohazard potential. *Norsk Geologisk Tidsskrift* 86(3), 163.

Kvalstad, T.J., Andresen, L., Forsberg, C.F., Berg, K., Bryn, P., Wangen, M., 2005. The Storegga slide: evaluation of triggering sources and slide mechanics. *Marine and Petroleum Geology* 22(1), 245-256.

Kvenvolden, K.A., 1988. Methane hydrate – a major reservoir of carbon in the shallow geosphere. *Chemical Geology* 71(1-3), 41-51.

Kvenvolden, K.A., 1993. Gas hydrates – geological perspective and global change. *Reviews of Geophysics* 31, 173-187.

Lane, A., Taylor, A., 2002. Geohazards: Are We Looking at Them the Right Way? View From Down Under, *Offshore Technology Conference*, doi: http://dx.doi.org/10.4043/14106-MS.

Lee, M.W., Hutchinson, D.R., Dillon, W.P., Miller, J.J., Agena, W.F., Swift, B.A., 1993. Method of Estimating the Amount of in-Situ Gas Hydrates in Deep Marine-Sediments. *Marine and Petroleum Geology* 10(5), 493-506.

Lewis, K., 1971. Slumping on a continental slope inclined at 1–4. *Sedimentology* 16(1-2), 97-110.

Li, A., Davies, R.J., Yang, J., 2016. Gas trapped below hydrate as a primer for submarine slope failures. *Marine Geology* 380, 264-271.

Liu, X., Flemings, P.B., 2006. Passing gas through the hydrate stability zone at southern Hydrate Ridge, offshore Oregon. *Earth and Planetary Science Letters* 241(1), 211-226.

Liu, X., Flemings, P.B., 2007. Dynamic multiphase flow model of hydrate formation in marine sediments. *Journal of Geophysical Research: Solid Earth* 112, B03101, doi:10.1029/2005JB004227.

Løseth, H., Wensaas, L., Arntsen, B., Hanken, N., Basire, C., Graue, K., 2011. 1000 m long gas blow-out pipes, *Marine and Petroleum Geology* 28(5), 1047-1060.

Loulergue, L., Schilt, A., Spahni, R., Masson-Delmotte, V., Blunier, T., Lemieux, B., Barnola, J.-M., Raynaud, D., Stocker, T.F., Chappellaz, J., 2008. Orbital and millennial-scale features of atmospheric CH_4 over the past 800,000 years. *Nature* 453(7193), 383-386.

Lu, S.M., McMechan, G.A., 2002. Estimation of gas hydrate and free gas saturation, concentration, and distribution from seismic data. *Geophysics* 67(2), 582-593, doi: 10.1190/1.1468619.

Lu, Z., Sultan, N., 2008. Empirical expressions for gas hydrate stability law, its volume fraction and mass-density at temperatures 273.15 K to 290.15 K. *Geochemical Journal* 42(2), 163-175.

Lyle, S., Huppert, H.E., Hallworth, M., Bickle, M., Chadwick, A., 2005. Axisymmetric gravity currents in a porous medium. *Journal of Fluid Mechanics* 543, 293-302.

Mackay, J.R., 1987. Some mechanical aspects of pingo growth and failure, western Arctic coast, Canada. *Canadian Journal of Earth Sciences* 24(6), 1108-1119.

MacKay, M.E., Jarrard, R.D., Westbrook, G.K., Hyndman, R.D., 1994. Origin of bottom-simulating reflectors: geophysical evidence from the Cascadia accretionary prism. *Geology* 22(5), 459-462.

Mak, T.C., McMullan, R.K., 1965. Polyhedral clathrate hydrates. X. Structure of the double hydrate of tetrahydrofuran and hydrogen sulfide. *The Journal of Chemical Physics* 42(8), 2732-2737.

Marcon, Y., Ondréas, H., Sahling, H., Bohrmann, G., Olu, K., 2014. Fluid flow regimes and growth of a giant pockmark. *Geology* 42(1), 63-66.

Martinez, J.F., Cartwright, J., Hall, B., 2005. 3D seismic interpretation of slump complexes: examples from the continental margin of Israel. *Basin Research* 17(1), 83-108.

Maslin, M., Owen, M., Day, S., Long, D., 2004. Linking continental-slope failures and climate change: Testing the clathrate gun hypothesis. *Geology* 32(1), 53-56.

Mavko, G., Mukerji, T., Dvorkin, J., 2009. The rock physics handbook: Tools for seismic analysis of porous media. Cambridge university press, 350-355.

Max, M.D., Johnson, A.H., Dillon, W.P., 2005. Economic geology of natural gas hydrate. Springer Science & Business Media, 239.

McDonnell, A., Loucks, R.G., Dooley, T., 2007. Quantifying the origin and geometry of circular sag structures in northern Fort Worth Basin, Texas: Paleocave collapse, pull-apart fault systems, or hydrothermal alteration?. *AAPG bulletin* 91(9), 1295-1318.

McGinnis, D.F., Greinert, J., Artemov, Y., Beaubien, S.E., Wuest, A., 2006. Fate of rising methane bubbles in stratified waters: How much methane reaches the atmosphere? *Journal of Geophysical Research: Oceans* 111, C09007, doi:10.1029/2005JC003183.

McIver, R.D., 1982. Role of naturally-occurring gas hydrates in sediment transport. *AAPG Bulletin* 66(6), 789-792.

McMullan, R.K., Jeffrey, G., 1965. Polyhedral clathrate hydrates. IX. Structure of ethylene oxide hydrate. *The Journal of Chemical Physics* 42(8), 2725-2732.

Mello, U.T., Pratson, L.E., 1999. Regional slope stability and slope-failure mechanics from the two-dimensional state of stress in an infinite slope. *Marine Geology* 154(1), 339-356.

Mienert, J., Vanneste, M., Bünz, S., Andreassen, K., Haflidason, H., Sejrup, H.P., 2005. Ocean warming and gas hydrate stability on the mid-Norwegian margin at the Storegga Slide. *Marine and Petroleum Geology* 22(1), 233-244.

Milkov, A.V., 2000. Worldwide distribution of submarine mud volcanoes and associated gas hydrates. *Marine Geology* 167(1), 29-42.

Milkov, A.V., 2004. Global estimates of hydrate-bound gas in marine sediments: how much is really out there? *Earth-Science Reviews* 66(3), 183-197.

Milkov, A.V., Dickens, G.R., Claypool, G.E., Lee, Y.-J., Borowski, W.S., Torres, M.E., Xu, W., Tomaru, H., Tréhu, A.M., Schultheiss, P., 2004. Co-existence of gas hydrate, free gas, and brine within the regional gas hydrate stability zone at Hydrate Ridge (Oregon margin): evidence from prolonged degassing of a pressurized core. *Earth and Planetary Science Letters* 222(3), 829-843.

Minshull, T., Marin-Moreno, H., Armstrong McKay, D., Wilson, P., 2016. Mechanistic insights into a hydrate contribution to the Paleocene-Eocene carbon cycle perturbation from coupled thermohydraulic simulations. *Geophysical Research Letters* 43, 8637-8644, doi:10.1002/2016GL069676.

Moridis, G., 2002. Numerical studies of gas production from methane hydrates, SPE Gas Technology Symposium. Society of Petroleum Engineers, doi: https://doi.org/10.2118/75691-MS.

Moridis, G.J., 2008. Toward production from gas hydrates: current status, assessment of resources, and simulation-based evaluation of technology and potential. Society of Petroleum Engieers, doi: https://doi.org/10.2118/114163-PA.

Moss, J.L., Cartwright, J., 2010a. 3D seismic expression of km-scale fluid escape pipes from offshore Namibia. *Basin Research* 22(4), 481-501.

Moss, J.L., Cartwright, J., 2010b. The spatial and temporal distribution of pipe formation, offshore Namibia. *Marine and Petroleum Geology* 27(6), 1216-1234.

Musgrave, R.J., Bangs, N.L., Larrasoana, J.C., Gracia, E., Hollamby, J.A., Vega, M.E., 2006. Rise of the base of the gas hydrate zone since the last glacial recorded by rock magnetism. *Geology* 34(2), 117-120.

Myhre, C.L., Ferré, B., Platt, S., Silyakova, A., Hermansen, O., Allen, G., Pisso, I., Schmidbauer, N., Stohl, A., Pitt, J., 2016. Extensive release of methane from Arctic seabed west of Svalbard during summer 2014 does not influence the atmosphere. *Geophysical Research Letters* 43, 4624-4631, doi:10.1002/2016GL068999.

Nimblett, J., Ruppel, C., 2003. Permeability evolution during the formation of gas hydrates in marine sediments. *Journal of Geophysical Research: Solid Earth* 108, 2420, doi:10.1029/2001JB001650, B9.

Nicholson, S.E., 2000. The nature of rainfall variability over Africa on time scales of decades to millenia. *Global and Planetary Change* 26(1), 137-158.

Nixon, M.F., Grozic, J.L.H., 2006. A simple model for submarine slope stability analysis with gas hydrates. *Norwegian Journal of Geology* 86(3), 309-316.

Ozisik, M.N., 1993. Heat conduction. John Wiley & Sons, 618.

Padden, M., Weissert, H., de Rafelis, M., 2001. Evidence for Late Jurassic release of methane from gas hydrate. *Geology* 29(3), 223-226.

Paull, C.K., Ussle, W., Borowski, W.S., 1994. Sources of biogenic methane to form marine gas hydrates in situ production or upward migration? *Annals of the New York Academy of Sciences* 715, 392-409.

Paull, C.K., Ussler, W., Borowski, W.S., Spiess, F.N., 1995. Methane-rich plumes on the Carolina continental rise – associations with gas hydrates. Geology 23(1), 89-92.

Paull, C.K., Brewer, P., Ussler, W., Peltzer, E., Rehder, G., Clague, D., 2002. An experiment demonstrating that marine slumping is a mechanism to transfer methane from seafloor gas-hydrate deposits into the upper ocean and atmosphere. *Geo-Marine Letters* 22(4), 198-203.

Pecher, I.A., 2002. Oceanography: Gas hydrates on the brink. *Nature* 420(6916), 622-623.

Pekar, S.F., Christie-Blick, N., Kominz, M.A., Miller, K.G., 2002. Calibration between eustatic estimates from backstripping and oxygen isotopic records for the Oligocene. *Geology* 30(10), 903-906.

Petersen, C.J., Bunz, S., Huston, S., Mienert, J., Klaeschen, D., 2010. High-resolution P-Cable 3D seismic imaging of gas chimney structures in gas hydrated sediments of an Arctic sediment drift. *Marine and Petroleum Geology* 27(9), 1981-1994.

Phrampus, B.J., Hornbach, M.J., 2012. Recent changes to the Gulf Stream causing widespread gas hydrate destabilization. *Nature* 490(7421), 527-530.

Plaza-Faverola, A., Bünz, S., Mienert, J., 2011. Repeated fluid expulsion through sub-seabed chimneys offshore Norway in response to glacial cycles. *Earth and Planetary Science Letters* 305(3), 297-308.

Plaza-Faverola, A., Westbrook, G.K., Ker, S., Exley, R.J., Gailler, A., Minshull, T.A., Broto, K., 2010. Evidence from three-dimensional seismic tomography for a substantial accumulation of gas hydrate in a fluid-escape chimney in the Nyegga pockmark field, offshore Norway. *Journal of Geophysical Research: Solid Earth* 115, B08104, doi:10.1029/2009JB007078.

Popescu, I., De Batist, M., Lericolais, G., Nouzé, H., Poort, J., Panin, N., Versteeg, W., Gillet, H., 2006. Multiple bottom-simulating reflections in the Black Sea: potential proxies of past climate conditions. *Marine Geology* 227(3), 163-176.

Posewang, J., Mienert, J., 1999. The enigma of double BSRs: indicators for changes in the hydrate stability field? *Geo-Marine Letters* 19(1), 157-163.

Rad, U., Hinz, K., Sarnthein, M., Seibold, E., 2012. Geology of the Northwest African continental margin. Springer Science & Business Media, 160-178.

Rajan, A., Mienert, J., Bunz, S., Chand, S., 2012. Potential serpentinization, degassing, and gas hydrate formation at a young (< 20 Ma) sedimented ocean crust of the Arctic Ocean ridge system. *Journal of Geophysical Research: Solid Earth* 117, B03102, doi:10.1029/2011JB008537.

Ramsay, J., 1980. Shear zone geometry: a review. *Journal of Structural Geology* 2(1-2), 83-99.

Reagan, M.T., Moridis, G.J., Elliott, S.M., Maltrud, M., 2011. Contribution of oceanic gas hydrate dissociation to the formation of Arctic Ocean methane plumes. *Journal of Geophysical Research: Oceans* 116, C09014, doi:10.1029/2011JC007189.

Rempel, A.W., and Buffett, B.A., 1997. Formation and accumulation of gas hydrate in porous media. *Journal of Geophysical Research: Solid Earth* 102(B5), 10151-10164, doi:10.1029/97JB00392.

Ripmeester, J.A., John, S.T., Ratcliffe, C.I., Powell, B.M., 1987. A new clathrate hydrate structure. *Nature* 325(6100), 135-136.

Roberts, H.H., 2001. Fluid and Gas Expulsion on the Northern Gulf of Mexico Continental Slope: Mud-Prone to Mineral-Prone Responses, Natural gas hydrates: occurrence, distribution, and detection. American Geophysical Union, 145-161, doi: 10.1029/GM124p0145.

Roberts, H.H., Hardage, B.A., Shedd, W.W., Hunt Jr, J., 2006. Seafloor reflectivity – an important seismic property for interpreting fluid/gas expulsion geology and the presence of gas hydrate. *The Leading Edge* 25(5), 620-628.

Ruppel, C., 2011. Methane hydrates and contemporary climate change. *Nature Education Knowledge* 3(10), 29.

Ruppel, C.D., Kessler, J.D., 2016. The Interaction of Climate Change and Methane Hydrates. *Reviews of Geophysics* 55, 126-168, doi:10.1002/2016RG000534.

Ruppel, C., Kinoshita, M., 2000. Fluid, methane, and energy flux in an active margin gas hydrate province, offshore Costa Rica. *Earth and Planetary Science Letters* 179(1), 153-165.

Saeki, T., Fujii, T., Inamori, T., Kobayashi, T., Hayashi, M., Nagakubo, S., Takano, O., 2008. Extraction of methane hydrate concentrated zone for resource assessment in the eastern Nankai Trough, Japan, *Offshore Technology Conference*, doi: https://doi.org/10.4043/19311-MS.

Sarkar, S., Berndt, C., Minshull, T.A., Westbrook, G.K., Klaeschen, D., Masson, D.G., Chabert, A., Thatcher, K.E., 2012. Seismic evidence for shallow gas‐escape features associated with a retreating gas hydrate zone offshore west Svalbard. *Journal of Geophysical Research: Solid Earth* 117, B09102, doi:10.1029/2011JB009126.

Schmuck, E., Paull, C., 1993. Evidence for gas accumulation associated with diapirism and gas hydrates at the head of the Cape Fear Slide. *Geo-Marine Letters* 13(3), 145-152.

Schowalter, T.T., 1979. Mechanics of secondary hydrocarbon migration and entrapment. *AAPG Bulletin* 63(5), 723-760.

Seibold, E., Fütterer, D., 1982. Sediment dynamics on the Northwest African continental margin. *(A Wiley-Interscience publication)* 147-163.

Serié, C., Huuse, M., Schødt, N.H., 2012. Gas hydrate pingoes: Deep seafloor evidence of focused fluid flow on continental margins. *Geology* 40(3), 207-210.

Sheriff, R.E., Geldart, L.P., 1995. Exploration seismology. Cambridge university press, 73-76, 211-238, 275-346.

Shipley, T.H., Houston, M.H., Buffler, R.T., Shaub, F.J., McMillen, K.J., Ladd, J.W., Worzel, J.L., 1979. Seismic evidence for widespread possible gas hydrate horizons on continental slopes and rises. *AAPG Bulletin* 63(12), 2204-2213.

Shipley, T.H., Moore, G.F., Bangs, N.L., Moore, J.C., Stoffa, P.L., 1994. Seismically inferred dilatancy distribution, northern Barbados Ridge decollement - implications for fluid migration and fault strength. *Geology* 22(5), 411-414.

Siddall, M., Rohling, E.J., Almogi-Labin, A., Hemleben, C., Meischner, D., Schmelzer, I., Smeed, D., 2003. Sea-level fluctuations during the last glacial cycle. *Nature* 423(6942), 853-858.

Singh, S.C., Minshull, T.A., Spence, G.D., 1993. Velocity structure of a gas hydrate reflector. *Science* 260(5105), 204-207.

Skarke, A., Ruppel, C., Kodis, M., Brothers, D., Lobecker, E., 2014. Widespread methane leakage from the sea floor on the northern US Atlantic margin. *Nature Geoscience* 7(9), 657-661.

Sloan, E.D., Koh, C., 2007. Clathrate hydrates of natural gases. CRC press, 53-67, 196-200, 234.

Sloan, E.D., Subramanian, S., Matthews, P.N., Lederhos, J.P., Khokhar, A.A., 1998. Quantifying hydrate formation and kinetic inhibition. *Industrial & Engineering Chemistry Research* 37(8), 3124-3132.

Smith, A.J., Mienert, J., Bünz, S., Greinert, J., 2014. Thermogenic methane injection via bubble transport into the upper Arctic Ocean from the hydrate-charged Vestnesa Ridge, Svalbard. *Geochemistry, Geophysics, Geosystems* 15(5), 1945-1959, doi:10.1002/2013GC005179.

Solheim, A., Berg, K., Forsberg, C.F., Bryn, P., 2005. The Storegga Slide complex: repetitive large scale sliding with similar cause and development. *Marine and Petroleum Geology* 22(1), 97-107.

Soloviev, V., Ginsburg, G., 1994. Formation of submarine gas hydrates. *Bull Geol Soc Denmark* 41, 86-94.

Somoza, L., Leon, R., Ivanov, M., Fernández-Puga, M., Gardner, J., Hernández-Molina, F., Pinheiro, L., Rodero, J., Lobato, A., Maestro, A., 2003. Seabed morphology and hydrocarbon seepage in the Gulf of Cadiz mud volcano area: Acoustic imagery, multibeam and ultra-high resolution seismic data. *Marine Geology* 195(1), 153-176.

Sowers, T., 2006. Late quaternary atmospheric CH_4 isotope record suggests marine clathrates are stable. *Science* 311(5762), 838-840.

Sultan, N., Cochonat, P., Foucher, J.P., Mienert, J., 2004. Effect of gas hydrates melting on seafloor slope instability. *Marine Geology* 213(1), 379-401.

Sun, Q., Cartwright, J., Wu, S., Chen, D., 2013. 3D seismic interpretation of dissolution pipes in the South China Sea: Genesis by subsurface, fluid induced collapse. *Marine Geology* 337, 171-181.

Talling, P., Clare, M., Urlaub, M., Pope, E., Hunt, J., Watt, S., 2014. Large submarine landslides on continental slopes: geohazards, methane release, and climate change. *Oceanography* 27(2), 32-45.

Tréhu, A.M., Flemings, P.B., Bangs, N.L., Chevallier, J., Gracia, E., Johnson, J.E., Liu, C.S., Liu, X.L., Riedel, M., Torres, M.E., 2004. Feeding methane vents and gas hydrate deposits at south Hydrate Ridge. *Geophysical Research Letters* 31, L23310, doi:10.1029/2004GL021286.

Tréhu, A.M., Long, P.E., Torres, M.E., Bohrmann, G., Rack, F.R., Collett, T.S., Goldberg, D.S., Milkov, A.V., Riedel, M., Schultheiss, P., Bangs, N.L., Barr, S.R., Borowski, W.S., Claypool, G.E., Delwiche, M.E., Dickens, G.R., Gracia, E., Guerin, G., Holland, M., Johnson, J.E., Lee, Y.J., Liu, C.S., Su, X., Teichert, B., Tomaru, H., Vanneste, M., Watanabe, M., Weinberger, J.L., 2004. Three-dimensional distribution of gas hydrate beneath southern Hydrate Ridge: constraints from ODP Leg 204. *Earth and Planetary Science Letters* 222(3), 845-862.

Tréhu, A.M., Stakes, D.S., Bartlett, C.D., Chevallier, J., Duncan, R.A., Goffredi, S.K., Potter, S.M., Salamy, K.A., 2003. Seismic and seafloor evidence for free gas, gas hydrates, and fluid seeps on the transform margin offshore Cape Mendocino. *Journal of Geophysical Research: Solid Earth* 108, 2263, doi:10.1029/2001JB001679, B5.

Tréhu, A.M., Torres, M.E., Moore, G.F., Suess, E., Bohrmann, G., 1999. Temporal and spatial evolution of a gas hydrate–bearing accretionary ridge on the Oregon continental margin. *Geology 27*(10), 939-942.

Treude, T., Ziebis, W., 2010. Methane oxidation in permeable sediments at hydrocarbon seeps in the Santa Barbara Channel, California. *Biogeosciences* 7, 3095-3108.

Ussler, W., Paull, C.K., 2008. Rates of anaerobic oxidation of methane and authigenic carbonate mineralization in methane-rich deep-sea sediments inferred from models and geochemical profiles. *Earth and Planetary Science Letters* 266(3), 271-287.

Vadakkepuliyambatta, S., Chand, S., Bünz, S., 2017. The history and future trends of ocean warming ‐ induced gas hydrate dissociation in the SW Barents Sea. *Geophysical Research Letters* 44(2), 835-844, doi:10.1002/2016GL071841.

Vanneste, M., De Batist, M., Golmshtok, A., Kremlev, A., Versteeg, W., 2001. Multi-frequency seismic study of gas hydrate-bearing sediments in Lake Baikal, Siberia. *Marine Geology* 172(1), 1-21,

Vear, A., 2005. Deep-water plays of the Mauritanian continental margin, *Geological Society, London, Petroleum Geology Conference series*. Geological Society of London, 6(1), 1217-1232.

Vella, D., Huppert, H.E., 2006. Gravity currents in a porous medium at an inclined plane. *Journal of Fluid Mechanics* 555, 353-362.

Waelbroeck, C., Labeyrie, L., Michel, E., Duplessy, J.C., McManus, J., Lambeck, K., Balbon, E., Labracherie, M., 2002. Sea-level and deep water temperature changes derived from benthic foraminifera isotopic records. *Quaternary Science Reviews* 21(1), 295-305.

Ward, B., Kilpatrick, K., Novelli, P., Scranton, M., 1987. Methane oxidation and methane fluxes in the ocean surface layer and deep anoxic waters. *Nature* 327(6119), 226-229.

Wefer, G., Fischer, G., 1993. Seasonal patterns of vertical particle flux in equatorial and coastal upwelling areas of the eastern Atlantic. *Deep Sea Research Part I: Oceanographic Research Papers* 40(8), 1613-1645.

Weitemeyer, K.A., Constable, S.C., Key, K.W., Behrens, J.P., 2006. First results from a marine controlled-source electromagnetic survey to detect gas hydrates offshore Oregon. *Geophysical Research Letters* 33, L03304, doi:10.1029/2005GL024896.

Weitemeyer, K.A., Constable, S., Tréhu, A.M., 2011. A marine electromagnetic survey to detect gas hydrate at Hydrate Ridge, Oregon. *Geophysical Journal International 187*(1), 45-62.

Westbrook, G.K., Chand, S., Rossi, G., Long, C., Bunz, S., Camerlenghi, A., Carcione, J.M., Dean, S., Foucher, J.P., Flueh, E., Gei, D., Haacke, R.R., Madrussani, G., Mienert, J., Minshull, T.A., Nouze, H., Peacock, S., Reston, T.J., Vanneste, M., Zillmer, M., 2008. Estimation of gas hydrate concentration from multi-component seismic data at sites on the continental margins of NW Svalbard and the Storegga region of Norway. *Marine and Petroleum Geology* 25(8), 744-758.

Westbrook, G.K., Thatcher, K.E., Rohling, E.J., Piotrowski, A.M., Pälike, H., Osborne, A.H., Nisbet, E.G., Minshull, T.A., Lanoisellé, M., James, R.H., and Hühnerbach, V., 2009, Escape of methane gas from the seabed along the West Spitsbergen continental margin. *Geophysical Research Letters* 36, L15608, doi:10.1029/2009GL039191.

Wood, W.T., Gettrust, J.F., Chapman, N.R., Spence, G.D., Hyndman, R.D., 2002. Decreased stability of methane hydrates in marine sediments owing to phase-boundary roughness. *Nature* 420(6916), 656-660.

Xu, W., Germanovich, L.N., 2006. Excess pore pressure resulting from methane hydrate dissociation in marine sediments: A theoretical approach. *Journal of Geophysical Research: Solid Earth* 111, B01104, doi:10.1029/2004JB003600.

Xu, W., Ruppel, C., 1999. Predicting the occurrence, distribution, and evolution of methane gas hydrate in porous marine sediments. *Journal of Geophysical Research: Solid Earth* 104(B3), 5081-5095, doi:10.1029/1998JB900092.

Yamamoto, K., Terao, Y., Fujii, T., Ikawa, T., Seki, M., Matsuzawa, M., Kanno, T., 2014, May. Operational overview of the first offshore production test of methane hydrates in the Eastern Nankai Trough. *Offshore Technology Conference*, doi: https://doi.org/10.4043/25243-MS.

Yamamoto, A., Yamanaka, Y., Oka, A., Abe-Ouchi, A., 2014. Ocean oxygen depletion due to decomposition of submarine methane hydrate. *Geophysical Research Letters* 41, 5075-5083, doi:10.1002/2014GL060483.

Yang, J., Davies, R.J., 2013. Gravity-driven faults: migration pathways for recycling gas after the dissociation of marine gas hydrates. *Marine Geology* 336, 1-9.

Yang, J., Davies, R.J., Huuse, M., 2013. Gas migration below gas hydrates controlled by mass transport complexes, offshore Mauritania. *Marine and Petroleum Geology* 48, 366-378.

Yun, T.S., Lee, C., Lee, J.S., Bahk, J.J., Santamarina, J.C., 2011. A pressure core based characterization of hydrate‐bearing sediments in the Ulleung Basin, Sea of Japan (East

Sea). *Journal of Geophysical Research: Solid Earth* 116, B02204, doi:10.1029/2010JB007468.

Zhang, Z.J., McConnell, D.R., Han, D.H., 2012. Rock physics-based seismic trace analysis of unconsolidated sediments containing gas hydrate and free gas in Green Canyon 955, Northern Gulf of Mexico. *Marine and Petroleum Geology* 34(1), 119-133.

Zühlsdorff, C., Wien, K., Stuut, J.-B., Henrich, R., 2007. Late Quaternary sedimentation within a submarine channel-levee system offshore Cap Timiris, Mauritania. *Marine Geology* 240(1), 217-23.

Appendix 1: Water temperature

The ocean data are from World Ocean Database (WOD) over the area of 17-21 °W, 18-21 °N (Fig.A1.1). The data include 70 *T-D* profiles recorded since 2009 by high-resolution Conductivity-Temperature-Depth (CTD), Ocean Station Data (OSD), Profiling Float Data (PFL) and Expendable bathythermograph data (XBT). These data can be found in http://nodc.noaa.gov/OCS/WOD/ and viewed in the software of Ocean Data View 4. The temperature data acquired at more than 50 m depth interval are not selected due to their low resolution. The ocean temperatures of C-6 and C-19 at each water depth are means of data recorded in March 2000 and December 2012 (Fig.A1.2). Some temperature data are linearly interpolated based on *T-D* profile.

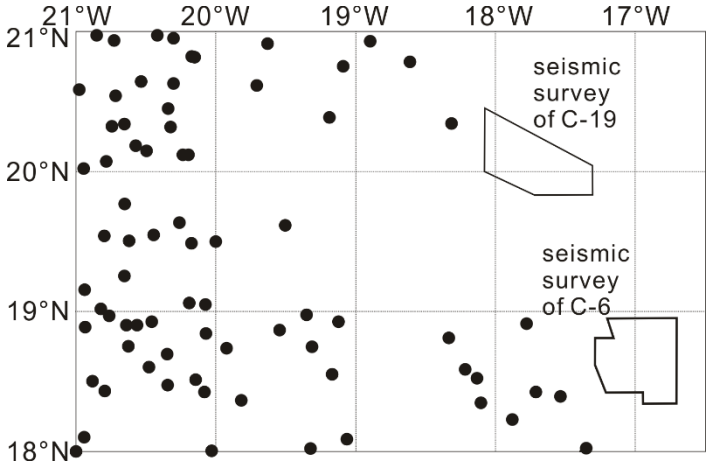

Fig.A1.1 Location of sampling of ocean temperature data and the seismic surveys.

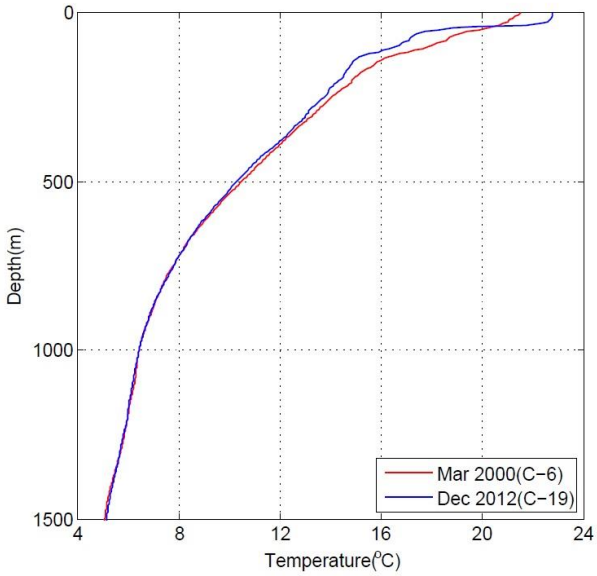

Fig.A1.2 Temperature-Depth(*T-D*) profiles of seismic surveys of C-6 and C-19

Appendix 2: Two-dimensional heat diffusion model for the BHSZ shift

We developed a 2-D finite diffusive heat-flow model to show an event of the BHSZ shoaling since the LGM. The governing equation for 2-D heat diffusion model is found from:

$$\rho_b C_b \frac{\partial T}{\partial t} = k_x \frac{\partial^2 T}{\partial x^2} + k_z \frac{\partial^2 T}{\partial z^2} \quad \text{(A2.1)}$$

where T is the sediment temperature, x and z are the sediment length and depth below the seafloor respectively, ρ_b is the sediment density, C_b is the specific heat capacity, and t is time. k_x and k_z are the sediment thermal conductivities in the horizontal and vertical direction, respectively. The subsurface sediment is assumed to be isotropic and homogeneous such that k_x=k_z. We assume the constant thermal conductivity of 1 W m^{-1} K^{-1}, an average bulk density of 2000 kg m^{-3}, which are consistent with the results recorded in the Global Heat Flow Database and the drilling data of Ras El Baida A-1, and a specific heat capacity of 2200 J K^{-1} kg^{-1} (Rempel and Buffett, 1997). All the gases trapped in hydrates are assumed to be methane and their molecular structure to be type I ($CH_4 \cdot 5.75H_2O$). If the temperature for hydrate equilibrium, T_c, is known, the pressure, P_c, can be determined from the empirical equation (Lu and Sultan, 2008):

$$P_c = \exp\big((C_s S + D_s)T_c\big) \exp(E_s S) F_s \quad \text{(A2.2)}$$

where S is the salinity of pore fluid (3.5 wt%), equal to that of seawater. C_s, D_s, E_s and F_s are constants of 0.1711726397, 0.1046133676, -34.14836102 and 1.010769956×10^{-9}, respectively. This simulation is applicable at the temperature of 273.15-300 K and the pressure of 1.5-40 MPa (150-4000 m water depth). We calculated the hydrostatic pressure gradient of 10.05 MPa/km by assuming the seawater density of 1024 kg m^{-3}.

Firstly we estimate the location of the present BHSZ and the geothermal gradient by using the numerical model that is discretised into 50 m (horizontal) × 10 m (vertical) cells and subjected to the boundary conditions:

$$T = T_o, \quad 0 \le x \le 32 \text{ km}, \quad 600 \text{ m} \le z \le 2200 \text{ m}, \quad t = 0$$

$$\partial T/\partial z = J, \quad 0 \le x \le 32 \text{ km}, \quad z = 2200 \text{ m}, \quad t > 0$$

$$\partial T/\partial z = 0, \quad 0 \le x \le 32 \text{ km}, \quad z = 600 \text{ m}, \quad t > 0$$
$$\partial T/\partial x = 0, \quad x = 32 \text{ km}, \quad 600 \text{ m} \le z \le 2200 \text{ m}, \quad t > 0$$
$$\partial T/\partial x = 0, \quad x = 0, \quad 600 \text{ m} \le z \le 2200 \text{ m}, \quad t > 0$$

where J is the geothermal gradient, T_o is the calculated ocean temperature in December 2009 (acquisition time of seismic data). The Neumann boundary conditions in this model prescribe heat flux at four boundaries. Specifically, the top, left and right boundaries are assumed to be perfectly insulated, while $\partial T/\partial x$ is assumed to be constant (equal to the geothermal gradient) at the bottom boundary. The temperature of ocean water at each depth (results are shown in Fig. A1.2) is the average of the values over the region 18-22^o N, 17-21^o W in December 2009, taken from the World Ocean Database (WOD). The geothermal gradient in the study area is unknown and two values of 29 ^{o}C km^{-1} (Davies et al., 2012b) and 46 ^{o}C km^{-1} (measured at 20.07^o N, 19.97^o W, data from Global Heat Flow Database) recorded near the site are taken as the end-members to estimate the range of the BHSZ location. Some arbitrary values of the geothermal gradient are also used to determine its value based on the seismic observation. Fig. A2.1 shows that at time zero the observed BSR is within its predicted zone and the geothermal gradient of 35 ^{o}C km^{-1} has the modelling result that fits most with the observed BSR. The discrepancy between the observed and modelled BSR at the depths smaller than 1400 mbsl could be attributed to the subsurface temperature regime that does not reach the steady state (c.f. Phrampus and Hornbach, 2012).

Next we use the numerical model to show the variation of the BHSZ since the LGM and to accelerate computing we narrow the modelled region. The model is changed to have a 400 × 200 cell temperature grid (with 20 m × 3.5 m cell dimensions). This grid spacing is chosen because: 1) the numerical scheme is computationally stable. Larger cells may cause the instability of the modelled BHSZ near the seabed (It is jagged rather than a smooth concave-up curve); 2) computing the scheme is feasible using personal computer. More cells would take more time to compute without significantly increasing the accuracy. The computing time of this model is ~10 hours. The initial and boundary condition can be written as:

$$
\begin{aligned}
T &= T_o', && 0 \le x \le 8 \text{ km}, && 600 \text{ m} \le z \le 1300 \text{ m}, && t = 0 \\
\partial T/\partial z &= J, && 0 \le x \le 8 \text{ km}, && z = 1300 \text{ m}, && t > 0 \\
\partial T/\partial z &= 0, && 0 \le x \le 8 \text{ km}, && z = 600 \text{ m}, && t > 0 \\
\partial T/\partial x &= 0, && x = 8 \text{ km}, && 600 \text{ m} \le z \le 1300 \text{ m} && t > 0 \\
\partial T/\partial x &= 0, && x = 0, && 600 \text{ m} \le z \le 1300 \text{ m} && t > 0
\end{aligned}
$$

where T_o' is the initial temperature at 20 kyr ago. The bathymetry is from Fig. 4.2a and assumed to be unchanged since 20 kyr ago. The data of RSL in the past 20 kyr are acquired by linearly interpolation from fig.1 by Siddall et al. (2003) (Fig. A2.2a). We use the temperature anomalies in Bintanja and van de Wal (2008) to estimate the variation of the temperature of deep ocean with time (Fig. A2.2b). The effect on the deep-ocean temperature, which is from ice-sheet and precipitating snow, is calculated through linear relation between the deep-water and the 3-kyr mean surface air temperature anomalies based on a climate-ocean model (Bintanja and van deWal, 2008). Heat transfer and time during hydrate formation and dissociation are not considered. At each time step the reference frame of the vertical shift of the BHSZ is the seabed. Eq. A2.1 is discretised in space using finite differences and then solved using the MATLAB ordinary differential equation (ODE) solver, ODE45. The ODE45 solver is designed to solve the ordinary differential equation and has an adaptive time stepping routine. The solver repeats its calculations with successively smaller time-steps until the error between two results, generated using Runge-Kutta 4th and Runge-Kutta 5th methods, is below a pre-defined error tolerance. The solver is able to compute solutions much faster than conventional first-order explicit time-stepping schemes without compromising accuracy.

Fig. A2.2c shows the BHSZ shoaled since the LGM at the site where the water depth is 825 m (its location is marked by the red triangle in Fig. 4.5). However, there are uncertainties in the modelling and some of them stem from the input values of parameters. Results based on different data show different degrees of oceanic warming, such as the data from the Paleoclimate Modelling Intercomparision Project Phase 3 (PMIP3, the data can be downloaded from https://pcmdi.llnl.gov/projects/esgf-llnl/) indicating that the temperature at the water depth of 600 – 900 m have increased by 0.8 – 3.9 ^{o}C since 20 kyr ago. The data of BWT and RSL are

not directly measured offshore of Mauritainia and may not suffice to reveal what happened in the sutdy area.

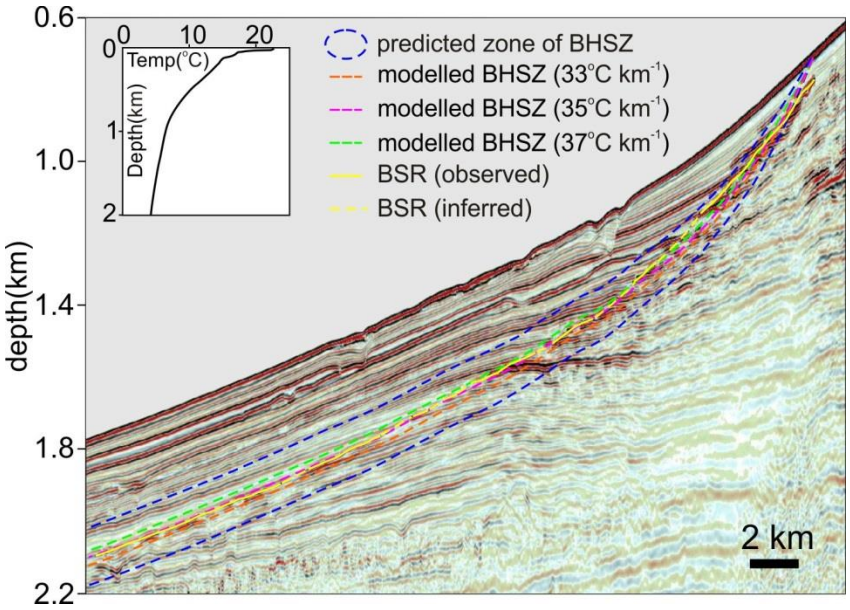

Fig.A2.1 The modelled locations of the BHSZ with inputs of different geothermal gradient on a seismic cross section. Their correlation with the observed BSR determines the geothermal gradient. The inset is the temperature-depth plot of the ocean water.

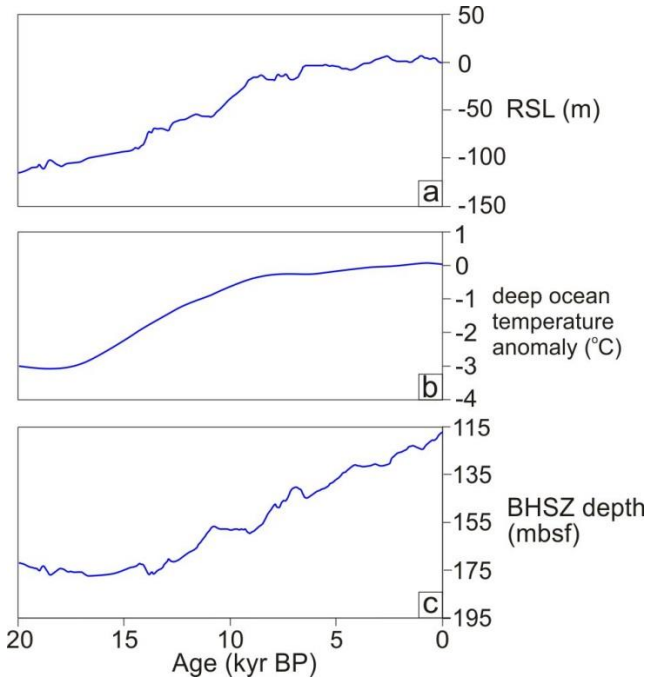

Fig.A2.2 The variation of relative sea level (RSL) (a) and bottom water temperature (BWT) (b) in the last 20 kyr. The modelled variation of the BHSZ depth is shown in Fig. c. The site is marked by the red triangle in Fig. 4.5. A gas chimney is observed here. mbsf – metres below seafloor.

Appendix 3: One-dimensional synthetic seismogram

The rock models and the parameters used are shown in Fig. A3.1 and Table A3.1. The ray path is assumed to be vertical and all interfaces are horizontal. Diffraction is ignored. The down-going seismic wavelet is assumed to be the Ricker wavelet. All pore pressure is hydrostatic. The water depth is assumed to be 800 m and the BSR depth is to be 200 mbsf. The rock physical model assumes gas hydrate acts as part of pore fluid. This study considers only the variation of the waveform so no time-depth conversion is done here. The convolved wavelet here is the Ricker wavelet:

$$A = (1 - 2\pi^2 v_M^2 t^2) e^{-(\pi v_M t)^2} \qquad \text{Eq. A3.1}$$

where A is the amplitude, v_M is the peak frequency and t is the sampling time. The saturations of hydrate deposit are assigned at a step of 10% and the 1-D synthetic seismic diagrams shown in Fig.A3.2-4.

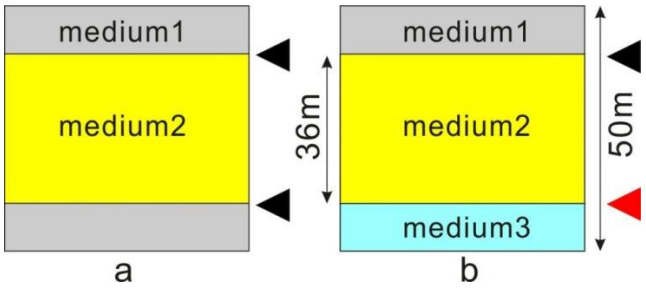

Fig.A3.1 (a) Model of the isolated hydrate reservoir and (b) model of the hydrate deposit underlain by free gas zone. Medium 1 is clay, medium 2 is hydrate-containing sandy sediment and medium 3 is gas-charged sediment. The black arrows mark the interface between clay and hydrate-bearing sandy sediments. The red arrow indicates the location of the BSR.

Table A3.1 Parameters used in the model

Seawater density	ρ_w= 1024 kg m^{-3}	Peak frequency of wavelet	v^M= 50 Hz
Clay density	ρ_c= 2580 kg m^{-3}	Wavelength of wavelet	λ = 36 m
Sand density	ρ_s= 2650 kg m^{-3}	Geothermal gradient	J = 36 ^{o}C km^{-1}
Gravity acceleration	g = 9.81 m s^{-2}	P-wave velocity in seawater	v_w = 1450 m s^{-1}
Methane hydrate density	ρ_{gh}= 910 kg m^{-3}	P-wave velocity in methane hydrate	v_{gh} = 3750 m s^{-1}
P-wave velocity in clay	v_c = 2500 m s^{-1}	Clay porosity	φ = 20 %
P-wave velocity in sand	v_s = 3500 m s^{-1}	Gas saturation	S_g = 5 %

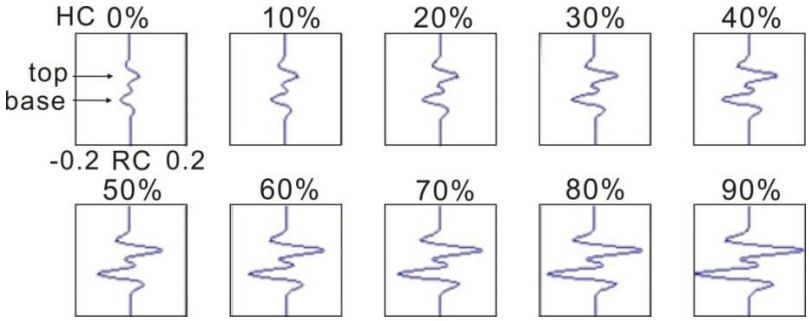

Fig.A3.2 Synthetic seismic diagram of model a. Porosities of hydrate reservoir and clay are 30% and 20%. HC – hydrate concentration, RC – reflection coefficient for this and subsequent figures.

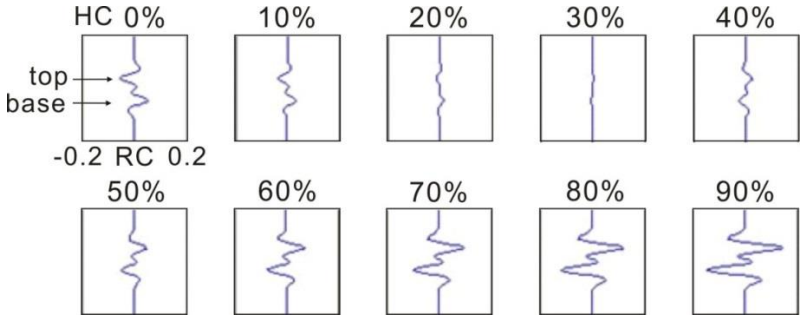

Fig.A3.3 Synthetic seismic diagram of model a. Porosities of hydrate reservoir and clay are 40% and 20%.

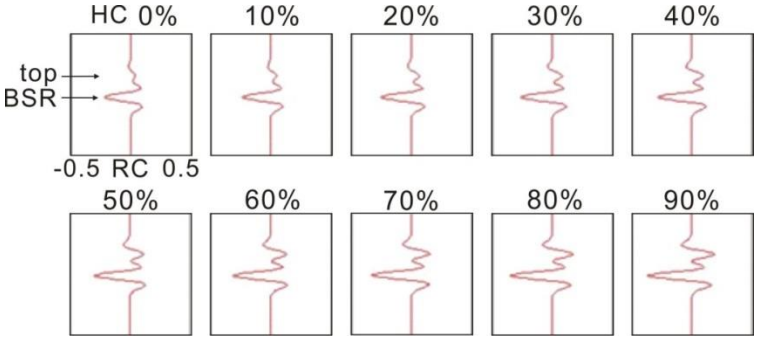

Fig.A3.4 Synthetic seismic diagram for the interface between hydrate-containing and gas-charged sediments (model b).

Appendix 4: Horizon maps

Block C-6

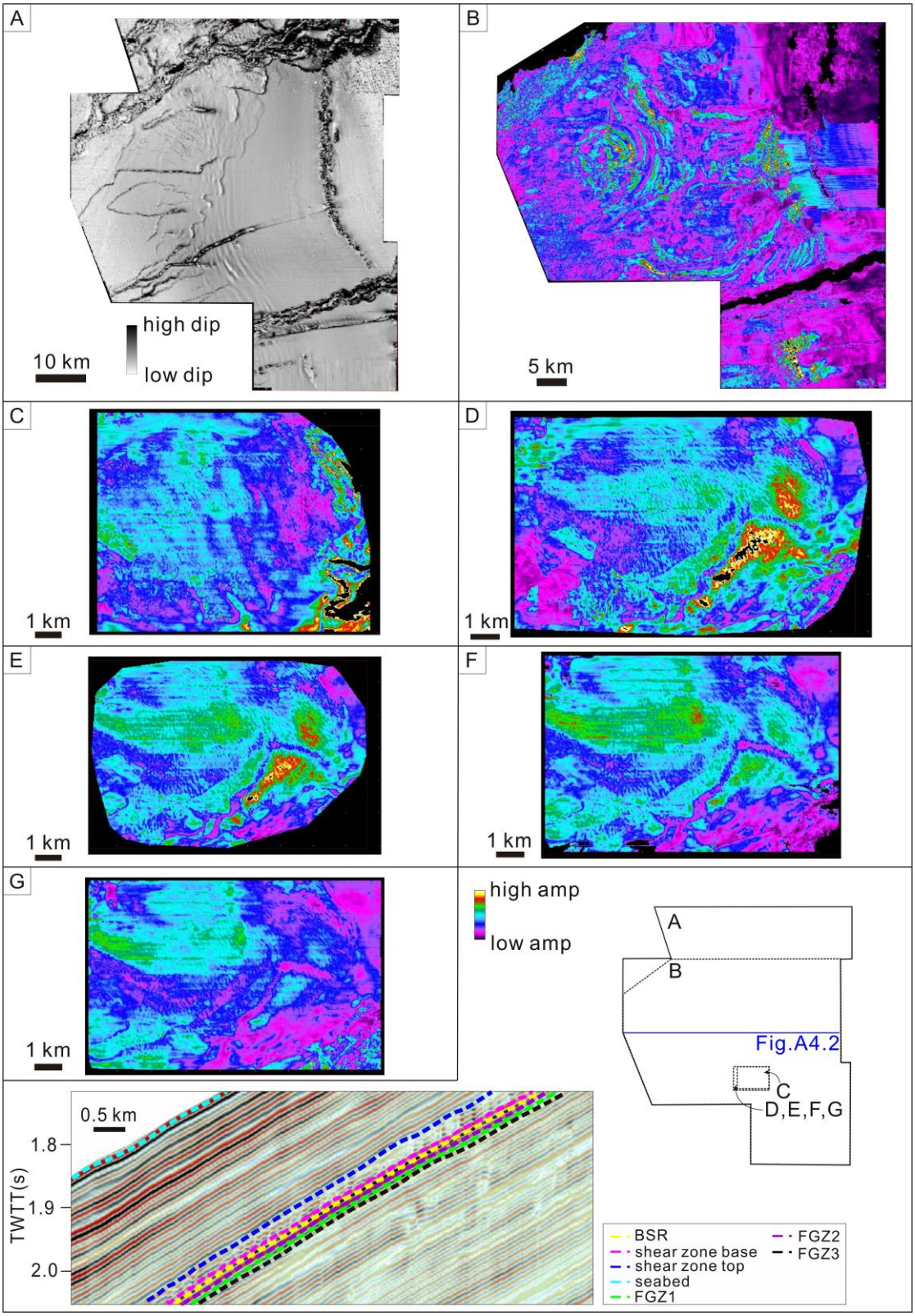

Fig.A4.1.A – dip magnitude map of seabed; B – RMS amplitude map of BSR; C – RMS amplitude map of top of shear zone; D – RMS amplitude map of base of shear zone; E – RMS amplitude map of reflection FGZ1; F – RMS amplitude map of reflection FGZ2; G – RMS amplitude map of reflection FGZ3

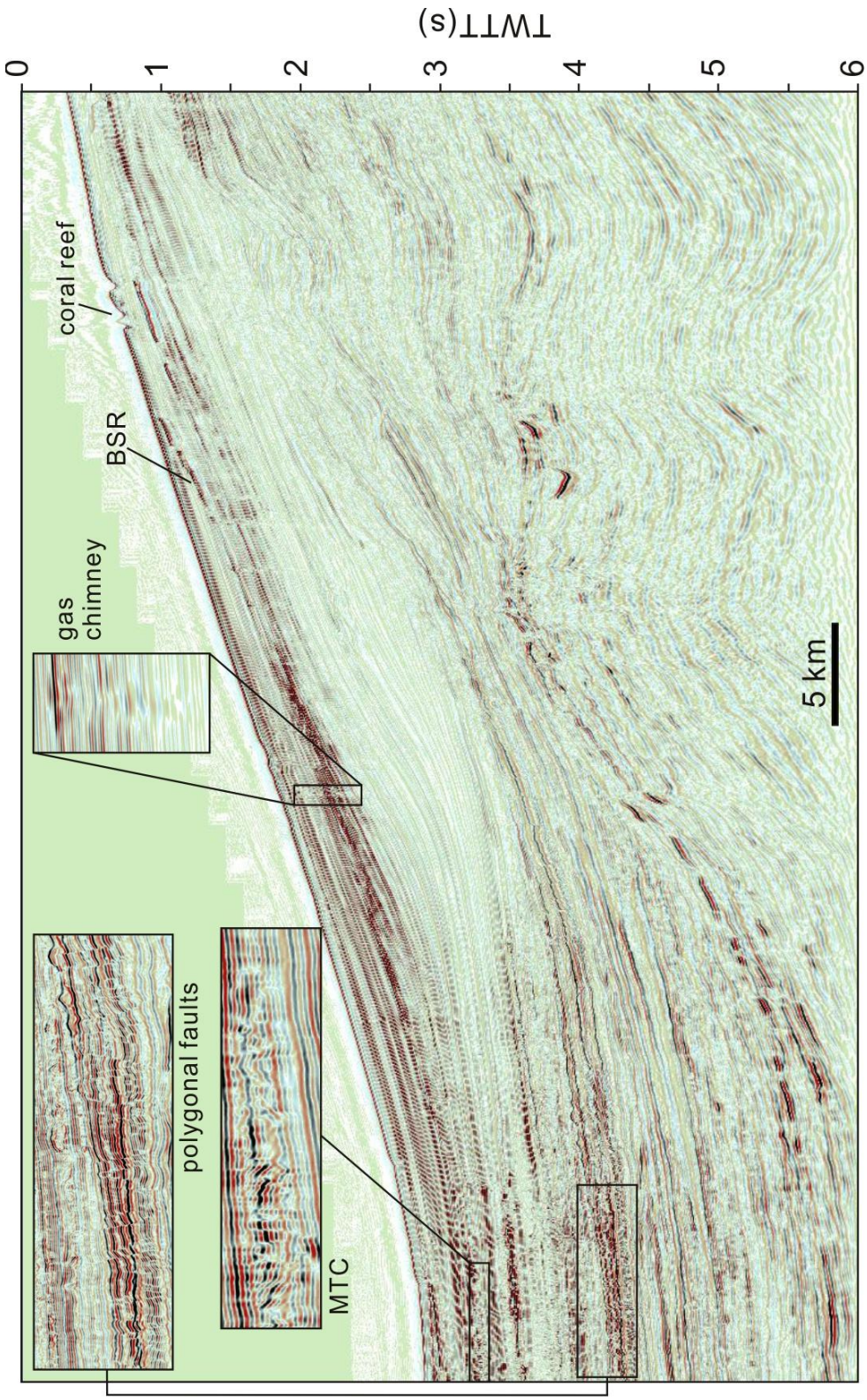

Fig. A4.2 A representative seismic cross section of block C-6. Its location is shown in Fig.A4.1.Please note the vertical exaggeration of the inset of the gas chimney is 1.

Block C-19

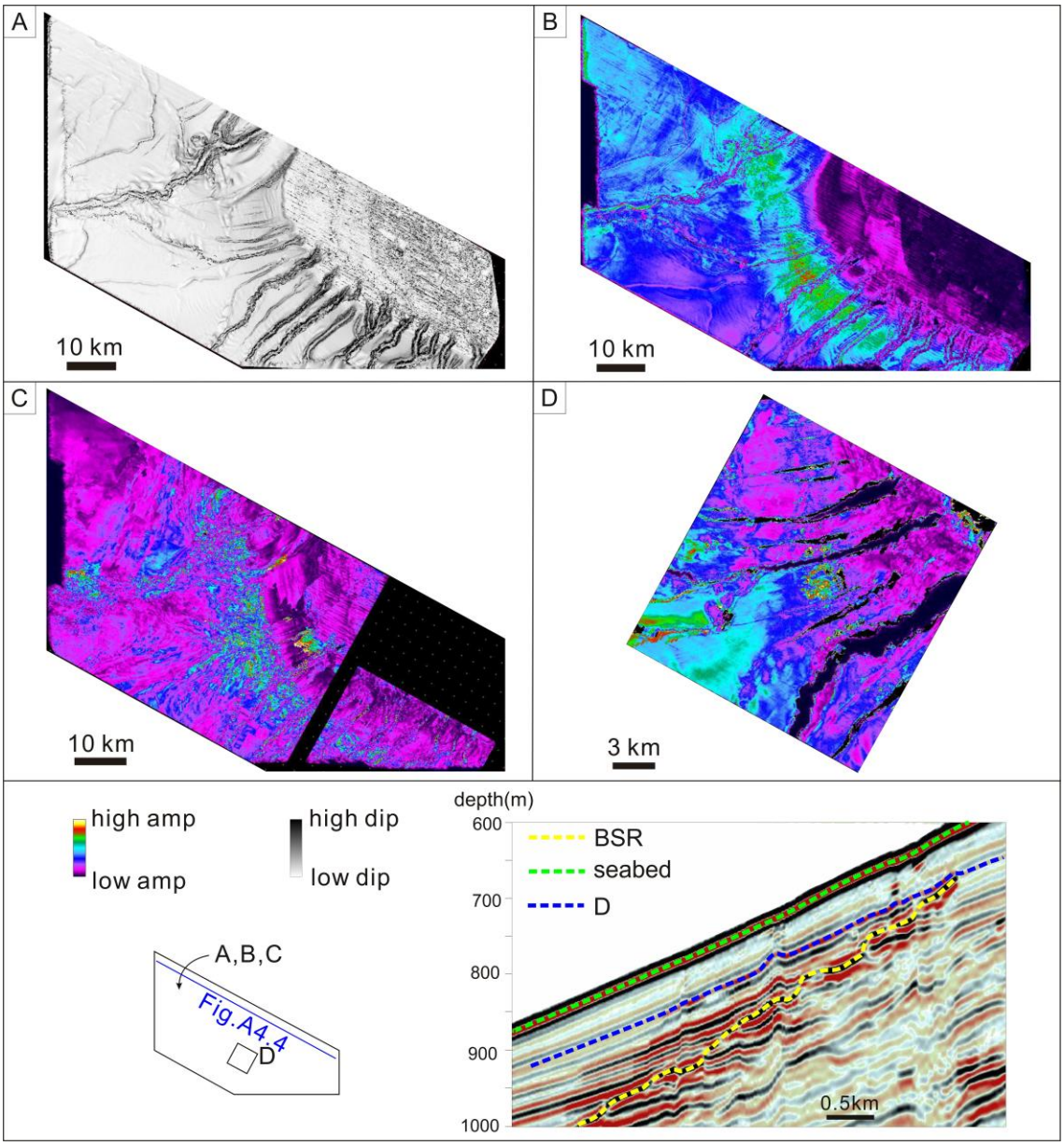

Fig.A4.3 A – dip magnitude map of seabed; B – RMS amplitude map of seabed; C – RMS amplitude map of BSR; D – RMS amplitude map of reflection D. Reflections of A, B, C, E and F are stated in chapter 4.

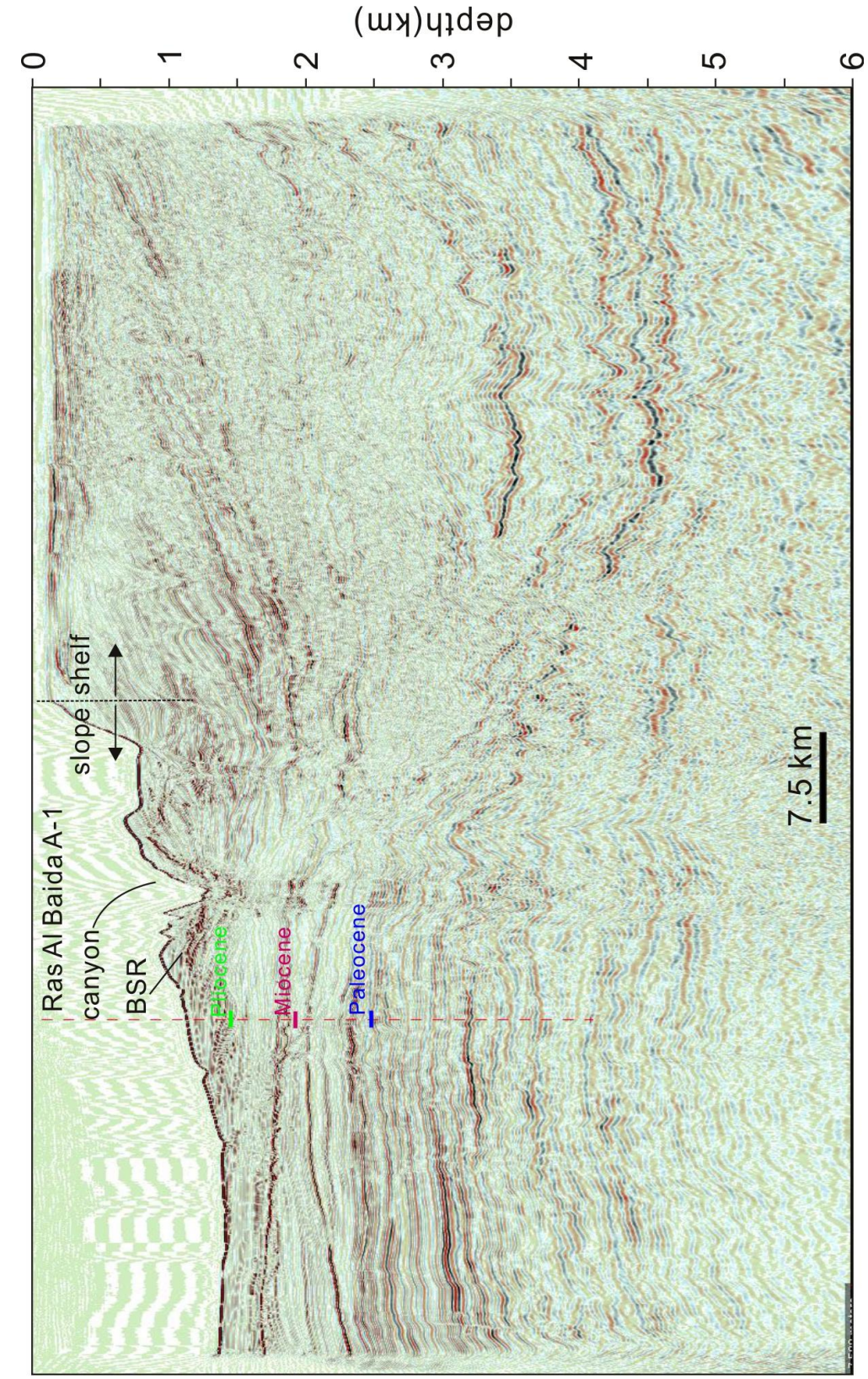

Fig. A4.4 A representative seismic cross section of block C-19. Its location is shown in Fig.A4.3.

Appendix 5: Seismic header for block C-19

C1 CLIENT: CHARIOT OIL & GAS SURVEY: MAURITANIA
C2 DATA TYPE: FULL STACK AFTER WAVLET DOMAIN DENOISE WITH AGC: DEPTH
C3 DATA ORDER: INLINE; INLINE RANGE: 984-2784 XLINE RANGE 488-9600
C4 ACQUISITION: FUGRO GEOTEAM VESSEL: MV GEO CELTIC DATE: DEC 2012
C5 CABLES: 12 CHANNELS:564 GRP INT:12.5 SEPARATION: 100M DEPTH: 8M
C6 SOURCES: 2 SP INTERVAL: 25M SEPARATION: 50M DEPTH: 6M
C7 RECORD LENGTH: 8000ms SR 2ms FILTER: 3(6)-200(370) Hz (dB/Oct)
C8 PROCESSING: CGG - SWANLEY, UK, DATE: APR 2013
C9 INPUT SEGD, TRACE EDITS, NAV/SEISMIC MERGE, 3Hz FILTER,
C10 DESIGNATURE TO ZERO PHASE, T2 GAIN, RESAMP TO 4MS, SWELL REMOVAL, GUN&CABLE
C11 STATICS, 3D SRME, LINEAR NOISE ATTENUATION, TAUP DECON & LINEAR NOISE
C12 ATTENUATION, VELS AT 1KM, DIFFRACTED NOISE ATTENUATION, RADON DEMULTIPLE,
C13 SCAMP, INVERSE PHASE Q, OFFSET INTERPOLATION, FXY DECONVOLUTION
C14 DEPTH DOMAIN PROCESSING:
C15 PSDM VELOCITY MODEL GENERATION: GMM + 3 PASSES TOMOGRAPHY
C16 FINAL VEL MOD M330: ISOTROPIC KIRCHOFF PRE STK DEPTH MIG 12.5m X 25m GRID
C17 4Km APERTURE: STRETCH TO TIME: INNER/OUTER MUTE, STACK(1/N),
C18 AMP BALANCING, AMPLITUDE Q, dB SCALE, TVF, STRETCH TO DEPTH,O/P SEGY
C19 POLARITY: peak=+ve number=increase in acoustic impedance
C20 PGS PROCESSING:
C21 INPUT: FULL - FOLD PSDM STACK - relative amplitude version: DEPTH
C22 STRETCH TO TIME, WAVELET DOMAIN DENOISE, AGC, STRETCH TO DEPTH,O/P SEGY
C23 PROCESSING GRID CONER POINTS:

C24 EASTING	NORTHING	IL	XL
C25 281968.580000	2212931.950000	2976	1
C26 176908.889485	2270918.684939	2976	9601
C27 150633.650216	2223313.512674	801	9601
C28 255693.340731	2165326.777735	801	1

C29 DATUM: WGS-84 PROJECTION: ZONE 28N CENTRAL MERIDIAN: 15W
C30 ROTATED GRID DEFINITION:
C31 GRID ORIGIN X:281968.58 Y:2212931.95 DIRECTION: 298.89610
C32 GRID ORIGIN INLINE: 2976 XLINE:1, INLINE CELL SIZE 12.5m, XLINE CELL SIZE:25m
C33 SAMPLES/TRACE : 3668 SAMPLE INTERVAL : 3000 mm
C34 FIRST SAMPLE AT : 0 m
C35 VERTICAL DIMENSION: TVDSS (m)
C36 SAMPLE RECORDING FORMAT: IBM FLOATING POINT (4-BYTE) SEG Y REV1
C37 HEADER BYTE LOCATIONS AND TYPES:
C38 3D INLINE: 189-192 (4-BYTE INT) 3D CROSSLINE: 193-196 (4-BYTE INT)
C39 ENSEMBLE X: 181-184 (4-BYTE INT) ENSEMBLE Y: 185-188 (4-BYTE INT)
C40 END TEXTUAL HEADER